

Université Mohamed Khider – Biskra
Faculté des Sciences et de la technologie
Département : Chimie Industrielle
Ref :



جامعة محمد خيضر بسكرة
كلية العلوم و التكنولوجيا
قسم: الكيمياء الصناعية
المرجع:

Thèse présentée en vue de l'obtention
Du diplôme de
Doctorat en sciences en : Chimie Industrielle
Spécialité (Option) : Génie Chimique

Synthèse de ligands bi-dentâtes de type base de schiff et leurs complexes métalliques

Synthesis of bidentate Schiff's base ligands and their metallic complexities

Présenté par :
REGHIOUA Abdallah

Soutenue publiquement le

Devant le jury composé de :

Dr. Sakri Adel	Maître de Conférences	Président	Université de Biskra
Dr. Barkat Djamel	Professeur	Rapporteur	Université de Biskra
Dr. Nedjar Zohir	Professeur	Examineur	Université de Khenchela
Dr. Khalef Abdelhamid	Professeur	Examineur	Université d'Eloued
Dr. Jawad H Ali AlTaie	Professeur	Invité	Université MARA (Malaysia)

ACKNOWLEDGEMENTS

First of all, I would like to thank ALLAH (s.w.t) for giving me perseverance, and patience throughout this Ph.D. journey. I will like to appreciate Dr. Barkat Djamel and Dr. Jawad H Ali Al Taie for their support, timely corrections, in moments I needed it in the course of my research work.

I also would like to thank all Dr. Sakri Adel, Dr. Nedjar Zohir, and Dr. Khelef Abdelhamid. for accepting to discuss my thesis.

Last but not least, I would like to thank my family who supported me, Thank you for dropping all and being present whenever I needed your help.

Abstract :

Liquid wastes of industrial are considered especially the dyes, which is directly discharged into rivers and other environmental parts, is one of the most important factors contributing to water pollution around the world. Therefore, many environmental associations call for finding solutions to treat these pollutants, which directly affect human health and the quality of aquatic life. In this research work, the adsorption of Remazol Brilliant Blue R dye in an aqueous solution onto biocomposites from a type of bi-function Schiff bases were studied. These adsorbents were prepared using different loading of ZnO nanoparticles into the polymeric matrix of Chitosan. Four adsorption operation parameters were studied to optimize these adsorbents (adsorbent dose, solution pH, temperature, and contact time). Empirical data were analyzed using Langmuir, Freundlich, and Temkin isotherm models to evaluate the maximum adsorption capacities. The adsorbents also were characterized using scanning electron microscopy- energy-dispersive x-ray (SEM-EDX), Fourier-transform infrared (FTIR) spectroscopy.

The remarkable output of this research can open a window for other possible significant applications such as treatment of real wastewater, removal of heavy metal ions, and reduction of chemical oxygen demand.

Keywords: Schiff's base; Chitosan; ZnO nanoparticles; Response surface methodology; Adsorption.

الملخص:

تعتبر المخلفات الصناعية السائلة ، خاصة الأصباغ منها و التي يتم تصريفها مباشرة في الأنهار والأجزاء البيئية الأخرى ، من أهم العوامل المساهمة في تلوث المياه حول العالم. لذلك ، تسعى العديد من الجمعيات البيئية بإيجاد حلول لمعالجة هذه الملوثات التي تؤثر بشكل مباشر على صحة الإنسان ونوعية الحياة المائية. في هذا البحث ، تمت دراسة امتزاز صبغة ريمazol بريليان بلو آر في محلول مائي على مركبات حيوية من نوع قواعد شيف ثنائية الوظيفة. تم تحضير هذه الممتزازات باستخدام تحميل مختلف من جزيئات أكسيد الزنك النانوية في المصفوفة البوليمرية للشيتوزان. تمت دراسة أربعة متغيرات لتحسين عملية الامتزاز هذه الممتزازات : (جرعة الممتزاز ، درجة الحموضة في المحلول ، درجة الحرارة ، ووقت الاتصال). تم تحليل البيانات التجريبية باستخدام نماذج متساوية الحرارة لانجموير وفريوندليش وتمكين لتقييم قدرات الامتزاز القصوى. كما تم توصيف الممتزازات أيضا باستخدام تقنيات التحليل نذكر منها : التحليل بالمسح المجهر الإلكتروني - الاشعة المشتتة للطاقة وتحليل الطيفي للاشعة تحت الحمراء .

يمكن للنتائج الرائعة لهذا البحث أن تفتح نافذة للتطبيقات الهامة الأخرى الممكنة مثل معالجة مياه الصرف الصحي الحقيقية ، وإزالة أيونات المعادن الثقيلة ، وتقليل الطلب على الأكسجين الكيميائي.

الكلمات المفتاحية: قواعد شيف ، الشيتوزان ، الجسيمات النانوية لأكسيد الزنك ، منهجية استجابة السطح

، الامتزاز

CONTENTS

Acknowledgements	i
Abstract	ii
List of Contents	iv
List of Tables	vii
List of Figures	ix
List of Symbols and Abbreviations	xii
GENERAL INTRODUCTION	1
Introduction	2
Background of Study	2
Problem Statement	3
Significance of Study	4
Research Objectives	4
Novelty of study	5
Thesis Layout	5
1 LITERATURE REVIEW	6
1.1 Introduction	7
1.2 Dyes	7
1.2.1 Classification of dyes	7

1.2.2	Toxicity effects of dyes	9
1.3	Adsorption	10
1.3.1	Factors impacting the Extent of Adsorption	11
1.3.2	Use of Schiff's base for adsorption of synthetic dyes	12
2	METHODOLOGY	15
2.1	Introduction	16
2.2	Materials and Chemical Solvent used	16
2.3	Synthesis of Schiff's base Composites	18
2.3.1	Preparation of Chitosan-Glyoxal/ZnO/ Fe_3O_4 ($CS - G/ZnO/Fe_3O_4$)	18
2.3.2	Preparation of chitosan-glutaraldehyde/ZnO/ Fe_3O_4	20
2.3.3	Preparation of chitosan-Benzil/ZnO/ Fe_3O_4	22
2.4	Instrumentation	24
2.4.1	Scanning Electron Microscopy (SEM)	24
2.4.2	Fourier Transform Infrared Spectroscopy (FTIR)	24
2.4.3	Brunauer-Emmett-Teller (BET)	24
2.4.4	X-Ray Diffraction (XRD)	24
2.4.5	Elemental Analysis (CHN)	25
2.4.6	Zero Point of Charge (pH pzc)	25
2.4.7	Potentiometric titration	25
2.4.8	Design of experiments	26
2.4.9	Batch adsorption study	35
3	RESULTS AND DISCUSSION	36
3.1	Results And Discussion Of Chitosan-Glyoxal/zinc oxide/ Fe_3O_4 ($CS - G/ZnO/Fe_3O_4$)	37
3.1.1	Characterization of CS-G/ZnO/ Fe_3O_4	37
3.1.2	BBD model analysis	44
3.1.3	Adsorption study	51
3.1.4	Adsorption kinetics	53
3.1.5	Adsorption isotherm	54
3.1.6	Adsorption mechanism	58
3.2	Results And Discussion Of Chitosan-glutaraldehyde/zinc oxide/ Fe_3O_4 ($CHT - GLA/ZnO/Fe_3O_4$)	60

3.2.1	Characterization of CHT-GLA/ZnO/ Fe_3O_4	60
3.2.2	BBD model analysis	66
3.2.3	Adsorption study	73
3.2.4	Adsorption kinetics	75
3.2.5	Adsorption isotherm	76
3.2.6	Adsorption mechanism	79
3.3	Results And Discussion Of chitosan-Benzil/ZnO/ Fe_3O_4 ($Cs - Bz/ZnO/Fe_3O_4$)	82
3.3.1	Characterization of Cs-Bz/ZnO/ Fe_3O_4	82
3.3.2	BBD model analysis	89
3.3.3	Adsorption study	97
3.3.4	Adsorption kinetics	99
3.3.5	Adsorption isotherm	100
3.3.6	Adsorption thermodynamics	104
3.3.7	Adsorption mechanism	106

GENERAL CONCLUSION **109**

Future Recommendations	111
----------------------------------	-----

BIBLIOGRAPHY

LIST OF TABLES

1.1	Different types of dyes and their main applications	8
1.2	chemical properties of RBBR dye.	9
1.3	The difference between chemisorption and Physisorption	11
2.1	Summary of some physico-chemical properties for materials.	17
2.2	Experimental levels of independent factors and their codes in BBD (CS-G/ZnO/ Fe_3O_4)	27
2.3	Experimental levels of independent factors and their codes in BBD (CHT-GLA/ZnO/ Fe_3O_4)	27
2.4	Experimental levels of independent factors and their codes in BBD (Cs-Bz/ZnO/ Fe_3O_4)	27
2.5	The 5-variables BBD matrix and experimental data for RB19 decolorization (CS- G/ZnO/ Fe_3O_4)	29
2.6	The 5-variables BBD matrix and experimental data for RB19 decolorization (CHT- GLA/ZnO/ Fe_3O_4)	31
2.7	The 5-variables BBD matrix and experimental data for RB19 decolorization (Cs- Bz/ZnO/ Fe_3O_4).	33
3.1	The physicochemical properties of the synthesized nanomaterials.	42
3.2	Analysis of variance (ANOVA) for RB19 decolorization.	45
3.3	PFO and PSO kinetic parameters for RB19 adsorption by CS-G/ZnO/ Fe_3O_4 NPs-25	54
3.4	Parameters of the Langmuir, Freundlich and Temkin isotherm models for RB19 adsorption on CS-G/ZnO/ Fe_3O_4 NPs-25 at 60°C	57

3.5	Comparison of the adsorption capacity of RB19 dye by various	57
3.6	The physicochemical properties of the synthesized nanocomposites.	65
3.7	Analysis of variance (ANOVA) for RBBR removal.	68
3.8	PFO and PSO kinetic parameters for RBBR dye adsorption on CHT-GLA/ZnO/ Fe_3O_4 -25.	75
3.9	Parameters of the Langmuir, Freundlich and Temkin isotherm models for RBBR dye adsorption on CHT-GLA/ZnO/ Fe_3O_4 -25 at 60 °C	79
3.10	Comparison of the adsorption capacity of RBBR dye by various adsorbents . . .	79
3.11	Material characteristics of the CS-Bz/ Fe_3O_4 , CS-Bz/ZnO-25/ Fe_3O_4 , and CS-Bz/ZnO-50/ Fe_3O_4	87
3.12	ANOVA analysis of RBBR removal.	90
3.13	Kinetic parameters for RBBR adsorption by Cs-Bz/ZnO-25/ Fe_3O_4	99
3.14	Parameters of isotherm models for RBBR adsorption by Cs-Bz/ZnO-25/ Fe_3O_4 at 60 °C	102
3.15	Comparison of the q_{max} of RBBR dye by different adsorbents.	103
3.16	Thermodynamic parameters for the adsorption of RBBR dye on Cs-Bz/ZnO-25/ Fe_3O_4	106

LIST OF FIGURES

1.1	Chemical structure of RBBR dye	9
2.1	Synthesis steps of $CS - G/ZnO/Fe_3O_4$	19
2.2	Synthesis steps of $CHT - GLA/ZnO/Fe_3O_4$	21
2.3	Synthesis steps of $Cs - Bz/ZnO/Fe_3O_4$	23
3.1	SEM-EDX analysis of (a) $CS-G/ Fe_3O_4$, (b) $CS-G/ZnO/Fe_3O_4$ NPs-25, (c) $CS-G/ZnO/Fe_3O_4$ NPs-50, and (d) $CS-G/ZnO/Fe_3O_4$ NPs-25 after adsorption of RB19 at magnification power 3000x.	38
3.2	FTIR spectra of $CS-G/ Fe_3O_4$, $CS-G/ZnO/Fe_3O_4$ NPs-25 and $CS-G/ZnO/Fe_3O_4$ NPs-25 after adsorption of RB19	40
3.3	XRD patterns of $CS-G/Fe_3O_4$, $CS-G/ZnO/Fe_3O_4$ NPs-25 and $CS-G/ZnO/Fe_3O_4$ NPs-50.	43
3.4	(a) Normal probability of the residuals, (b) observed values versus the predicted values, and (c) residual versus run	47
3.5	3D response surfaces plots of (a) AB, (b) AC, (c) BC, and (e) CD interactions; whereas, (d) pH_{pzc} of $CS-G/ZnO/Fe_3O_4$ NPs	50
3.6	(a) Effect of the contact time on RB19 adsorption at different initial concentrations	52
3.7	adsorption isotherms of RB19 by $CS-G/ZnO/Fe_3O_4$ NPs-25 (dosage = 0.06g, pH of solution = 4, temperature = 60°C, agitation speed = 100 strokes and volume of solution = 100 mL)	56

3.8	Illustration of the possible interaction between CS-G/ZnO/ Fe_3O_4 NPs surface and RB19 including (a) electrostatic attraction, (b) hydrogen bonding interactions, (c) Yoshida H-bonding, and (d) n- interactions.	59
3.9	SEM images of (a) CHT-GLA/ Fe_3O_4 , (b) CHT-GLA/ZnO/ Fe_3O_4 -25, (c) CHT-GLA/ZnO/ Fe_3O_4 -50, and (d) CHT-GLA/ZnO/ Fe_3O_4 -25 after adsorption of RBBR dye at magnification power 2000x.	61
3.10	FTIR spectra of (a) CHT-GLA/ Fe_3O_4 , (b) CHT-GLA/ZnO/ Fe_3O_4 -25, and (c) CHT-GLA/ZnO/ Fe_3O_4 -25 after adsorption of RBBR dye	63
3.11	XRD patterns of (a) CHT-GLA/ Fe_3O_4 , (b) CHT-GLA/ZnO/ Fe_3O_4 -25, and (c) CHT-GLA/ZnO/ Fe_3O_4 -50	66
3.12	Plots of (a) actual versus predicted, (b) normal probability of the residuals, and (c) externally studentized residuals versus predicted.	70
3.13	3D plots of (a) AB, (b) BC, and (d) BE significant interactions on RBBR removal; whereas. (c) pH _{pzc} of CHT-GLA/ZnO/ Fe_3O_4	72
3.14	(a) Effect of the contact time on RBBR dye adsorption at different initial concentrations	74
3.15	adsorption isotherms of RBBR by CHT-GLA/ZnO/ Fe_3O_4 -25 (dosage 0.06g, pH of solution 4, temperature 45 °C, agitation speed = 100 strokes and volume of solution = 100 mL).	78
3.16	Illustration of the possible interaction between CHT-GLA/ZnO/ Fe_3O_4 nanocomposite surface and RBBR dye including electrostatic attraction, hydrogen bonding interactions, Yoshida H-bonding, and n- interactions.	81
3.17	SEM images and EDX spectra of (a) Cs-Bz/ Fe_3O_4 , (b) Cs-Bz/ZnO-25/ Fe_3O_4 nanocomposite, and (c) Cs-Bz/ZnO-25/ Fe_3O_4 nanocomposite after adsorption of RBBR dye at magnification power 3000x.	83
3.18	FTIR spectra of (a) Cs-Bz/ZnO-25/ Fe_3O_4 , and (b) Cs-Bz/ZnO-25/ Fe_3O_4 after adsorption of RBBR dye	85
3.19	XRD spectra of (a) Cs-Bz/ Fe_3O_4 , (b) Cs-Bz/ZnO-25/ Fe_3O_4 , and (c) Cs-Bz/ZnO-50/ Fe_3O_4	88
3.20	Plots of (a) residuals normal probability, and (b) predicted vs. actual relationship of RBBR dye removal (%).	91
3.21	(a) 3D plot, and (b) 2D contour plot of the parametric interaction between AC, and (c) pH _{pzc} of Cs-Bz/ZnO-25/ Fe_3O_4	93

3.22 (a) 3D, (b) 2D contour plot of the parametric interaction between AB on RBBR removal.	94
3.23 (a) 3D response surface plot, (b) 2D contour plot of RBBR dye removal demonstrating the parametric interaction between CD.	96
3.24 Influence of initial RBBR concentrations vs. contact time on adsorption capacity of Cs-Bz/ZnO-25/ Fe_3O_4 . Experimental conditions (dose = 0.04 g, pH = 4, temperature = 60 °C, agitation speed = 100 rpm, and vol. = 100 mL).	98
3.25 Adsorption isotherms of RBBR dye by Cs-Bz/ZnO-25/ Fe_3O_4 . Experimental conditions (dose = 0.04 g, pH = 4, temperature = 60 °C, agitation speed = 100 strokes, and volume of solution = 100 mL).	101
3.26 Van't Hoff plot RBBR dye adsorption by Cs-Bz/ZnO-25/ Fe_3O_4 (dose=0.04 g, pH= 4, agitation speed = 100 strokes, and vol.= 100 mL).	105
3.27 Adsorption mechanism of RBBR dye on the Cs-Bz/ZnO/ Fe_3O_4 surface.	108

LIST OF SYMBOLS and ABBREVIATIONS

SEM	Scanning electron microscope
EDX	Energy- dispersive x-ray spectroscopy
FTIR	Fourier Transform Infrared
RBBR	Remazol Brilliant Blue R dye
RSM	Response Surface Methodology
BBD	Box Behnken design
XRD	X-Ray Diffraction
q_e	Adsorption capacity at equilibrium (mg/g)
q_t	Amount of dye adsorbed per unit of adsorbent (mg/g)
R^2	Correlation coefficient
K_L	Langmuir constant (L/mg)
K_f	Freundlinch constant
K_T	Temkin constant
C_0	Initial concentration (mg/L)
C_e	Equilibrium concentration (mg/L)
t	Time
V	Volume of adsorbate (L)
W	Weight of adsorbent (g)
PFO	pseudo-first-order
PSO	pseudo-second-order

GENERAL INTRODUCTION

Introduction

ligands of Schiff's base and their complexes have acquired particular importance in the domain of coordination chemistry^[1] because of their different possibilities of application in several fields such as homogeneous, heterogeneous catalysis, analytics^[2], biological activity as antibacterial and antifungal agents^[3] and in broad fields of magnetism^[4]. This importance is essentially attributable to the ease of synthesis of these compounds as well as their structural versatility

ligands of Schiff's base can be categorized by their numbers of chelating sites, therefore these ligands are likely to occur in a variety of sites chelating agents, commonly called "teeth", namely mono, bi, tri, tetra or polydentate. Tetradentates and hexadentates are the most studied in the literature because of their stability increased^[5], induced by the chelating sphere which perfectly encases the metal ion. This form of complex is observed in those of cytochrome P450 enzymes^[6] present mainly in the liver as well as in that of blood hemoglobin.

In same context, ligands of Schiff' base have been interested through preparation ,characterization and applying for removing of anionic dye .

- **Background of Study**

Water is one of the most important elements for the survival of the human race^[7], It also plays a major role in the sustainable development of urbanization, industrialization, and agricultural activities^[8]. However, Population explosion, and Water pollution due to the release of polluted effluents into the water bodies by irresponsible parties caused by the industrial revolution, It become the most important issue of environmental stress and a source of concern for many critical problems facing all over the world especially for undeveloped countries and causing millions of death annually parties^[9] Among these pollutants have attracted the attention of environmentalists as one of the most harmful organic pollutants is Synthetic dyes^[10] which are widely used such as textile, paper and pulp, tannery, and pharmaceutical owing to their low production cost, vivid colors, resistance towards environmental factors, and easy-to-apply factor^[11],^[12]. The discharge of these dyes without treatment into water is one of the environmental problems due to its risks on aquatic life and human's health^[13]. Thus, it is recommended that these organic dyes be correctly disposed of before being released into the aquatic environment to maintain ecosystems^[14].

Till now, There are several techniques that have been used for the removal of dyes such as adsorption^[15], coagulation^[16], photocatalytic degradation^[17], oxidation^[18], membrane filtration^[19],

electrochemical reaction^[20], and cation-exchange membrane^[21]. Whilst, these treatment methods either possessed low efficiency which limits the effectiveness of the process, high operating costs or generation of harmful substances and time-consuming^{[22], [23]}. adsorption is a very effective technique due to its high selectivity^[24], regeneration, low-cost, and designability^[25].in addition, the production of harmful substances in adsorption is reduced compared to other methods^[26]These ideal features of adsorption make it one of the most important techniques to confront dangerous environmental threats.

Therefore, The current work is focused on treating dye pollutants from wastewater by adsorption technique through the preparation of some ligands from a kind of bi -Schiff's base functions which are obtained through condensation or crosslinking reactions between biopolymer (chitosan) contains amine firstly group and bi-carbonyl. These prepared ligands have also been enhanced by zinc oxide nanopomposite to improve the surface area.Furthermore, adsorption operation parameters (adsorbent dose, solution pH, temperature, and contact time) are optimized by BoxBehnken design.

- **Problem Statement**

One of the most alarming crises happening in society is water pollution due to the increasing number of industrialization. The evolution has caused water pollution contributed mostly by dyes and discharged freely into water bodies without being treated. Adsorption has been found to be an efficient method for the removal of dyes from effluents because it produces high-quality treated effluent. Recently, the attention has been focused on naturally occurring waste biomaterials for color removal owing to their huge availability, biodegradability, and low cost such as chitosan Raw chitosan shows low mechanical properties, serve shrinking, deformation after drying, is compressible at high operating pressure, and soluble in many organic acids in addition to high crystallinity and hydrophobicity. Raw chitosan has also low surface area and non-porosity thus the dye molecules cannot easily penetrate onto the surface structure. Therefore, a decrease in adsorption capacity and rate due to poor access to internal adsorption sites might occur. Moreover, nanoZnO has post-treatment issues in the removal of the adsorbent, making it unviable for either a batch mode or column mode operation in large-scale applications. Thus, in order to make use of the sorption efficiency of the nano-ZnO, it is important to be able to prepare them in a useable format, such as beads of regular size and shape.

- **Significance of Study**

The significance of this study is to synthesize hybrid biocomposite beads by modifying three types of cross-linked chitosan glyoxal, glutaraldehyde, and benzil with different impregnation ratios of nano-ZnO. Preparing organic/inorganic hybrid composite material by adding nanoscale of ZnO into the molecular structure of cross-linked chitosan beads can improve the adsorptive properties of the biopolymer, reducing the crystalline state, enhancing the inner surface of the polymeric structure, and speeding up the diffusion rate of water pollutants into chitosan polymeric structure.

- **Research Objectives**

Although efforts have been made to develop various dye removal techniques, there are many challenges associated with them, for example, the high production cost, the use of many toxic chemicals including organic solvents, which raises concerns about their environmental impact as they are derived from non-renewable and non-renewable sources. Biodegradable. Natural polymers or biopolymers including cellulose and chitosan are considered a distinct leap that aroused the interest of many researchers in the removal of dyes due to their high percentage, low cost, and tunable properties such as surface area and pore size. Biopolymers are biodegradable and have an additional advantage over synthetic materials, and do not show any negative impact on the environment or living organisms. Biocompatible biopolymers derived from renewable sources, the use of chitosan as an excellent in wastewater treatment has some limitations such as low chemical stability, low surface area, solubility in many organic acids and low mechanical strength. In general, there are methods that can be used to improve the properties of chitosan such as chemical bonding reaction and synthesis of nanoparticles in a matrix of chitosan. Thus, the main objectives of the current study are:

- ✓ To prepare three adsorbents type of Schiff's base bi-functions followed by using glyoxal, glutaraldehyde, and benzil as cross-linking agents
- ✓ To characterize the adsorbents using scanning electron microscopy (SEM), Fourier-transform infrared (FTIR) spectroscopy, and energy-dispersive x-ray (EDX) spectroscopic techniques.
- ✓ To analyze experimental data by using isotherm models and Kinetic studies to evaluate the Adsorption behavior process
- ✓ To evaluate the performance of prepared nanocomposites for removal of textile dyes from aqueous solution by response surface methodology (RSM).

- **Novelty of study**

The novelty of this study can be recognized in the preparation of biocomposites as adsorbents to absorb RBBR anionic dye as a pollutant and harmful to the environment. Several researchers have prepared composites of Schiff's base by using Chemical modifications of chitosan to adsorb the anionic dye, however, the adsorbents used were prepared to contain Schiff bases but were in a limited range and have no magnetic properties. However, the results revealed that there is a gap in this area. Hence, this is the main motivation for this study.

- **Thesis Layout**

This thesis is organized into three chapters :

Chapter 1 discusses the literature related to the current work such as sources of wastewater in the surface medium. In addition to, the technique has been used for cleaning technology of dyes. as well as using Schiff's base composites for the removal of this pollutants water.

Chapter 2 presents materials and chemicals employed, synthesis of three bio composites which carrying bi- Schiff's base functions .therefor, the instruments has been utilised a flow chart of the methodology,

Chapter 3 presents the research findings. The preliminary study is firstly discussed, followed by the characterization, optimization, and modeling of selected adsorbent. The reaction mechanism is also discussed in this chapter.

At the end of this work was general conclusion which summarizing the main of obtained results and offering some recommendations for future work

CHAPTER 1

LITERATURE REVIEW

1.1 Introduction

This chapter is contained at three main parts which are the pollutant, technique of treatment this pollutant, and some researches. The first part describes about a brief history of dyes, types, and their toxicities. The second part also explains with the best low cost technique for removing the dye which is the adsorption. Lastly, It was supported by some researches in order to validate in this research.

1.2 Dyes

Since the beginning of civilization, mankind has fascinated by colors, where he had expressed his feelings and thoughts in the form of painted images, and his cultures have wonderful been left distinctive an imprint to of peoples all over the world^[27]. Dyes are basically chemical compounds that a water-soluble, and can connect themselves to surfaces or fabrics to impart color^[28]. The majority of dyes are complex organic molecules and consist of two components which are chromophores (the part of a molecule responsible for its color, e.g: $-N=O$, $-C=C-$, $-C=O$) and auxochromes (A functional group that modifies the light absorbance, e.g: $-OH$, $-NH_2$, $-COOH$.)^[29].

Dyes are used in different industries of an advanced technologies such as in various kinds of textile^[28], leather tanning^[30], paper^[31], and food processing, plastics, cosmetics, rubber, printing, and dye manufacturing industries^[32]. Currently, the textile industry is one of the largest consumers of dyes produced annually^[33] Total dye production is estimated at 7×10^5 tonnes per year of which the textile industry consumes 10,000 tonnes per year and discharges 1000 tonnes/year into water bodies^[34]

1.2.1 Classification of dyes

There are many ways that can be classified for the classification of commercial dyes of which colour effectively^[35], molecular structure, and application methods^[36]. Other than the above, dyes are also usually classified based on their particle charge upon dissolution in aqueous application medium^[37,38] such as anionic (direct, acid, and reactive dyes), non-ionic (dispersed dyes), and cationic (all basic dyes). The following (table: 1.1) shows various types of dyes.

Table 1.1: Different types of dyes and their main applications

Type	Water Solubility	Applications	Common Application Method	Example
Acid	<i>Soluble</i>	Cosmetics, food, leather , modified acrylics, nylon , paper, printing ink , silk and wool	In dye baths with neutral to acidic conditions	Acid Yellow 36
Azo	<i>Soluble/insoluble</i>	Acetate, cellulose, cotton , rayon and polyester	Coupling component used to impregnate fiber and a solution of stabilized diazonium salt is used for treatment	Bluish Red azo dye
Basic	<i>Soluble</i>	Inks, medicine, modified nylon, modified polyester , paper, polyacrylonitrile, polyester	In dye baths with acidic conditions	Methylene Blue
Direct	<i>Soluble</i>	Cotton, leather, nylon, rayon, silk and paper	In dye baths with neutral or slightly alkaline conditions with additional electrolyte.	Direct Orange 26
Disperse	<i>Insoluble</i>	Acetate, acrylic fibers, cellulose, cellulose acetate	Padded on cloth and either baked or thermo-fixed at high pressure and temperature or low temperature carrier methods	Disperse Red 4
Reactive	<i>Soluble</i>	Cellulosic, cotton, nylon, silk and wool	reactive group on dye. Covalently bonding under heat and alkaline pH	Reactive Blue 5
Solvent	<i>insoluble</i>	Fats, gasoline, inks, lacquers, lubricants, oils, plastics, stains, varnishes and waxes	Substrate dissolution	Solvent Red 26

Among these kinds of dyes The dye Remazol Brilliant Blue Reactive (RBBR) which was highlighted in this research. RBBR or RB19 is one of the most widely used synthetic dyes in the textile industry because of its properties such as water solubility^[39], simplicity in utilization, and resistance to degradation due to its anthraquinone structure^[40]. as it has widely been applied to cotton substrates, providing a wide range of bright and colorful tones^[41].

(**Table:** 1.2) and (**Figure:** 1.1) display some chemical properties and chemical structure of RBBR dye.

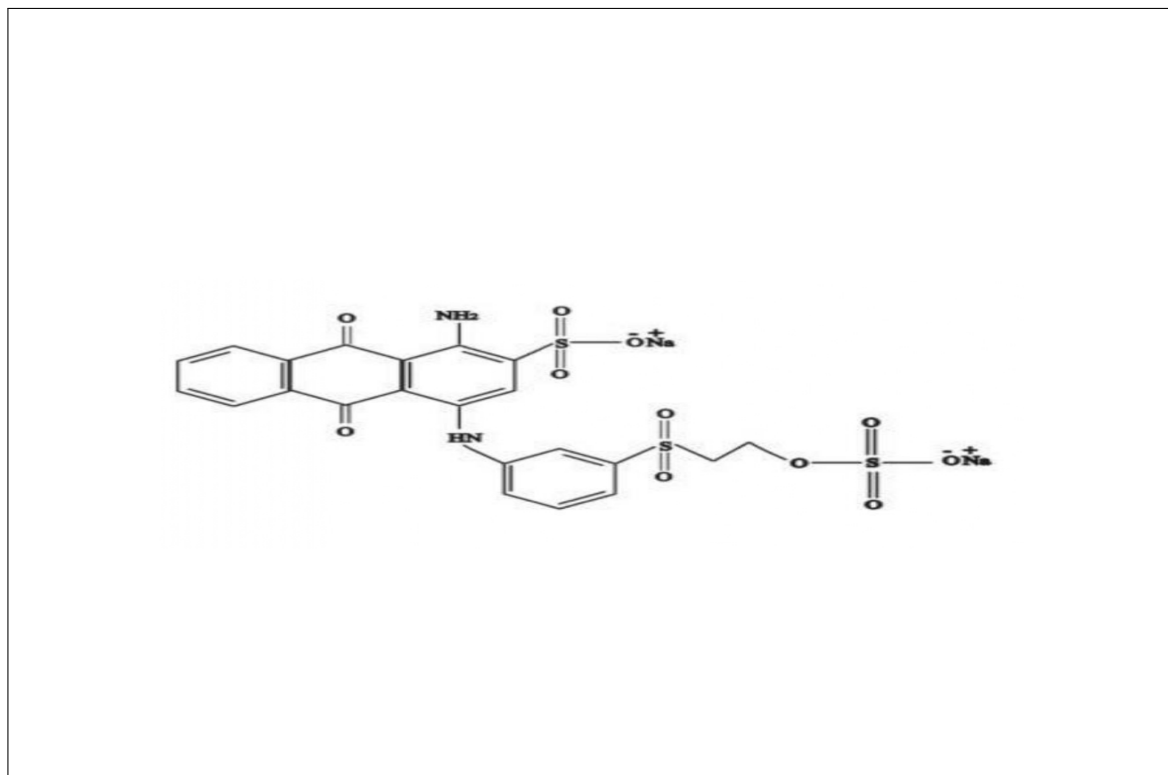


Figure 1.1: Chemical structure of RBBR dye .

Table 1.2: chemical properties of RBBR dye.

Commercial name	Remazol Brilliant Blue Reactive
Generic name	Reactive Blue 19
Abbreviation	RBBR
Functional group	Anthraquinone
Molecular mass (g/mol)	626.54
λ max (nm)	590
Molecular formula	$C_{22}H_{16}N_2Na_2O_{11}S_3$

1.2.2 Toxicity effects of dyes

Basic dyes have high intensity of colours and are greatly visible even in very little concentration^{[36], [42–46]}. The complex dyes are generally chromium based, which is carcinogenic^[36,37,47]. Dyes may affect the photosynthetic activity in aquatic life due to decreased light penetration

and may also be toxic to some aquatic life due to the presence of metals, aromatics, etc. Furthermore, dyes are also carcinogenic, mutagenic, or teratogenic in various microbiological, fish species. Additionally it can also cause severe damage to human beings such as dysfunction of the kidney, reproductive system, liver, brain and central nervous system^[48]. Azo dyes are toxic because of the presence of toxic amines in the effluent^[49]. Similarly anthraquinonebased dyes are most resistant to degradation and remains colour for a large time in effluents^[49]. Reactive dyes are water soluble and 510% of the dyes go in the dye bath giving highly coloured effluent causing serious troubles in the environment^[50]. Additionally, reactive dyes that are chemically stable and having little biodegradability are likely to pass through conventional treatment plants untreated, so their elimination is of great importance.

1.3 Adsorption

Adsorption has been known for a long time for the treatment of water, and medicinal purposes^[51]. The word adsorption was used due to differentiate between two terms: The positioning of molecules at the surface and the penetration of molecules into the surface^[52]. Adsorption is a phenomenon that occurs at the surface's interfaces, a surface process that leads to the accumulation of a substance (an atom an ion, or molecule) on the solid surface from its gaseous or liquid surroundings. The solid surface on which the adsorption process occurs is called the adsorbent, and the substance that accumulates on the surface of the solid is called the adsorbate^[53].

Depending upon the nature of the process, and forces bondings, there are two main types of adsorption processes that may be distinguished chemical sorption(chemisorption) and physical sorption(Physisorption)^[54],^[55].

- chemical sorption(chemisorption): Chemisorption is described the kind of bonding which occurring between the adsorbent surface and molecules or ions of adsorbate^[56]. as changes occur in the molecular structure and energy is released in this range [20-200 kj/mol]^[57].
- physical sorption(physisorption): Physical adsorption is also called van der Waals adsorption because It illustrates the nature of the weak link between the adsorbate and adsorbent including hydrogen bonding. usually rapid and readily reversible. Although weak individually^[58].It also produces energy less than 40 kj/mol.

The following ([Table: 1.3](#)) shows the difference between chemisorption and Physisorption

Table 1.3: The difference between chemisorption and Physisorption

Properties	Chemisorption	Physisorption
bonding type	chemical bonds	van der Waals bond
layer kind	mono layer	mono, or multi layers
	slowly and irreversibly	rapid and reversibly
adsorption heat	more than 10 K Cal/mol	less than 10 KCal/mol
	needs to an activation energy	does not need to an activation energy

1.3.1 Factors impacting the Extent of Adsorption

There are principal factors that affect the adsorption effectiveness for instance: The initial dye concentration, temperature, pH, contact time, adsorbent dosage, and adsorbent particle size^[59]. Optimization of such conditions will greatly help in the development of the industrial-scale dye removal treatment process. In the next section, some of the factors affecting the adsorption of dyes are discussed.

■ Effect of initial dye concentration: The amount of adsorption for dye removal is highly dependent on the initial dye concentration. The effect of initial dye concentration depends on the immediate relation between the concentration of the dye and the available sites on an adsorbent surface. In general, the percentage of dye removal decreases with an increase in the initial dye concentration, which may be due to the saturation of adsorption sites on the adsorbent surface. On the other hand, the increase in initial dye concentration will cause an increase in the capacity of the adsorbent and this may be due to the high driving force for mass transfer at a high initial dye concentration^[60].

■ Effect of temperature: Effect of temperature is another significant Physico-chemical process parameter because the temperature will change the adsorption capacity of the adsorbent^[61]. If the amount of adsorption increases with increasing temperature then the adsorption is an endothermic process. This may be due to the increasing mobility of the dye molecules and an increase in the number of active sites for the adsorption with increasing temperature. Whereas the decrease of adsorption capacity with increasing temperature indicates that the adsorption is an exothermic process. This may be due to increasing temperature decreasing the adsorptive forces between the dye species and the active sites on the adsorbent surface as a result of decreasing the amount of adsorption^[62].

■ Effect of solution pH: One of the most important factors affecting the capacity of adsorbents in wastewater treatment is solution pH. The efficiency of adsorption is dependent on the solution pH since variation in pH leads to the variation in the degree of ionization of the adsorptive molecule and the surface properties of the adsorbent^[63].

■ Contact time: The longer the time the more complete the adsorption will be. However, the equipment will be larger. The boundary layer resistance will be affected by the rate of adsorption and increase in contact time, which will reduce the resistance and increase the mobility of dye during adsorption^[64].

■ Effect of amount of adsorbent: Adsorbent dosage is an important process parameter to determine the capacity of an adsorbent for a given amount of the adsorbent at the operating conditions. Generally, the percentage of dye removal increases with increasing adsorbent dosage, where the quantity of sorption sites at the surface of the adsorbent will increase by increasing the amount of the adsorbent. The effect of adsorbent dosage gives an idea for the ability of dye adsorption to be adsorbed with the smallest amount of adsorbent, so as to recognize the capability of a dye from an economical point of view^[62].

■ adsorbent particle size: Smaller particle sizes reduce internal diffusional and mass transfer limitation to the penetration of the adsorbate inside the adsorbent (that is, equilibrium is more easily achieved and nearly full adsorption capability can be attained). However, wastewater drop across columns packed with powdered material is too high for use of this material is packed beds. The addition of powdered adsorbents must be followed by their removal.

Therefore, the researchers shifted towards natural biopolymers and waste materials as economical alternative adsorbents^[65]. Various types of adsorbents such as chitosan, cellulose, cotton, fly ash, clay, biomass, and sludge were applied in the adsorption process for removals of dyes^[66-72]. In recent years, chitosan and chitosan derivatives have been widely applied as adsorbents due to their low-cost, high adsorption capacity and, being environmentally friendly^[73,74].

1.3.2 Use of Schiff's base for adsorption of synthetic dyes

Schiff bases are named in honor of Hugo Schiff (1834-1915), the Italian-German chemist who synthesized the first members of this class of products containing an azomethine or imine group in 1864^[75,76].as have been synthesized by condensation reaction between a carbonyl compound (aldehyde or ketone) with a primary amine under distillation.

Schiff bases are the most among common organic compounds, they have been used in a

broad range of applications, such as food industry^[77,78], organic synthesis^[79–82], dye^[83–85], and catalysis^[86,87].

1.3.2.1 Chitosan

Chitosan is an important biopolymer which was discovered in 1859 by Professor C. Rouget^[88–90]. Chitosan is a linear polysaccharide consist of 2-amino-2-deoxy--D-glucopyranose units^[91]. Chitosan is considered from most important derivatives of chitin which is a mainly produced from marine organisms such as shrimp and crabs, in addition to insects and fungi^[92–94]. Cs has several significant characteristics e.g non-toxicity, biodegradability, antimicrobial activity, and biocompatibility^[95]. It is unique due to the existence of two groups namely hydroxyl (-OH) and amino ($-NH_2$) in its backbone^[40]. These unique functional groups in Cs backbone can be effectively utilized for capturing various types water pollutants such as dyes^[96], and metal ions^[97]. However, the application of unmodified Cs in waste water treatment is still limited because of solubility of Cs in drastic acidic environments, considerable leachability, and low surface area^[98].

chitosan/derived Schiff's base (mono function) has been synthesized by Fadi Alakhras and his researchers for uptaking of Cationic Rhodamine B Dye from Aqueous Solutions^[99]. the obtained composite showed that enhancing mechanical properties of chitosan through Chemical modification. Also, the adsorption capacity was 233.4 mg/gm (25°C), while the kinetic data were better fitted using nonlinear pseudo-first-order.

Ali H. Jawad and his co-workers prepared Schiffs Base (bi-functions) Chitosan-Glutaraldehyde as a promising adsorbent for the effective removal of cationic dyes from aquatic media^[100]. the obtained findings demonstrated that TH dye adsorption on the Ch-Glu/AC surface obeyed the pseudo-first order (PFO) kinetic model, The maximum adsorption capacity (qm) of the TH dye was 30.8 mg/g at 50 °C, and the Freundlich isotherm was obeyed at equilibrium.

Nurul Najwa AbdMalek and her team synthesized Schiff's base(bi -functions)-chitosan-glyoxal/fly ash/ Fe_3O_4 in order to remove the anionic azo dye^[101]. Response surface methodology was used to optimize the factors affecting on adsorption process efficiency of chitosan/-glyoxal/fly ash/ Fe_3O_4 such as pH solution, time, dye concentration, and adsorbent dose. The results showed efficiency using of chitosan/-glyoxal/fly ash/ Fe_3O_4 as a candidate adsorbent with the optimum conditions following: pH solution - 4, adsorbent dose (0.1 g), temperature (40 °C), and contact time (12.5 min). According to the results of kinetics and isotherms models

indicate that the adsorption was affected by chemisorption and heterogeneous model of adsorption. The q_{max} of Chi-Gly/FA/ Fe_3O_4 biocomposite for anionic azo dye was 112.5 mg/g at 40 °C.

Leila YavariMaroufi et al^[102] reported the fabrication of a novel antibacterial based on chitosan and dialdehyde guar gum (DAGG). The results showed both good antioxidant (81.13%) and antimicrobial activities. The hydrogel was observed to have a good potential to be used as an antibacterial pad.

Rahime Eshaghi Malekshah et al^[103] have developed many complexes that contain Schiff's base chitosan with several transition metals such as Cu(II), Ni(II), and Zn(II) to decrease cancer activity for some cells. The investigated findings confirmed that the anticancer activity of Schiff base and their complexes were much better than that of pure CS against cancer MG63 cell line. through flow cytometry has demonstrated that all compounds were efficient in inducing the apoptosis effect in K562 and MG63 cell lines except Schiff base-chitosan in K562 cell lines.

Chitosan Schiff Base Salicylaldehyde^[104] was complexed with $MnCl_2 \cdot 4H_2O$ by Ismiyati and his group to inhibit bacteria activity from the kind of Staphylococcus aureus and Escherichia coli. The product revealed that the Mn(II) Complexes-Carboxymethyl Chitosan Schiff Base-salicylaldehyde was a black solid with a yield of 59% (w/w) and has antibacterial activity against Staphylococcus aureus (clear zone diameter 13 mm) and Escherichia coli (clear zone diameter 17 mm).

CHAPTER 2

METHODOLOGY

2.1 Introduction

All experiments for this research work were conducted at three main laboratories namely: Laboratory of Molecular Chemistry and Environment at University of Biskra, Laboratory (5) Faculty of Technology University of El Oued, and Laboratory (105) in Faculty of Applied Sciences Universiti Teknologi MARA (Malaysia).

This chapter is made up of three essential parts which we can be summarized as follows: the first part displays the preparation of the biocomposites which are: $CS-G/ZnO/Fe_3O_4$, CHT-GLA, $/ZnO/Fe_3O_4$), lastly Cs-Bz/ ZnO/Fe_3O_4) based they are as among the best a promising and recoverable adsorbent for uptaking the pollutants like synthetic dyes (RBBR) from water bodies. these biocomposites that have been mentioned involve imine function it is also called Schiff's base. These last are obtained through a condensation reaction. Noteworthy that the Benzil crosslinker was synthesized through a series of reactions beginning with benzaldehyde.

regarding the second part explains the instruments for an instant: SEM, BET, FTIR ... and various techniques like pH pzc, Potentiometric titration that has used for this work.

According to third part illustrates looking for optimum adsorption operation parameters by BoxBehnken design.

2.2 Materials and Chemical Solvent used

Several materials and chemicals solvent were used for this work such as: Benzaldehyde, Chitosan Flakes, and Ethanol...etc. The below ([Table: 2.1](#)) exhibit : Name, Chemical formula, Properties, and company of industry these materials.

Table 2.1: Summary of some physico-chemical properties for materials.

No	Name	Chemical formula	Properties	Company
1	<i>Benzaldehyde</i>	C_7H_6O	Liquid , MW= 106.12 g/mol, d= 1.05g/cm ³	Fluka
2	<i>Zinc Oxide</i>	ZnO	Powder, P= 99 %	Sigma-Aldrich
3	<i>Chitosan Flakes</i>	Biopolymer	Powder, deacetylation around (75%), medium molecular weight	Sigma-Aldrich
4	<i>Remazol Brilliant Blue R (RBBR)</i>	$C_{22}H_{16}N_2Na_2O_{11}S_3$	Powder , max = 592 nm, MW = 626.53 g/mol	Sigma-Aldrich
5	<i>Acetic Acid</i>	CH_3COOH	Liquid, colorless, MW= 60.05 g/mol	Hmbg Chemicals
6	<i>Glutaraldehyde</i>	$C_5H_8O_2$	Liquid , MW= 100.1 g/mol, Boiling point =187 °C	SigmaAldrich
7	<i>Sodium Hydroxide</i>	NaOH	white powder, soluble in water, d= 2.13g/cm ³	R and M Chemicals
8	<i>Ethanol</i>	C_2H_6O	Colorless Liquid, MW= 46.07 g/mol, Boiling point =78.4 °C	Biochem

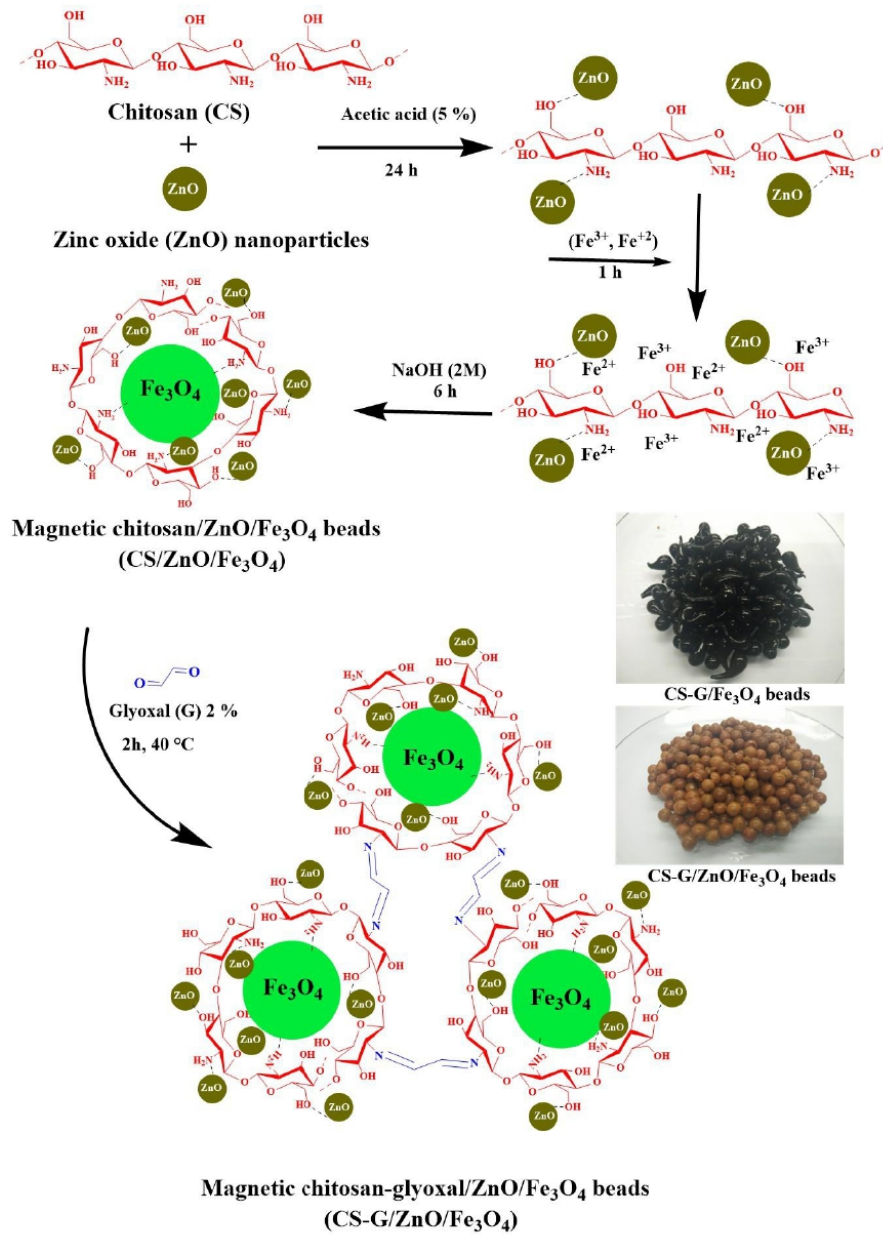
2.3 Synthesis of Schiff's base Composites

It should be mentioned that the use of three kinds of compounds which containing two carbonyls function (glyoxal, glutaraldehyde, as well as benzil) in order to obtain Schiff base reaction, where the last one was prepared at the laboratory.

2.3.1 Preparation of Chitosan-Glyoxal/ZnO/ Fe_3O_4 (CS - G/ZnO/ Fe_3O_4)

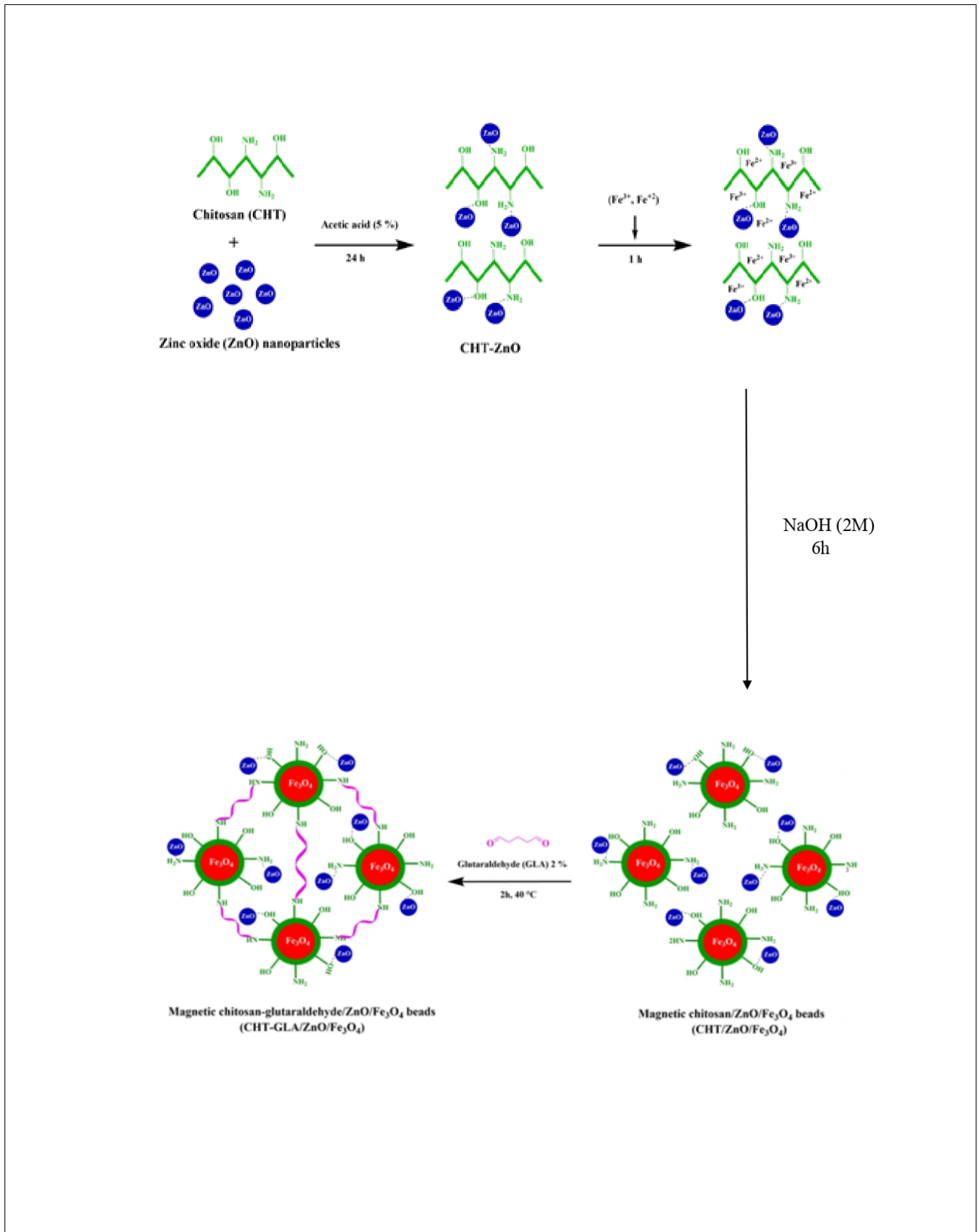
1 g of CS flakes was dissolved in CH_3COOH acid solution (60 mL, 5% v/v), and then magnetically stirred at 25°C until it becomes a homogeneous viscous solution. Next, 10 mL aqueous solution of Fe (III) and Fe (II) salts with a molar ratio (2:1) was added to CS solution while stirring for 60 min. The CS/Fe_3O_4 beads were achieved by injecting droplets of the mixture solution through a syringe needle into aqueous NaOH solution (2 M). The formed beads (CS/Fe_3O_4) were rapidly washed with distilled water in order to remove any trace of NaOH and attaining a neutral pH. Cross-linking step of the CS/Fe_3O_4 beads was performed by transferring the beads to flask containing 80 mL Glyoxal (2 %) with gentle stirring in a thermostat laboratory shaker at 40 °C for 2 h. Then, the resulting composite (CS-G/ Fe_3O_4) was washed with distilled water and dried in an oven for 24 h at 60°C. For comparison purpose, chitosan-glyoxal/ZnO/ Fe_3O_4 nanoparticles were synthesized by loading various ratios (wt.%) of ZnO nanoparticles with chitosan before adding to CH_3COOH solution, viz., 25:75 wt.% (ZnO:CS), which was labeled as CS-G/ZnO/ Fe_3O_4 NPs-25, and 50:50 wt.% (ZnO:CS), which was labeled as CS-G/ZnO/ Fe_3O_4 NPs-50. At last, the synthesized composites were crushed and then sieved at a constant particle size (250 m) for the RB19 dye removal experiments. The synthesis procedure of the CS-G/ZnO/ Fe_3O_4 beads is schematically illustrated in

(**Figure:** 2.1).

Figure 2.1: Synthesis steps of *CS – G/ZnO/Fe₃O₄*

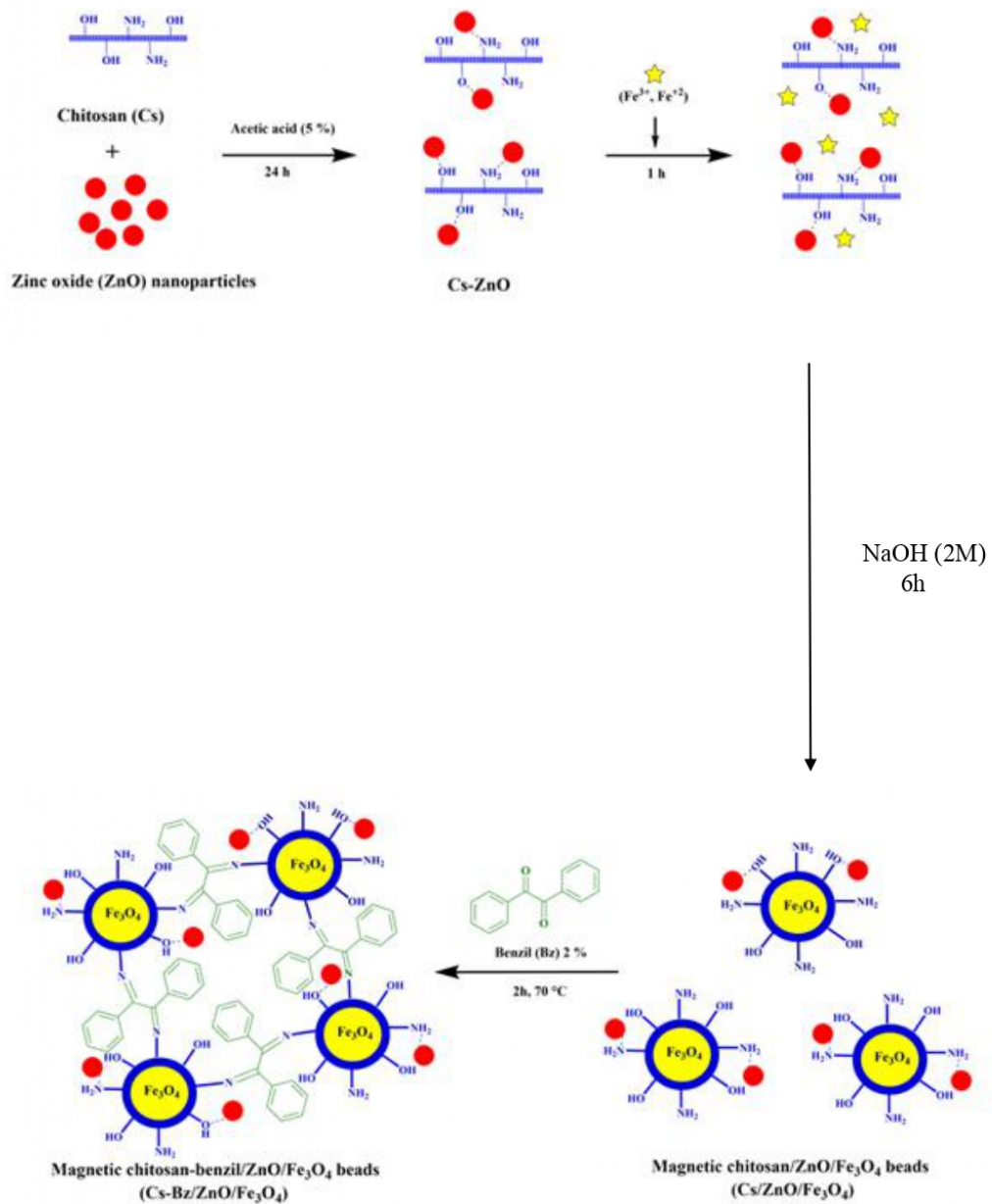
2.3.2 Preparation of chitosan-glutaraldehyde/ZnO/ Fe_3O_4

1 g of CHT flakes were poured in 60 mL of CH_3COOH acid solution (5% v/v) and agitated at 550 rpm on a magnetic stirrer for 24 h at 25 °C to dissolve CHT flakes. Subsequently, 10 mL aqueous solution of Fe^{3+}/Fe^{2+} ions (3.9 g $FeCl_3 \cdot 6H_2O$ and 2.7 g $FeCl_2 \cdot 4H_2O$) was added to CHT solution with stirring for 1 h. The magnetic CHT/ Fe_3O_4 beads were obtained by dropping of the mixture solution as drops into 1000 mL of NaOH solution (2 M). The resulting magnetic CHT hydrogel beads were washed with distilled water until become neutral. Cross-linking process of the magnetic beads was accomplished by adding them into flask containing 80 mL GLA (2 %) with mild stirring in shaker bath incubator at 40 °C for 2 h. The resultant was washed and then dried at 60 °C overnight in oven to get the final CHT-GLA/ Fe_3O_4 composite. For the purpose of comparison, chitosan-glutaraldehyde/ZnO/ Fe_3O_4 nanocomposite was prepared by mixing different ratios (wt.%) of ZnO nanoparticles with chitosan before adding to CH_3COOH solution, i.e. 25:75 wt.% (ZnO:CHT), which was named as CHT-GLA/ZnO/ Fe_3O_4 -25 and 50:50 wt.% (ZnO:CHT), which was named as CHT-GLA/ZnO/ Fe_3O_4 -50. Ultimately, the synthesized composites were pulverized and then sieved at a particle size (250 m) for further use. (Figure: 2.2). demonstrates the fabrication steps of the CHT-GLA/ZnO/ Fe_3O_4 nanocomposite.

Figure 2.2: Synthesis steps of *CHT* – *GLA*/*ZnO*/*Fe*₃*O*₄

2.3.3 Preparation of chitosan-Benzil/ZnO/ Fe_3O_4

50 mL of ethanoic acid (5%) was used to convert 1 g of Cs flakes into homogeneous Cs gel solution under gentle stirring for 24 h. After that, 10 mL aqueous solution of Fe(III) and Fe(II) salts were added to Cs gel solution and stirred for 60 min. Then, the viscous mixture was injected by a syringe needle into 500 mL of NaOH solution (2M) to form magnetic hydrogel beads of Cs/ Fe_3O_4 , which were eventually washed with distilled water to achieve a neutral pH. The crosslinking reaction was carried out to form Schiff's base-Cs derivative by adding 100 mL of 2% Bz before being placed inside a thermostat water bath shaker for 2 h at 70°C to form a Schiff's base Cs-Bz/ Fe_3O_4 . The preparation of nanocomposites nanoparticles of Cs – Bz/ZnO/ Fe_3O_4 was performed by direct mixing of ZnO nanoparticles powder at different ratios 25% and 50% with Cs flakes before adding ethanoic acid solution. The above-mentioned procedure of beads preparation was repeated to produce nanocomposites Bz/ZnO – 25/ Fe_3O_4 (Cs75% + ZnO25%), and Cs – Bz/ZnO – 50/ Fe_3O_4 (Cs50% + ZnO50%). Then, the obtained Cs – Bz/ Fe_3O_4 , Cs – Bz/ZnO – 25/ Fe_3O_4 and Cs – Bz/ZnO – 50/ Fe_3O_4 beads materials were crushed and sieved into certain particle size 250 μ m. The synthesis steps of Cs – Bz/ZnO/ Fe_3O_4 are exhibited in (Figure: 2.3).

Figure 2.3: Synthesis steps of *Cs* – *Bz*/ZnO/*Fe*₃O₄

2.4 Instrumentation

In order to characterize the compounds that have been prepared in this study, various analytical techniques were used as follows:

2.4.1 Scanning Electron Microscopy (SEM)

SEM is one of the most fascinating analysis techniques to photograph the topography of the compound's surfaces. The working principle is based on shedding a beam of electrons into the samples that had already been coated with gold by a Polaron SC 515 sputter coater to make the samples electrically conductive, through this collision produces many signals which are treated and transforming in the form of images. It should be noted that the samples were examined with scanning electron microscope with energy dispersive X-ray analyzer (SEM-EDX, Hitachi, TM3030Plus, Tabletop Microscope, Japan)

2.4.2 Fourier Transform Infrared Spectroscopy (FTIR)

The fundamental functional groups of the samples were identified by FTIR spectrometer (Perkin-Elmer, Spectrum RX I), A thin and transparent pellet was prepared from of mixture the sample with potassium bromide, after milling and compressing by mortar with pestle and hydraulic press respectively. Then, it is placed in the cell holder and is inserted into FTIR spectrophotometer to be analyzed. All the spectra were recorded within the wavenumbers range of 4000-450 cm^{-1} .

2.4.3 Brunauer-Emmett-Teller (BET)

Brunauer-Emmett-Teller (BET) analysis was used in order to estimate surface area (m^2/g), Total pore volume (cm^3/g), and Mean pore diameter (nm). The above-mentioned characteristics were achieved by a surface area analyzer (Micromeritics, Model ASAP 2020, USA).

2.4.4 X-Ray Diffraction (XRD)

Ray diffraction model XPert PRO, PA nalytical, USA was used to give information about crystal structure and lattice parameters Diffraction data is acquired by exposing powder samples to X-ray radiation, which has a characteristic wavelength (λ) of 1.5418 Å. Cu-K X-rays were generated from a Cu anode supplied with 40 kV of voltage and a current of 40 mA.

2.4.5 Elemental Analysis (CHN)

The samples were determined by using the CHN/O analyzer (Perkin-Elmer, Series II CHNS/O Analyzer, 2400) at the combustion temperature of 925 °C and at reduction temperature of 640 °C. During the analysis, samples were ground and dried properly under oven at 100 °C overnight prior to analysis to ensure there are no error occurred during the weighing process. The instrument was purged using a mixture of pure oxygen and helium gas. The calibration standard was acetanilide. Precision and accuracy of the results are within 2-3%.

2.4.6 Zero Point of Charge (pH pzc)

Among the analysis techniques that determine kind of the surface charge of samples (positive, negative or zero) is Jeon and Holl technique (Dalvand, A., Nabizadeh, R., Ganjali, M. R., Khoobi, M., Nazmara, S., Mahvi, A. H. 2016). regarding the working mode as follows :100 ml of NaCl solution (0.01N) was taken into a series of conical flasks (pH 2 to 12) after adjusting by using aqueous solution 0.01 N HCl or 0.01 N NaOH. In this regard, the initial pH values were recorded by using pH meter (Metrohm, 827 pH lab). Thereafter, 100 mg of each adsorbent were mixed with these solutions, and the mixture was then left agitated for 24 h on shaker bath incubator at 100 rpm to obtain the final pH. pH vs pH was plotted where pH_{pzc} point is the intersection of the curve with pH straight line.

2.4.7 Potentiometric titration

pH-potentiometric titration was carried out to determine the amine content in the samples based on the method published by vieira and beppu^[105]. In this method, adsorption sites on the surface were activated by adding 50 ml of HCl solution (0.02 N) into Erlenmeyer flask containing 0.1 g of each adsorbent, where the mixture was incubated for overnight. After that, the solution has been obtained was titrated against NaOH solution (0.01 N). The pH of the solution was monitored by pH meter (methrohm, 827 ph lab) with a calibrated pH sensitive glass electrode whereby an interval time of 2 min was allowed before adding more NaOH. The percentage of amino content was calculated using (equation: 2.1)^[105]:

$$\%NH_2 = \frac{MNaOH(V_2 - V_1) \times 161}{W} \times 100 \quad (2.1)$$

where :

M NaOH : the molarity of sodium hydroxide solution (M)

$V_2 - V_1$: the used volume of NaOH (L)

161: the molecular weight of the chitosan monomer

W: the mass of adsorbent before titration (g)

According to $V_2 - V_1$ values, it can be inferred them straight from the titration curves. simultaneously, this values signify to The volume of acid consumed by the amino ($-NH_2$)groups.

2.4.8 Design of experiments

A preliminary test was carried out in order to select the main impactful factors, and their working ranges. After that, BBD was applied as mathematical and statistical tool for optimizing the synthesis and adsorption inputs such as ZnO loading, adsorbent dose, solution pH, contact time, and temperature towards uptaking RBBR dye as a response (output). The BBD and statistical data analysis were done using Stat-Ease Design-Expert (Version 11) software.

(Tables: 2.2, 2.3, 2.4) show different experimental levels of independent factors and their codes for CS-G/ZnO/ Fe_3O_4 , CHT-GLA/ZnO/ Fe_3O_4 , and Cs-Bz/ZnO/ Fe_3O_4 . A second-order polynomial model was employed for analyzing and predicting the RBBR decolorization as shown in the following (equation 2.2) :

$$Y = \beta_0 + \sum \beta_{ii}X_i^2 + \sum \sum \beta_{ij}X_iX_j \quad (2.2)$$

where (Y , X_i and X_j) represent the response of RBBR dye removal (%); and coded independent factors. β_0 is constant, whereas, β_i , β_{ii} , and β_{ij} signify the linear, quadratic, and interactive coefficients of input independent variables, respectively. A total of 46 runs were completed by BBD model to investigate the impacts of 5 independent factors on the removal of RBBR (%) as presented in (Tables: 2.2, 2.3 , 2.4).

Table 2.2: Experimental levels of independent factors and their codes in BBD (CS-G/ZnO/ Fe_3O_4)

Codes	Variables	Level 1 (-1)	Level 2 (0)	Level 3 (+1)
A	ZnO loading (%)	0	25	50
B	Adsorbent dose (g)	0.02	0.06	0.1
C	pH	4	7	10
D	Temperature (°C)	30	45	60
E	Time (min)	10	35	60

Table 2.3: Experimental levels of independent factors and their codes in BBD (CHT-GLA/ZnO/ Fe_3O_4)

Codes	Variables	Level 1 (-1)	Level 2 (0)	Level 3 (+1)
A	ZnO loading (%)	0	25	50
B	Adsorbent dose (g)	0.02	0.06	0.1
C	pH	4	7	10
D	Temperature (°C)	30	45	60
E	Time (min)	10	35	60

Table 2.4: Experimental levels of independent factors and their codes in BBD (Cs-Bz/ZnO/ Fe_3O_4)

Codes	Variables	Level 1 (-1)	Level 2 (0)	Level 3 (+1)
A	ZnO loading (%)	0	25	50
B	Adsorbent dose (g)	0.02	0.04	0.06
C	pH	4	7	10
D	Temperature (°C)	30	45	60
E	Time (min)	5	10	15

The experiments data of the optimization process as well as the RBBR removal as a response are recorded in (Tables: 2.5 , 2.6 , 2.7). A certain amount of the studied adsorbent was added to an Erlenmeyer flask (250 mL) containing 100 mL of RBBR solution (100 mg/L) before shaking process using a thermostat water bath shaker. The change in the RBBR concentrations was followed using HACH DR 3900 spectrophotometer at λ max 592. The RBBR decolorization (DR %) was determined by the following (equation 2.3) :

$$DR\% = \frac{C_0 - C_e}{C_0} \times 100 \quad (2.3)$$

Where C_0 : the initial concentration of the RBBR dye solution (mg/L), and C_e (mg/L) is the concentration of solution at equilibrium.

Table 2.5: The 5-variables BBD matrix and experimental data for RB19 decolorization (CS-G/ZnO/ Fe_3O_4)

Run	A: ZnO loading	B: Adsorbent dosage	C: pH	D: Temp	E: Time	RB19 decolorization (%)
1	0	0.02	7	45	35	7.7
2	50	0.02	7	45	35	53.8
3	0	0.1	7	45	35	70.1
4	50	0.1	7	45	35	87.3
5	25	0.06	4	30	35	68.9
6	25	0.06	10	30	35	47.2
7	25	0.06	4	60	35	93.8
8	25	0.06	10	60	35	21.2
9	25	0.02	7	45	10	39.4
10	25	0.1	7	45	10	71.2
11	25	0.02	7	45	60	51.2
12	25	0.1	7	45	60	87.7
13	0	0.06	4	45	35	79.3
14	50	0.06	4	45	35	82.9
15	0	0.06	10	45	35	4.2
16	50	0.06	10	45	35	58.9
17	25	0.06	7	30	10	50.7
18	25	0.06	7	60	10	80.3
19	25	0.06	7	30	60	65.8
20	25	0.06	7	60	60	92.2

Continued.....

21	25	0.02	4	45	35	66.3
22	25	0.1	4	45	35	89.3
23	25	0.02	10	45	35	8.5
24	25	0.1	10	45	35	61.3
25	0	0.06	7	30	35	38.1
26	50	0.06	7	30	35	62.1
27	0	0.06	7	60	35	75.5
28	50	0.06	7	60	35	84.1
29	25	0.06	4	45	10	80.2
30	25	0.06	10	45	10	33.9
31	25	0.06	4	45	60	85.2
32	25	0.06	10	45	60	45.8
33	0	0.06	7	45	10	41.3
34	50	0.06	7	45	10	62.4
35	0	0.06	7	45	60	60.8
36	50	0.06	7	45	60	76.8
37	25	0.02	7	30	35	36.2
38	25	0.1	7	30	35	67.6
39	25	0.02	7	60	35	52.8
40	25	0.1	7	60	35	88.1
41	25	0.06	7	45	35	67.5
42	25	0.06	7	45	35	62.8
43	25	0.06	7	45	35	71.2
44	25	0.06	7	45	35	70.4
45	25	0.06	7	45	35	72.2

Continued.....

<i>46</i>	<i>25</i>	<i>0.06</i>	<i>7</i>	<i>45</i>	<i>35</i>	<i>63.8</i>
-----------	-----------	-------------	----------	-----------	-----------	-------------

Table 2.6: The 5-variables BBD matrix and experimental data for RB19 decolorization (CHT-GLA/ZnO/ Fe_3O_4)

Run	A: ZnO loading	B: Adsorbent dosage	C: pH	D: Temp	E: Time	RB19 decolorization (%)
<i>1</i>	<i>0</i>	<i>0.02</i>	<i>7</i>	<i>45</i>	<i>35</i>	<i>10.2</i>
<i>2</i>	<i>50</i>	<i>0.02</i>	<i>7</i>	<i>45</i>	<i>35</i>	<i>42.6</i>
<i>3</i>	<i>0</i>	<i>0.1</i>	<i>7</i>	<i>45</i>	<i>35</i>	<i>41.6</i>
<i>4</i>	<i>50</i>	<i>0.1</i>	<i>7</i>	<i>45</i>	<i>35</i>	<i>50.3</i>
<i>5</i>	<i>25</i>	<i>0.06</i>	<i>4</i>	<i>30</i>	<i>35</i>	<i>65.1</i>
<i>6</i>	<i>25</i>	<i>0.06</i>	<i>10</i>	<i>30</i>	<i>35</i>	<i>29.1</i>
<i>7</i>	<i>25</i>	<i>0.06</i>	<i>4</i>	<i>60</i>	<i>35</i>	<i>75.8</i>
<i>8</i>	<i>25</i>	<i>0.06</i>	<i>10</i>	<i>60</i>	<i>35</i>	<i>39.4</i>
<i>9</i>	<i>25</i>	<i>0.02</i>	<i>7</i>	<i>45</i>	<i>10</i>	<i>32.2</i>
<i>10</i>	<i>25</i>	<i>0.1</i>	<i>7</i>	<i>45</i>	<i>10</i>	<i>44.9</i>
<i>11</i>	<i>25</i>	<i>0.02</i>	<i>7</i>	<i>45</i>	<i>60</i>	<i>22.7</i>
<i>12</i>	<i>25</i>	<i>0.1</i>	<i>7</i>	<i>45</i>	<i>60</i>	<i>62.9</i>
<i>13</i>	<i>0</i>	<i>0.06</i>	<i>4</i>	<i>45</i>	<i>35</i>	<i>42.3</i>
<i>14</i>	<i>50</i>	<i>0.06</i>	<i>4</i>	<i>45</i>	<i>35</i>	<i>57.2</i>
<i>15</i>	<i>0</i>	<i>0.06</i>	<i>10</i>	<i>45</i>	<i>35</i>	<i>18.9</i>
<i>16</i>	<i>50</i>	<i>0.06</i>	<i>10</i>	<i>45</i>	<i>35</i>	<i>43.2</i>
<i>17</i>	<i>25</i>	<i>0.06</i>	<i>7</i>	<i>30</i>	<i>10</i>	<i>40.3</i>

Continued.....

18	25	0.06	7	60	10	41.8
19	25	0.06	7	30	60	52.2
20	25	0.06	7	60	60	52.9
21	25	0.02	4	45	35	35.2
22	25	0.1	4	45	35	74.1
23	25	0.02	10	45	35	27.6
24	25	0.1	10	45	35	38.7
25	0	0.06	7	30	35	39.2
26	50	0.06	7	30	35	45.1
27	0	0.06	7	60	35	35.2
28	50	0.06	7	60	35	45.9
29	25	0.06	4	45	10	69.1
30	25	0.06	10	45	10	27.7
31	25	0.06	4	45	60	64.4
32	25	0.06	10	45	60	43.3
33	0	0.06	7	45	10	36.3
34	50	0.06	7	45	10	41.7
35	0	0.06	7	45	60	30.6
36	50	0.06	7	45	60	50.3
37	25	0.02	7	30	35	27.1
38	25	0.1	7	30	35	59.5
39	25	0.02	7	60	35	30.9
40	25	0.1	7	60	35	63.6
41	25	0.06	7	45	35	42.2
42	25	0.06	7	45	35	43.2

Continued.....

43	25	0.06	7	45	35	45.2
44	25	0.06	7	45	35	48.2
45	25	0.06	7	45	35	46.2
46	25	0.06	7	45	35	50.2

Table 2.7: The 5-variables BBD matrix and experimental data for RB19 decolorization (Cs-Bz/ZnO/ Fe_3O_4).

Run	A: ZnO loading	B: Adsorbent dosage	C: pH	D: Temp	E: Time	RB19 decolorization (%)
1	0	0.02	7	45	10	24.1
2	50	0.02	7	45	10	43.8
3	0	0.06	7	45	10	72.2
4	50	0.06	7	45	10	64.9
5	25	0.04	4	30	10	73.9
6	25	0.04	10	30	10	39.2
7	25	0.04	4	60	10	98.9
8	25	0.04	10	60	10	10.1
9	25	0.02	7	45	5	51.4
10	25	0.06	7	45	5	70.2
11	25	0.02	7	45	15	59.5
12	25	0.06	7	45	15	85.4
13	0	0.04	4	45	10	84.2
14	50	0.04	4	45	10	66.2
15	0	0.04	10	45	10	5.2

Continued.....

16	50	0.04	10	45	10	14.7
17	25	0.04	7	30	5	59.2
18	25	0.04	7	60	5	67.8
19	25	0.04	7	30	15	71.2
20	25	0.04	7	60	15	82.8
21	25	0.02	4	45	10	68.2
22	25	0.06	4	45	10	84.5
23	25	0.02	10	45	10	4.9
24	25	0.06	10	45	10	12.7
25	0	0.04	7	30	10	70.6
26	50	0.04	7	30	10	51.4
27	0	0.04	7	60	10	63.1
28	50	0.04	7	60	10	63.7
29	25	0.04	4	45	5	76.9
30	25	0.04	10	45	5	3.9
31	25	0.04	4	45	15	86.3
32	25	0.04	10	45	15	23.1
33	0	0.04	7	45	5	43.6
34	50	0.04	7	45	5	48.3
35	0	0.04	7	45	15	70.8
36	50	0.04	7	45	15	60.8
37	25	0.04	7	30	10	46.3
38	25	0.06	7	30	10	79.3
39	25	0.02	7	60	10	61.7
40	25	0.06	7	60	10	88.9

Continued.....

41	25	0.04	7	45	10	74.2
42	25	0.04	7	45	10	72.7
43	25	0.04	7	45	10	73.5
44	25	0.04	7	45	10	74.8
45	25	0.04	7	45	10	72.6
46	25	0.04	7	45	10	73.8

2.4.9 Batch adsorption study

From BBD, 46 experiments were carried out in order to find the best operation conditions that lead to the highest removal of RBBR for each biocomposite. The results of BBD are recorded in (Tables: 2.5, 2.6, 2.7), and the highest RBBR removal was run 7 . The quantity (mg) of adsorbate (RBBR) by samples (g) at equilibrium was calculated by the following (equation 2.4):

$$q_e = \frac{C_0 - C_e}{W} \times V \quad (2.4)$$

knowing that:

q_e is the adsorption capacity (mg/g)

V is the volume of the dye solution (L)

W(g) is the amount of the adsorbent..

CHAPTER 3

RESULTS AND DISCUSSION

This chapter aims to analyze and discuss the obtained results of chitosan-glyoxal/ZnO/ Fe_3O_4 , chitosan-glutaraldehyde/zinc oxide/ Fe_3O_4 , and chitosan-benzil/zinc oxide/ Fe_3O_4 . This chapter is divided into three sections, each of which contains

3.1 Results And Discussion Of Chitosan-Glyoxal/zinc oxide/ Fe_3O_4

($CS - G/ZnO/Fe_3O_4$)

3.1.1 Characterization of CS-G/ZnO/ Fe_3O_4

3.1.1.1 Morphological Characterization for the CS-G/ZnO/ Fe_3O_4

The morphological structure and chemical composition of $CS-G/Fe_3O_4$, $CS-G/ZnO/Fe_3O_4$ NPs-25, $CS-G/ZnO/Fe_3O_4$ NPs-50, and $CS-G/ZnO/Fe_3O_4$ NPs-25 after RB19 adsorption were investigated by SEM-EDX. (**Figure: 3.1,a-d**) display the obtained results of the SEM images and EDX analyses for $CS-G/Fe_3O_4$, $CS-G/ZnO/Fe_3O_4$ NPs-25, $CS-G/ZnO/Fe_3O_4$ NPs-50, and The surface morphology of $CS-G/Fe_3O_4$ after loading 25% ZnO (**Figure: 3.1,b**) and 50% ZnO (**Figure: 3.1,c**) into its polymeric matrix was converted to be rougher, more irregular with presence of various sizes of pores and cavities. These results indicate the uniform distribution of the ZnO nanoparticles into polymeric matrix of Fe_3O_4 . The EDX analysis corresponding to $CS-G/ZnO/Fe_3O_4$ NPs-25 and $CS-G/ZnO/Fe_3O_4$ NPs-50 reveal the presence of C, O, N, Fe and Zn. The presence of peak for Zn in the EDX spectrum indicates that the ZnO nanoparticles were successfully incorporated into the polymeric matrix of CS-G. The $CS-G/ZnO/Fe_3O_4$ NPs-25 surface after RB19 adsorption (**Figure: 3.1,d**) was significantly altered into a smoother one in line with the loading of RB19 dye molecules on its surface. This observation was reconfirmed by EDX analysis, which indicates the presence of S element related to the RB19 dye structure.

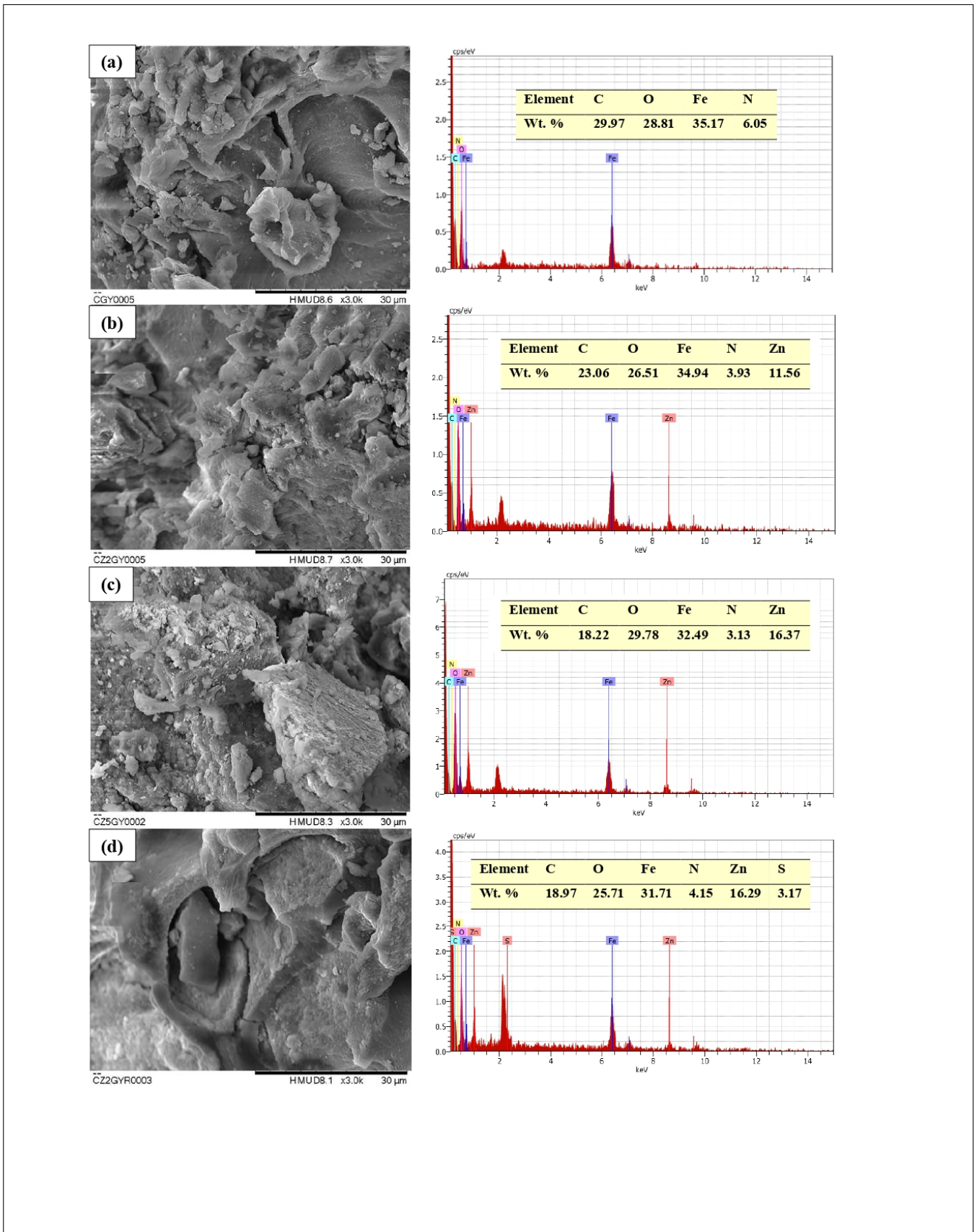


Figure 3.1: SEM-EDX analysis of (a) CS-G/ Fe_3O_4 , (b) CS-G/ZnO/ Fe_3O_4 NPs-25, (c) CS-G/ZnO/ Fe_3O_4 NPs-50, and (d) CS-G/ZnO/ Fe_3O_4 NPs-25 after adsorption of RB19 at magnification power 3000x.

3.1.1.2 FT-IR spectral analysis

The characteristic functional groups of the CS-G/ Fe_3O_4 , CS-G/ZnO/ Fe_3O_4 NPs-25, and CS-G/ZnO/ Fe_3O_4 NPs-25 after RB19 adsorption were identified by FTIR spectral analysis. (**Figure: 3.2**) presents the obtained spectra of the FTIR analysis for CS-G/ Fe_3O_4 , CS-G/ZnO/ Fe_3O_4 NPs-25, and CS-G/ZnO/ Fe_3O_4 NPs-25 after RB19 adsorption, respectively. The peaks presented (in blue color: CS-G/ Fe_3O_4) at $3400-3200\text{ cm}^{-1}$, 2900 cm^{-1} , 1650 cm^{-1} , 1340 cm^{-1} and 1070 cm^{-1} refer to $-NH_2$ and -OH groups stretching vibration, C-H stretching vibration, N-H bending of primary amine group, C-N stretching vibration and C-O stretching vibrations (C-O-C), respectively^[40]. The peak at 1650 cm^{-1} was also attributed to the C=N stretching vibration resulting from reaction between $-NH_2$ groups of CS and C=O groups of G^[88]. FTIR spectrum of CS-G/ZnO/ Fe_3O_4 NPs-25 (red color) shows the incremental increase of the intensity of the -OH and N-H bands, which can be attributed to the coordination bonds formed between OH and $-NH_2$ groups of CS and surface Zn^{2+} cations^[106]. Moreover, a new peak appeared at 530 cm^{-1} , due to Zn-O vibrations^[107]. FTIR spectrum of the CS-G/ZnO/ Fe_3O_4 NPs-25 after RB19 adsorption (green color) showed a notable change in intensity of the -OH and N-H bands, confirming the interaction of functional groups of the CS-G/ZnO/ Fe_3O_4 NPs-25 with RB19 molecules.

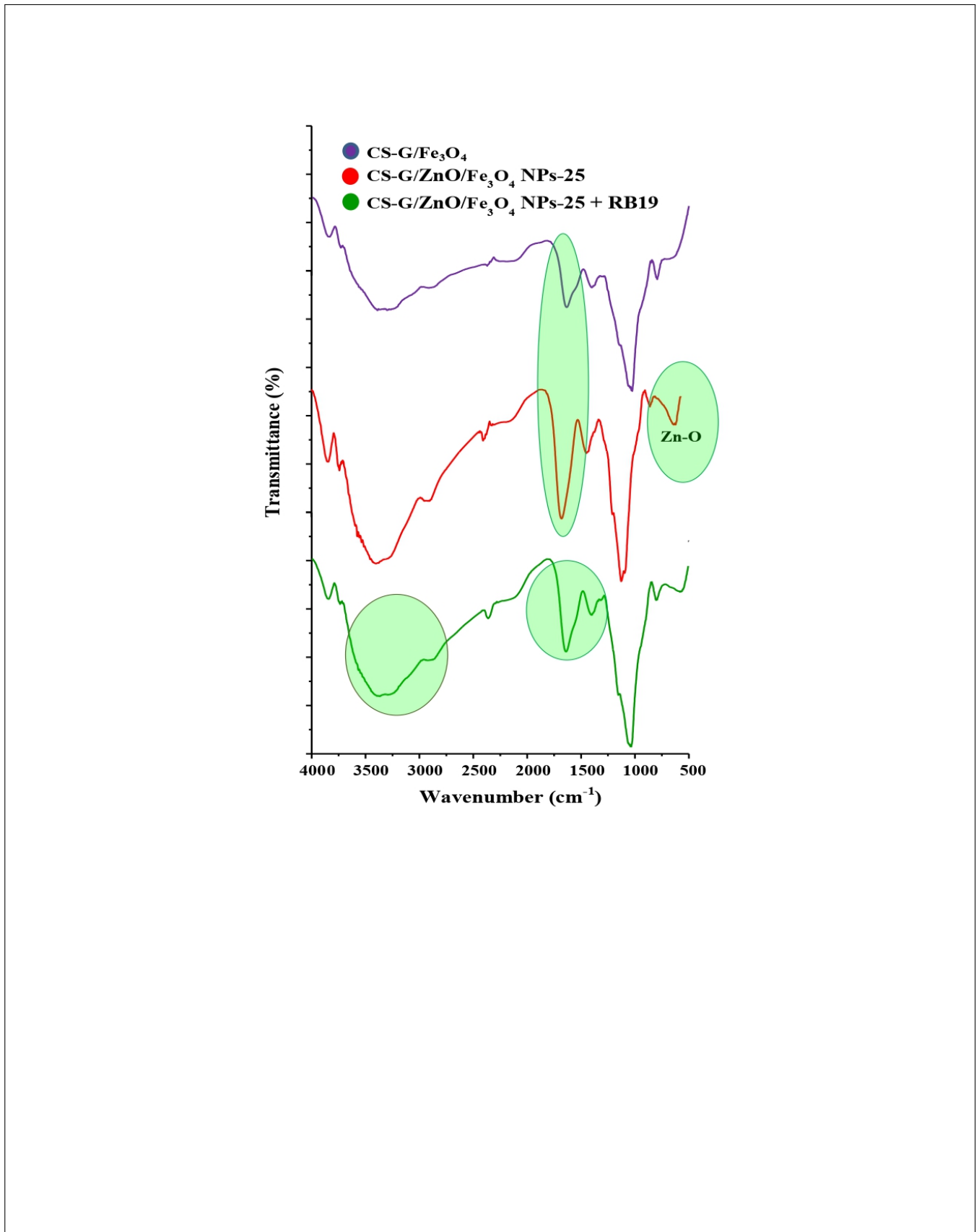


Figure 3.2: FTIR spectra of CS-G/ Fe_3O_4 , CS-G/ $\text{ZnO}/\text{Fe}_3\text{O}_4$ NPs-25 and CS-G/ $\text{ZnO}/\text{Fe}_3\text{O}_4$ NPs-25 after adsorption of RB19

3.1.1.3 Physio-chemical properties

The physicochemical properties (elemental composition, amine content, BET surface area, average pore diameter, and pore volume) of CS-G/ Fe_3O_4 , CS-G/ZnO/ Fe_3O_4 NPs-25, and CS-G/ZnO/ Fe_3O_4 NPs-50 are listed in (Table: 3.1). It can be distinctly seen from (Table: 3.1) that the C content was significantly decreased in CS-G/ZnO/ Fe_3O_4 NPs-25 and CS-G/ZnO/ Fe_3O_4 NPs-50 compared to CS-G/ Fe_3O_4 ; whereas, the oxygen content was higher in CS-G/ZnO/ Fe_3O_4 NPs-25 and CS-G/ZnO/ Fe_3O_4 NPs-50 compared to CS-G/ Fe_3O_4 . This drastic increment in oxygen content can be assigned to the loading of metal oxide (ZnO) nanoparticles into biopolymer matrix of the CS-G/ Fe_3O_4 . From (Table: 3.1), the actual amine ($-NH_2$) group content (%) for CS-G/ Fe_3O_4 , CS-G/ZnO/ Fe_3O_4 NPs-25, and CS-G/ZnO/ Fe_3O_4 NPs-50 are 23.5%, 18.4%, and 12.55%, respectively.

This gradual descend in the amine ($-NH_2$) group content (%) by loading more ZnO nanoparticles into polymeric matrix of the CS-G/ Fe_3O_4 can be attributed to two main possible reasons: (i) replacing the portion of CS in the polymeric matrix of CS-G/ Fe_3O_4 by adding ZnO nanoparticles will basically lead to reduce the content of amine ($-NH_2$) group in the final CS composite-based material^[108], (ii) strong interaction between the amine ($-NH_2$) group in CS backbone with zinc ions^[109]. The BET analysis shows that the surface area of CS-G/ Fe_3O_4 increased by 5.1 times after loading 25% ZnO NPs (CS-G/ZnO/ Fe_3O_4 NPs-25), and further increased by 7.4 times after loading 50% ZnO NPs (CS-G/ZnO/ Fe_3O_4 NPs-50). This finding can be assigned to the fact that the ZnO nanoparticles with high surface area were well scattered in the CS-G/ Fe_3O_4 matrix and caused an increase in its surface area^[110]. According to the classification of IUPAC, all the synthesized materials (CS-G/ Fe_3O_4 , CS-G/ZnO/ Fe_3O_4 NPs-25, and CS-G/ZnO/ Fe_3O_4 NPs-50) are mesoporous^[111].

Table 3.1: The physicochemical properties of the synthesized nanomaterials.

Analysis	CS-G/ Fe_3O_4	CS-G/ZnO/ Fe_3O_4 NPs-25	CS-G/ZnO/ Fe_3O_4 NPs-50
C(wt. %)	22.89	19.64	13.76
H(wt. %)	4.39	4.27	2.42
N(wt. %)	3.0	2.39	1.66
O(wt. %)	69.72	73.7	82.16
pH-potentiometric titration $-NH_2$ (%)	23.5	18.4	12.5
BET surface area (m^2/g)	1.437	7.375	10.706
Total pore volume (cm^3/g)	0.00552	0.01362	0.01789
Vm (cm^3/g)	0.00017	0.00080	0.00125
Mean pore diameter (nm)	14.19	7.3	6.2

As per to the adsorption study of RB19 on CS-G/ZnO/ Fe_3O_4 NPs-25 section, the best decolorization of RB19 was obtained with CS-G/ZnO/ Fe_3O_4 NPs-25. Indeed, CS-G/ZnO/ Fe_3O_4 NPs-25 has higher surface area and lower amine ($-NH_2$) group content compared to CS-G/ Fe_3O_4 . In contrast, CS-G/ZnO/ Fe_3O_4 NPs-25 has lower surface area and higher amino content compared to CS-G/ZnO/ Fe_3O_4 NPs-50. Consequently, the composite formula of CS-G/ZnO/ Fe_3O_4 NPs-25 exhibits a perfect and desirable balance between the surface area and the amine ($-NH_2$) group content. Thus, CS-G/ZnO/ Fe_3O_4 NPs-25 was adopted as the best formulation of the composite material (adsorbent) for the decolorization of RB19 with respect to CS-G/ Fe_3O_4 and CS-G/ZnO/ Fe_3O_4 NPs-50.

3.1.1.4 XRD analysis

The crystallinity of the CS-G/ Fe_3O_4 , CS-G/ZnO/ Fe_3O_4 NPs-25, and CS-G/ZnO/ Fe_3O_4 NPs-50 were tested by XRD analysis. ([Figure: 3.3](#)) the XRD patterns of CS-G/ Fe_3O_4 , CS-G/ZnO/ Fe_3O_4 NPs-25, and CS-G/ZnO/ Fe_3O_4 NPs-50. The XRD pattern of CS-G/ Fe_3O_4 shows a major peak at $2\theta = 30.1^\circ$, 35.2° , 43.1° , 53.2° , 57.3° , and 62.1° , which are

assigned to Fe_3O_4 particles^[112]. The XRD patterns of CS-G/ Fe_3O_4 NPs-25, and CS-G/ Fe_3O_4 NPs-50 show a slight increase in intensity compared with that of CS-G/ Fe_3O_4 due to the loading of ZnO nanoparticles into the polymeric structure of CS-G/ Fe_3O_4 . These peaks revealed the successful loading of ZnO nanoparticles in the molecular structure of CS-G/ Fe_3O_4 .

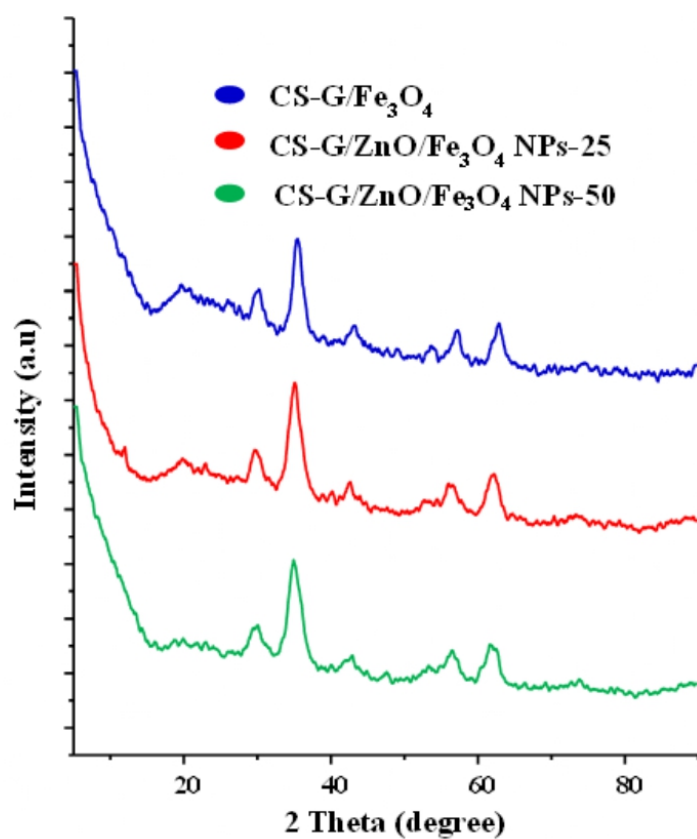


Figure 3.3: XRD patterns of CS-G/ Fe_3O_4 , CS-G/ZnO/ Fe_3O_4 NPs-25 and CS-G/ZnO/ Fe_3O_4 NPs-50.

3.1.2 BBD model analysis

The experimental data for the RB19 decolorization was investigated by the variance analysis (ANOVA) to comprehensively analyse the data and determine the significant parameters.

(Table: 3.2) shows ANOVA results of the RB19 decolorization. According to the results obtained, all the five key factors were found to be significant, and signifying that all of the five factors examined in the batch experiments affects the RB19 decolorization. As recorded in (Table: 3.2), F-value of BBD model is 22.42 (p-value < 0.0001) for RB19 decolorization that denotes the model is statistically significant^[101].

The validity and adequacy of the model can be concluded from the value of correlation coefficient (R^2) of 0.95^[113]. Moreover, this result also indicates good agreement between the predicted and observed values. The terms of BBD model with low probability values ($p < 0.05$) are statistically significant. From (Table: 3.2), A , B , C , D , E , AB , AC , BC , CD , A^2 , B^2 , and C^2

are also significant terms in the RB19 decolorization process. Hence, the empirical relationship between RB19 decolorization (%) and the tested variables was obtained by quadratic regression model as shown in (equation: 3.1):

$$\begin{aligned} \text{RB19 decolorization (\%)} = & +67.98 + 11.96A + 19.17B - 22.81C + 9.46D + 6.63E - 7.23AB \\ & + 12.77 AC + 7.45 BC - 12.72 CD - 5.84 A^2 - 6.41 B^2 - 7.38 C^2 \end{aligned} \quad (3.1)$$

Table 3.2: Analysis of variance (ANOVA) for RB19 decolorization.

Source	Sum of Squares	Df	Mean Square	F-value	p-value
Model	21504.37	20	1075.22	22.42	< 0.0001
A-ZnO loading	2287.23	1	2287.23	47.70	< 0.0001
B-Adsorbent dosage	5879.06	1	5879.06	122.61	< 0.0001
C-pH	8322.00	1	8322.00	173.56	< 0.0001
D-Temp.	1432.62	1	1432.62	29.88	< 0.0001
E-Time	703.58	1	703.58	14.67	0.0008
AB	208.80	1	208.80	4.35	0.0473
AC	652.80	1	652.80	13.61	0.0011
AD	59.29	1	59.29	1.24	0.2767
AE	6.50	1	6.50	0.1356	0.7158
BC	222.01	1	222.01	4.63	0.0413
BD	3.80	1	3.80	0.0793	0.7806
BE	5.52	1	5.52	0.1152	0.7372
CD	647.70	1	647.70	13.51	0.0011
CE	11.90	1	11.90	0.2482	0.6227
DE	2.56	1	2.56	0.0534	0.8191
A^2	298.03	1	298.03	6.22	0.0196
B^2	358.63	1	358.63	7.48	0.0113
C^2	474.95	1	474.95	9.91	0.0042
D^2	5.10	1	5.10	0.1064	0.7470
E^2	5.44	1	5.44	0.1135	0.7390
Residual	1198.75	25	47.95		
Cor Total	22703.12	45			

To further confirm the validity of model, several graphics derived from BBD such as normal probability of the residuals, observed values versus the predicted values, and residual versus run were statistically analyzed. The relationship between observed values and predicted values of RB19 decolorization is shown in ([Figure: 3.4,a](#)). From ([Figure: 3.4,a](#)) the observed values of RB19 decolorization (%) are in good agreement with the predicted values. This finding signifies the high applicability and accuracy of the BBD model^[114]. ([Figure: 3.4,b](#)) shows the normal plot of residuals of RB19 decolorization. According to ([Figure: 3.4,b](#)), the points lay on a relatively straight line, signifying the independence of the residuals, and accuracy of the assumptions^[108]. ([Figure: 3.4,c](#)) shows plot of residuals against run number. It can be seen from ([Figure: 3.4,c](#)) that the points are randomly distributed around zero, denoting the validity of the model^[115].

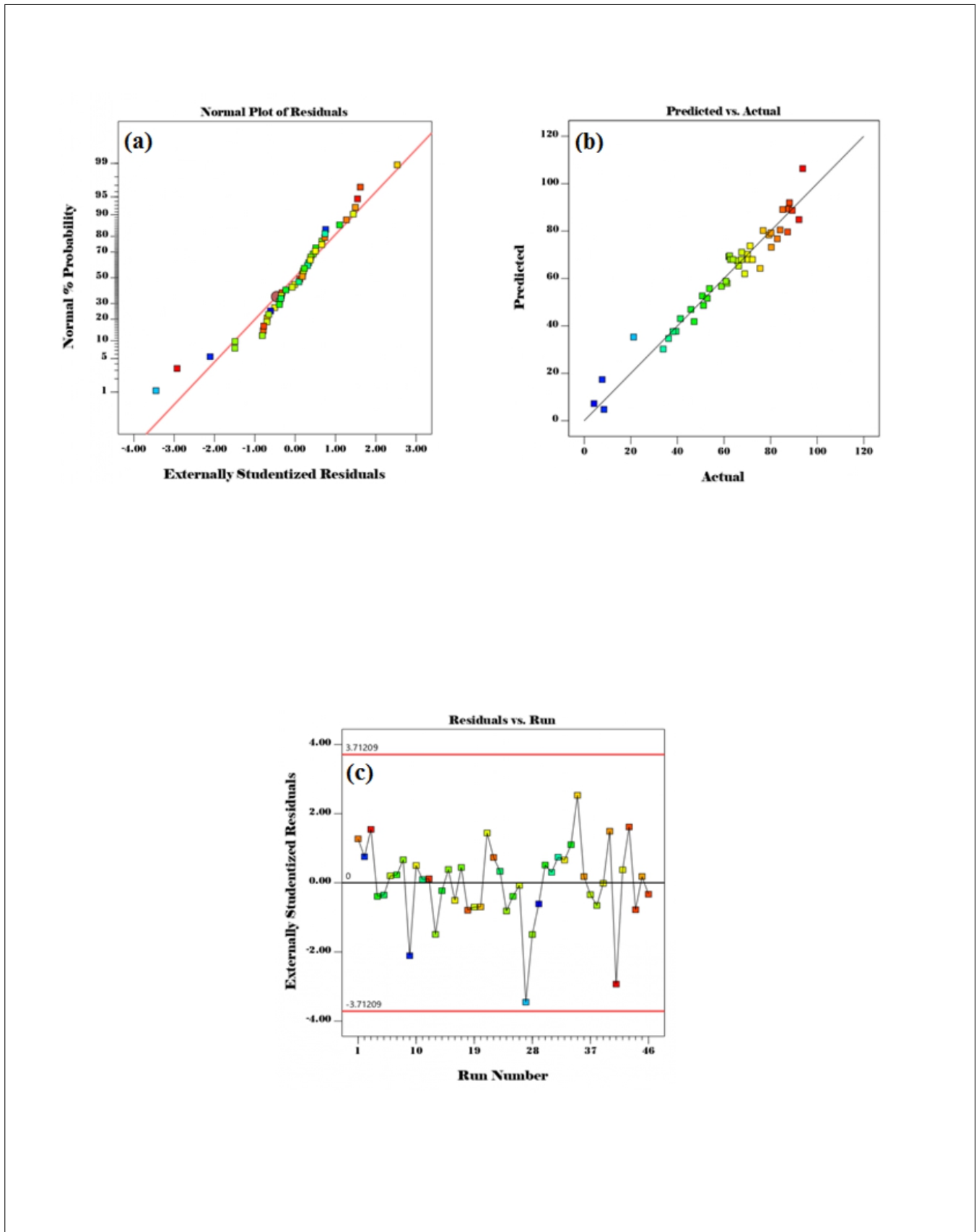


Figure 3.4: (a) Normal probability of the residuals, (b) observed values versus the predicted values, and (c) residual versus run

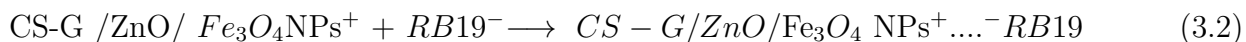
3.1.2.1 Parametric optimization of BBD

Three-dimensional (3D) response surfaces are employed to understand the interactive relationships between two selected parameters and the RB19 decolorization, in addition to determining the optimum operating conditions for the RB19 decolorization. The interaction between ZnO loading and adsorbent dosage on RB19 decolorization was significant.

([Figure: 3.5,a](#)) shows 3D surface plot of the interaction between ZnO loading and adsorbent dosage and their impact on RB19 decolorization, while other variables (pH =7, temperature = 45 °C, and time = 35 min) were kept constant. It was apparent from ([Figure: 3.5,a](#)) that the RB19 decolorization was improved by increasing both adsorbent dosage and ZnO loading. This result can be attributed to the fact that the ZnO nanoparticles have a high surface area, which leads to an increase in the surface area of the CS-G/ZnO/ Fe_3O_4 NPs^[110], in addition to the high number of active functional groups resulted from the higher dosage of adsorbent.

The interaction between ZnO nanoparticles loading and pH on RB19 decolorization was significant. ([Figure: 3.5,b](#)) shows 3D surface plot of the interaction between ZnO nanoparticles loading and pH and their impact on RB19 decolorization, while other variables (adsorbent dosage = 0.06 g, temperature = 45°C, and time = 35 min) were kept constant. It can be easily observed from ([Figure: 3.5,a](#)) that the RB19 decolorization was remarkably improved in acidic medium (pH = 4). This may be due to the positive charges generated from ZnO nanoparticles and thus, the adsorption of the negative groups of the RB19 dye^[116].

The interaction between adsorbent dosage and pH on RB19 decolorization was significant. ([Figure: 3.5,c](#)) shows 3D surface plot of the interaction between adsorbent dosage and pH and their impact on RB19 decolorization, while other variables (ZnO loading = 25%, temperature = 45°C, and time = 35 min) were kept constant. According to ([Figure: 3.5,c](#)), highest RB19 decolorization can be achieved at acidic solution pH (4). The pHPzc of the CS-G/ZnO/ Fe_3O_4 NPs was specified to be 6.4 as given in ([Figure: 3.5,d](#)). This result indicates that the CS-G/ZnO/ Fe_3O_4 NPs at pH > pHPzc acquires negative charges on its surface. As a result, the decrease in the pH value up to the acidic environment (pH = 4) leads to the generation of positive charges on the surface of CS-G/ZnO/ Fe_3O_4 NPs and consequently, formation of electrostatic attractions between the positive charges generated on the adsorbent surface and the negatively charged RB19 molecules as given in (equation: 3.2) .



The interaction between pH and temperature on RB19 decolorization was significant. ([Figure: 3.5,e](#)) shows 3D surface plot of the significant interaction between pH and temperature and their impact on RB19 decolorization, while other variables (ZnO loading = 25%, adsorbent dosage = 0.06 g, and time = 35 min) were kept constant. It can be shown in ([Figure: 3.5,e](#)) that RB19 decolorization was considerably enhanced with increasing the temperature up to 60°C, denoting that the adsorption process of RB19 was an endothermic in nature^[117].

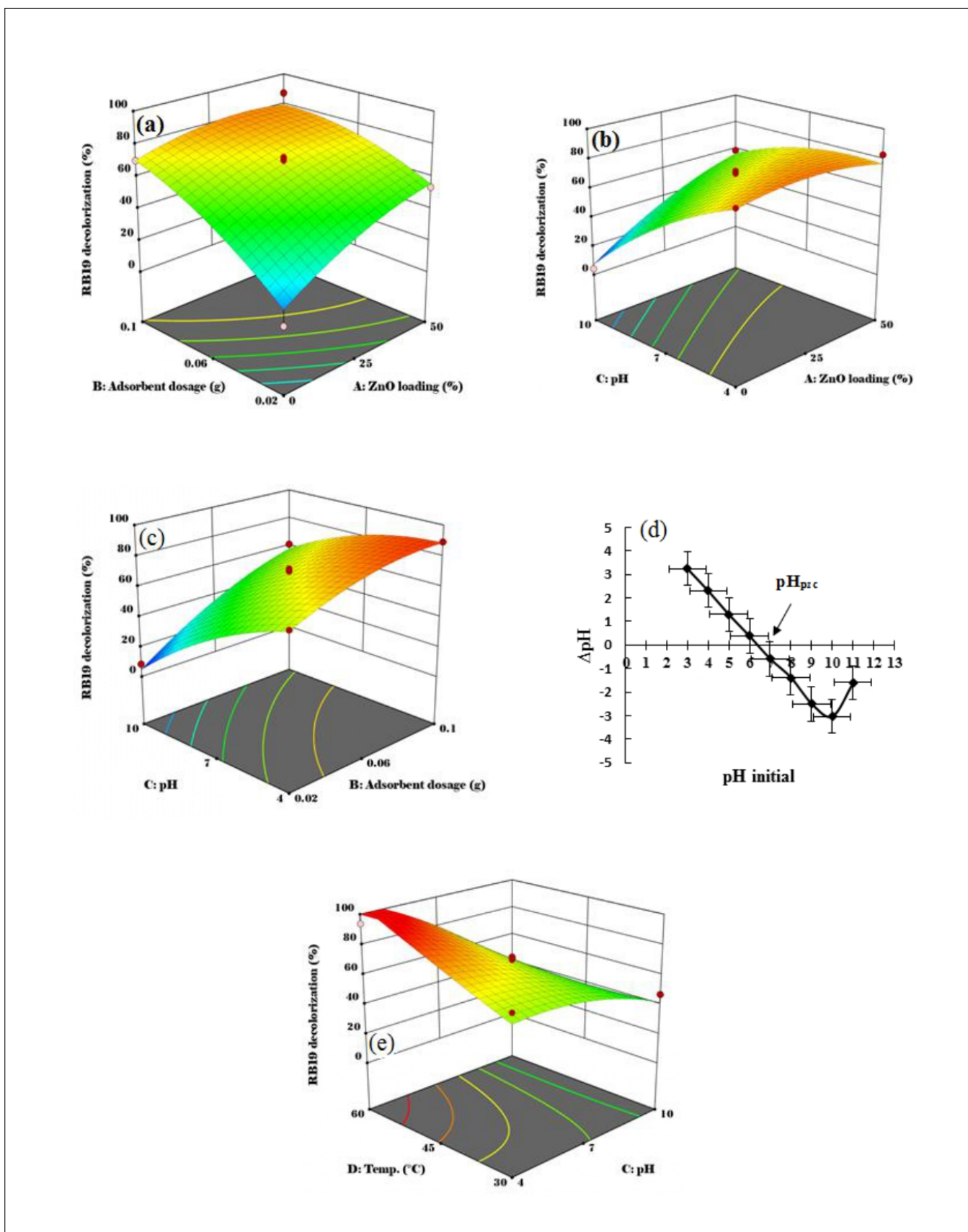


Figure 3.5: 3D response surfaces plots of (a) AB, (b) AC, (c) BC, and (e) CD interactions; whereas, (d) pH_{pzc} of CS-G/ZnO/Fe₃O₄ NPs

3.1.3 Adsorption study

The effect of initial RB19 concentration on adsorption efficiency by CS-G/ZnO/ Fe_3O_4 NPs-25 was assessed by varying RB19 concentrations between 50-300 mg/L, while other key parameters such as CS-G/ZnO/ Fe_3O_4 NPs-25 dose, pH, temperature, and shaking speed were kept constant at 0.06 g, 4, 60°C, and 100 rpm, respectively. (Figure: 3.6) depicts the adsorption capacity of CS-G/ZnO/ Fe_3O_4 NPs-25 to adsorb of RB19 as a function of contact time. As presented in (Figure: 3.6), a gradual increase in the adsorption capacity (59.7 to 334.9 mg/g) of CS-G/ZnO/ Fe_3O_4 NPs-25 was observed with an increase in initial RB19 concentration (from 50 to 300 mg/L). This finding can be attributed to the higher RB19 concentration, which acts as a driving force to mass transfer of the RB19 dye to active sites of the CS-G/ZnO/ Fe_3O_4 NPs-25^[40].

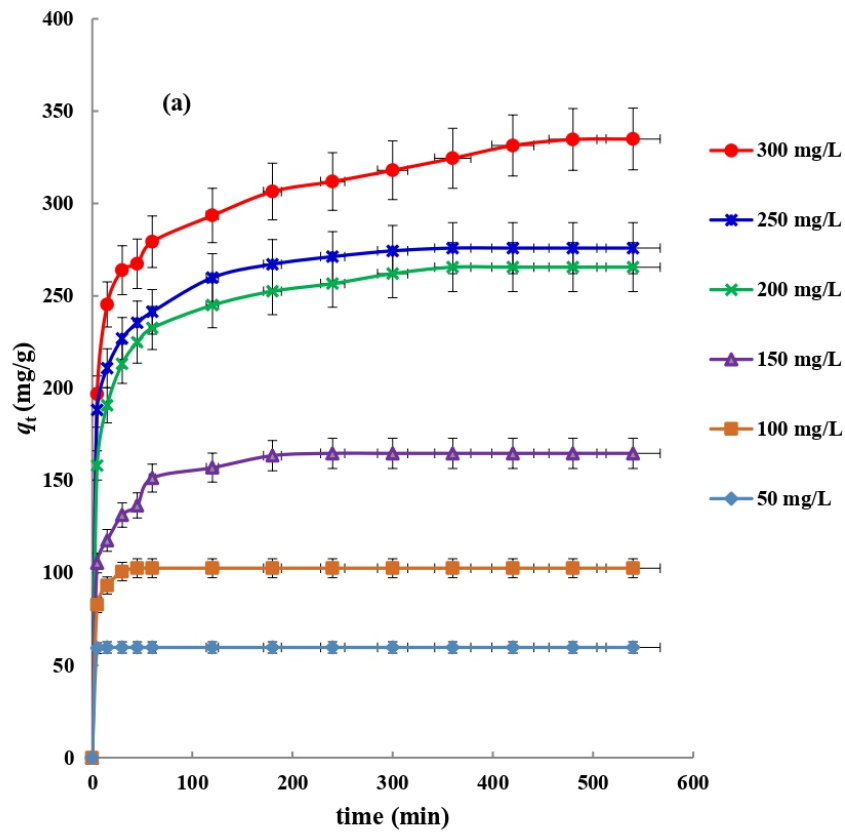


Figure 3.6: (a) Effect of the contact time on RB19 adsorption at different initial concentrations

3.1.4 Adsorption kinetics

Adsorption kinetic is a prime analysis for determining the rate of limiting mechanism and calculating the rate constant of RB19 adsorption from aqueous solution by CS-G/ZnO/ Fe_3O_4 NPs-25. The commonly applicable kinetic models involving pseudo-first-order (PFO) and pseudo-second-order (PSO) were used to analyze the adsorption data. (Equations 3.3 and 3.4) show the non-linear mathematical expressions of PFO^[118] and PSO^[119], respectively.

$$q_t = q_e(1 - \exp^{-K_1 t}) \quad (3.3)$$

$$q_t = \frac{q_e^2 K_2 t}{1 + q_e K_2 t} \quad (3.4)$$

where q_e (mg/g) and q_t (mg/g) are amounts of RB19 adsorbed onto the solid phase (CS-G/ZnO/ Fe_3O_4 NPs-25) at equilibrium and time (t), respectively. k_1 (1/min) and k_2 (g/mgmin) are rate constants for PFO and PSO, respectively. (Table: 3.3) shows the fitting parameters of the kinetic models. As recoded in (Table: 3.3), the PSO exhibits higher correlation coefficient (R^2) than PFO and also the calculated q_e of PSO agrees with experimental q_e very well. Thus, these results indicate that the chemisorption is the main controlling mechanism in the adsorption of RB19 onto CS-G/ZnO/ Fe_3O_4 NPs-25 surface^[120]. These results also signify that the adsorption of RB19 dye may be due to electrostatic attraction between the positively charged groups (e.g., $-NH_3^+$, $-OH_2^+$, and $Zn(OH)^+$ on the CS-G/ZnO/ Fe_3O_4 NPs-25 surface and negatively charged sulfonate (SO_3) groups of RB19 dye^[121].

Table 3.3: PFO and PSO kinetic parameters for RB19 adsorption by CS-G/ZnO/ Fe_3O_4 NPs-25

Concentration(mg/L)	$q_{eexp}(mg/g)$	PFO			PSO		
		$q_{ecal}(mg/g)$	$k_1(1/min)$	R^2	$q_{ecal}(mg/g)$	$k_2 * 10^{-2}(g/mgmin)$	R^2
50	59.7	59.7	0.999	1	59.8	51.57	1
100	102.6	101.8	0.325	0.99	103.5	0.764	0.99
150	164.7	155.9	0.168	0.90	163.1	0.150	0.97
200	265.5	248.9	0.150	0.92	260.2	0.087	0.98
250	275.8	259.2	0.225	0.93	269.4	0.123	0.97
300	334.9	304.5	0.168	0.91	328.7	0.076	0.97

3.1.5 Adsorption isotherm

Adsorption isotherm is an important function to explain how the CS-G/ZnO/ Fe_3O_4 NPs-25 can interact with the RB19 dye molecules. Therefore, different isotherm models^[122–124] were applied to study the adsorption behavior of RB19 by CS-G/ZnO/ Fe_3O_4 NPs-25, and computing the adsorption capacity of CS-G/ZnO/ Fe_3O_4 NPs-25. (Equations: 3.5, 3.6, and 3.7) show the non-linear mathematical expressions of Langmuir, Freundlich, and Temkin, respectively.

$$q_t = \frac{q_{max}K_aC_e}{1 + K_aC_e} \quad (3.5)$$

$$q_e = K_f C_e^{1/n} \quad (3.6)$$

$$q_t = \frac{RT}{b_T} \ln K_a C_e \quad (3.7)$$

where $q_{max}(mg/g)$ is the maximum adsorption capacity of CS-G/ZnO/ Fe_3O_4 NPs-25, and $K_a(L/mg)$ is a constant of Langmuir model. $K_f(mg/g)(L/mg)^{1/n}$ and n are the Freundlich constants. $K_T(L/mg)$ is equilibrium binding constant of Temkin model, $b_T(J/mol)$ is constant related to adsorption heat, $T(K)$ is the temperature, and $R(8.314J/molK)$ is the universal gas constant. The calculated parameters and plots of isotherm models are presented in (Table 3.4) and (**Figure: 3.7**), respectively. Depending on the coefficient of correlation (R^2), the equilibrium data are best fitted to the Freundlich model, which is supported by the higher (R^2)(0.95) compared to the Langmuir and Temkin models. This finding indicates the multilayer adsorption

of RB19 molecules onto heterogeneous surface of CS-G/ZnO/ Fe_3O_4 NPs-25^[125]. These results also reflect the hetro-energetic non-ideal reversible multi-layer adsorption nature of RB19 dye on CS-G/ZnO/ Fe_3O_4 NPs-25 and the RB19 molecules ability to form π - π interaction^[126] Furthermore, the q_{max} calculated from the Langmuir isotherm of RB19 onto CS-G/ZnO/ Fe_3O_4 NPs-25 was found to be 363.3 mg/g (**Table: 3.5**) compares the q_{max} of this study with adsorption capacities of different adsorbents reported in the literature for the adsorption of RB19. As recorded in (**Table: 3.5**), the q_{max} of the CS-G/ZnO/ Fe_3O_4 NPs-25 is superior over most of the previously reported adsorbents in the literature. Moreover, the obtained results indicate that the CS-G/ZnO/ Fe_3O_4 NPs-25 is a low-cost, feasible and promising adsorbent for environmental remediation process of textile wastewater.

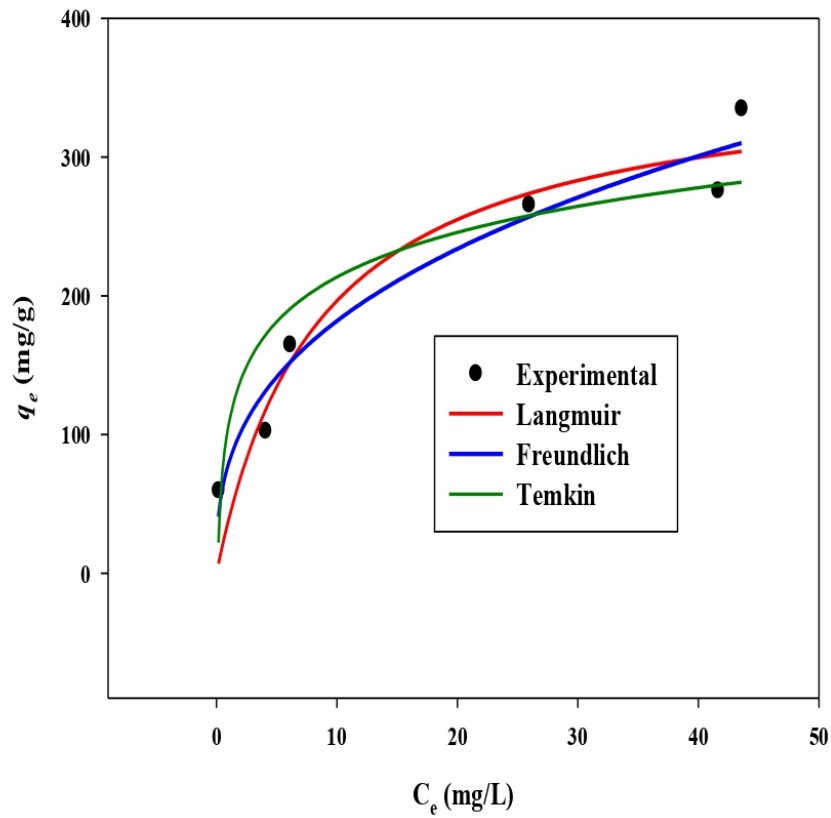


Figure 3.7: adsorption isotherms of RB19 by CS-G/ZnO/Fe₃O₄ NPs-25 (dosage = 0.06g, pH of solution = 4, temperature = 60°C, agitation speed = 100 strokes and volume of solution = 100 mL)

Table 3.4: Parameters of the Langmuir, Freundlich and Temkin isotherm models for RB19 adsorption on CS-G/ZnO/ Fe_3O_4 NPs-25 at 60°C

Adsorption isotherm	Parameter	Value
Langmuir	qm (mg/g)	363.3
	Ka (L/mg)	0.117
	R^2	0.92
Freundlich	Kf (mg/g) (L/mg) ^{1/n}	78.9
	N	2.7
	R^2	0.95
Temkin	KT (L/mg)	2.3
	bT (J/mol)	59.6
	R^2	0.83

Table 3.5: Comparison of the adsorption capacity of RB19 dye by various

Adsorbents	qm (mg/g)	References
Chitosan-glyoxal/ZnO/ Fe_3O_4 nanoparticles	363.3	This study
Chitosan-epichlorohydrin/kaolin clay composite	560.9	[40]
Chitosan/MgO composite	512.82	[127]
Polyaniline/chitosan composite	303.03	[128]
Carboxylated carbon nanotube	291.55	[129]
ZnO-polyacrylonitrile-hinokitiol	267.37	[130]
Bentonite-DTMA	206.58	[131]
Fe_3O_4 @L-arginine	125	[132]
Chitosan-alkali lignin composite	111.11	[133]
Chitosan/SiO ₂ /carbon nanotubes magnetic nanocomposite	97.08	[134]
Amino-functionalized organosilane	21.3	[135]
Borax cross-linked Jhingan gum hydrogel	9.884	[136]

3.1.6 Adsorption mechanism

The adsorption mechanism of RB19 dye was established on the basis of the availability of active binding sites including amino $-NH_2$, hydroxyl $-OH$, and $Zn(OH)^+$ on the CS-G/ZnO/ Fe_3O_4 NPs surface as shown in ([Figure: 3.8](#)). Initially, the CS-G/ZnO/ Fe_3O_4 NPs surface can acquire positive charges in an acidic medium because the pH value in the acid medium is less than pHPzc value (as shown in ([Figure: 3.5,d](#)). The positive charges for CS-G/ZnO/ Fe_3O_4 NPs surface can come from several locations such as the protonated groups of amino $-NH_2$, and hydroxyl $-OH$, in addition to positive charges generated from ZnO NPs. Electrostatic interactions are the major contributor to the RB19 adsorption process due to the abundance of cationic groups and positive charges available on the CS-G/ZnO/ Fe_3O_4 NPs surface, which are attracted to the sulfonate groups ($-SO_3^-$) of the RB19 dye, as shown in ([Figure: 3.8,a](#)). Several researches have reported that the adsorption of organic dyes by ZnO NPs in acidic medium is through electrostatic attractions between the positively charged ZnO-NPs and the anionic dyes molecules Hydrogen interactions represented by H-bonding and Yoshida H-bonding also play a fundamental role in RB19 dye adsorption. These interactions (H-bonding, see ([Figure: 3.8,b](#)) and Yoshida H-bonding, see ([Figure: 3.8,c](#)) are generated from the interaction of free hydrogen and H-OH (hydrogen of hydroxyl) with the groups containing N and O and the aromatic rings of the RB19 dye, respectively^[137]. Finally, n- interactions ([Figure: 3.8,d](#)) are among the most common paths to improve the absorption process of organic dyes by CS composites. These interactions can come from the interaction of the electron pairs of N and O (electron donor) in the CS-G/ZnO/ Fe_3O_4 NPs with the aromatic system (electron acceptor) of the RB19 dye^[12].

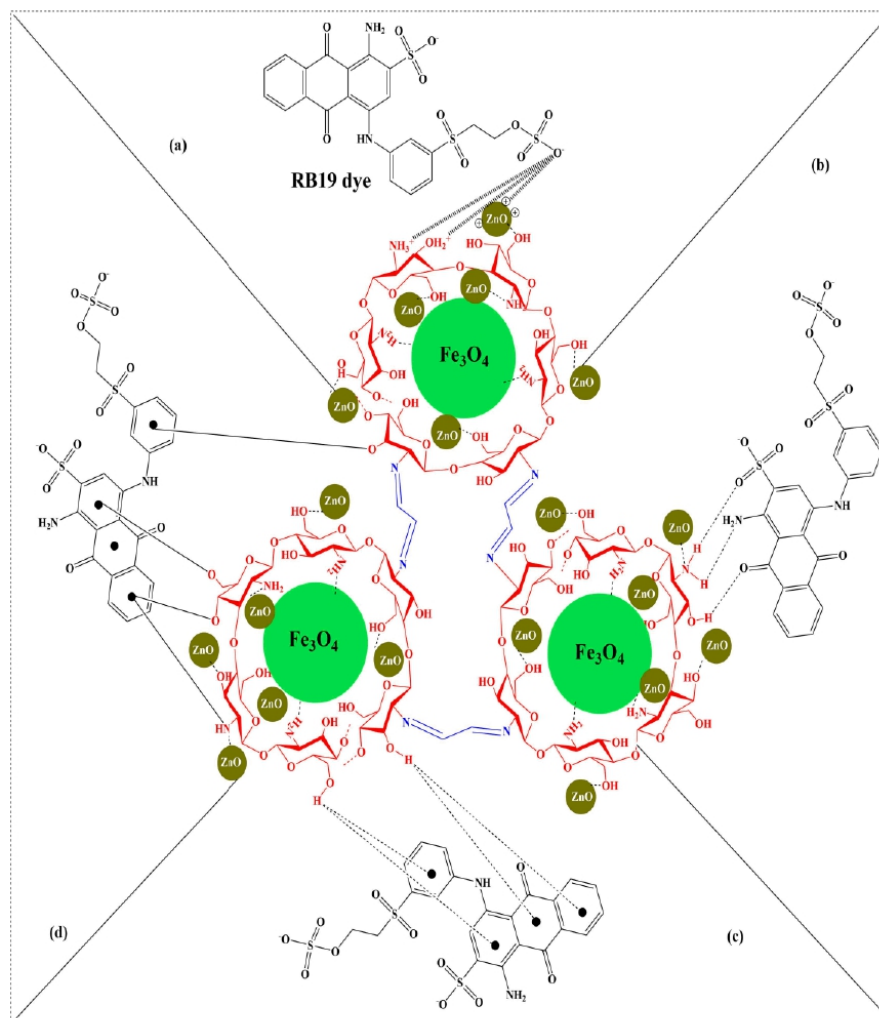


Figure 3.8: Illustration of the possible interaction between CS-G/ZnO/ Fe_3O_4 NPs surface and RB19 including (a) electrostatic attraction, (b) hydrogen bonding interactions, (c) Yoshida H-bonding, and (d) n- interactions.

3.2 Results And Discussion Of Chitosan-glutaraldehyde/zinc oxide/ Fe_3O_4

(*CHT – GLA/ZnO/Fe₃O₄*)

3.2.1 Characterization of CHT-GLA/ZnO/ Fe_3O_4

3.2.1.1 Morphological Characterization for the CHT-GLA/ZnO/ Fe_3O_4

The surface morphology and chemical composition of CHT-GLA/ Fe_3O_4 , CHT-GLA/ZnO/ Fe_3O_4 -25, CHT-GLA/ZnO/ Fe_3O_4 -50, and CHT-GLA/ZnO/ Fe_3O_4 -25 after RBBR adsorption were examined by SEM-EDX. The SEM images and EDX analysis of CHT-GLA/ Fe_3O_4 , CHT-GLA/ZnO/ Fe_3O_4 -25, CHT-GLA/ZnO/ Fe_3O_4 -50, and CHT-GLA/ZnO/ Fe_3O_4 -25 after RBBR adsorption are presented respectively in ([Figure: 3.9,a-d](#)). As depicted in ([Figure: 3.9,a](#)), the CHT-GLA/ Fe_3O_4 nanocomposite owned an irregular, wavy, and uneven structure. The EDX analysis of CHT-GLA/ Fe_3O_4 composite detects the presence of C, O, N and Fe. ([Figure: 3.9,b](#)) and ([Figure: 3.9,c](#)) corresponding to 25% ZnO and 50% ZnO nanoparticles loaded into molecular structure of CHT-GLA show that the nanocomposites surface contains small fractures and holes due to the embedded and well-dispersed ZnO nanoparticles into polymer matrix of CHT-GLA. According to EDX analysis, the main elements present in CHT-GLA/ZnO/ Fe_3O_4 -25 and CHT-GLA/ZnO/ Fe_3O_4 -50 nanocomposites are C, N, O, Fe and Zn. The presence of peak for Zn element in the EDX spectrum confirms that the ZnO nanoparticles were successfully loaded into the structure of CHT-GLA. After RBBR adsorption, CHT-GLA/ZnO/ Fe_3O_4 nanocomposite surface was remarkably changed into smooth, compact and homogenous surface in agreement with the covering by RBBR molecule. This finding was confirmed by EDX, which indicated the existence S element.

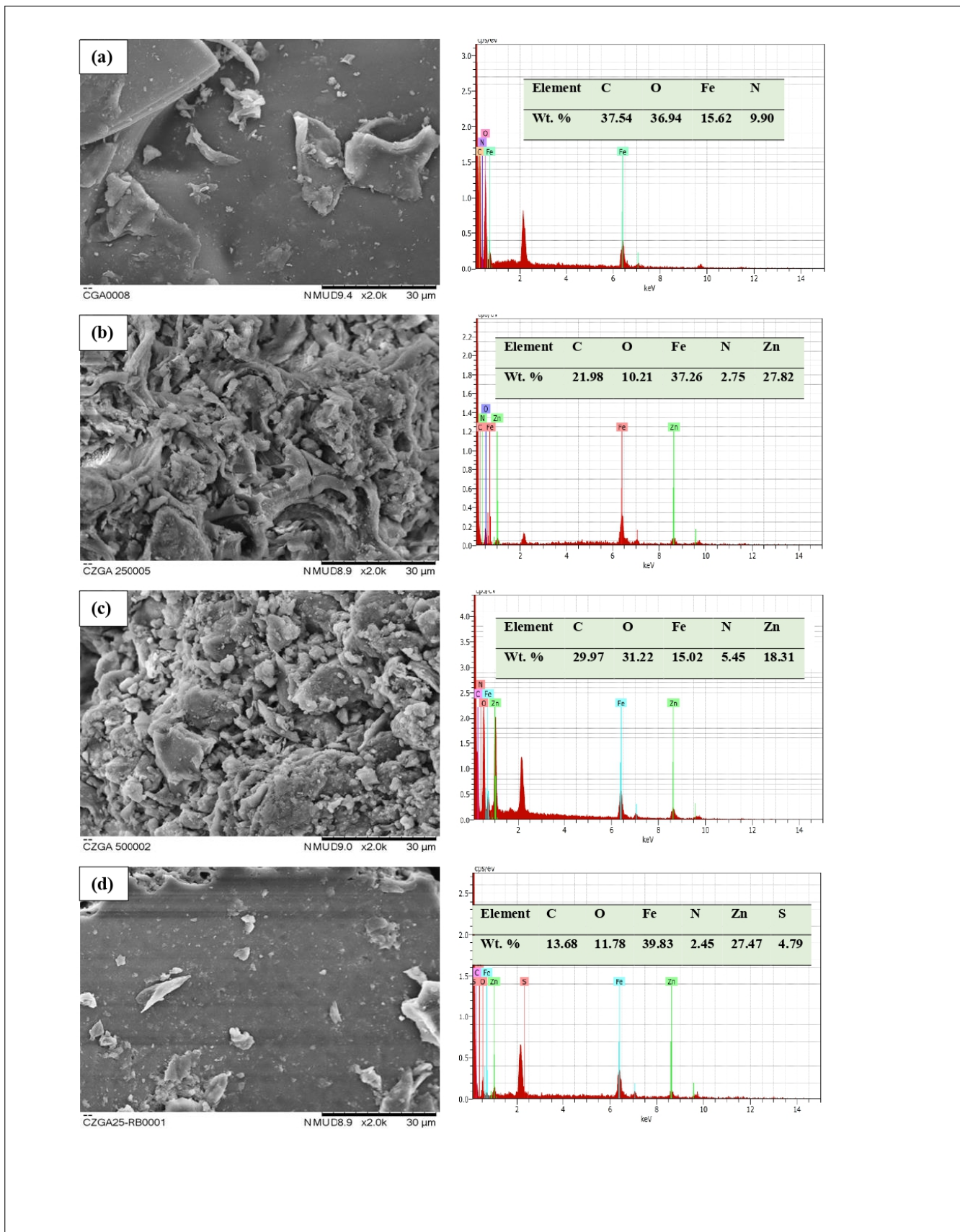


Figure 3.9: SEM images of (a) CHT-GLA/ Fe_3O_4 , (b) CHT-GLA/ZnO/ Fe_3O_4 -25, (c) CHT-GLA/ZnO/ Fe_3O_4 -50, and (d) CHT-GLA/ZnO/ Fe_3O_4 -25 after adsorption of RBBR dye at magnification power 2000x.

3.2.1.2 FT-IR spectral analysis

The typical functional groups of the CHT-GLA/ Fe_3O_4 , CHT-GLA/ZnO/ Fe_3O_4 -25, and CHT-GLA/ZnO/ Fe_3O_4 -25 after RBBR adsorption were obtained by FTIR analysis. The FTIR spectra of CHT-GLA/ Fe_3O_4 , CHT-GLA/ZnO/ Fe_3O_4 , and CHT-GLA/ZnO/ Fe_3O_4 -25 after RBBR adsorption are presented respectively in ([Figure: 3.10, a-c](#)). The bands observed ([Figure: 3.10, a](#)) at 3430 cm^{-1} , 2910 cm^{-1} , 1640 cm^{-1} , 1370 cm^{-1} , 1060 cm^{-1} , and 550 cm^{-1} are ascribed to O-H and N-H stretching, C-H symmetric stretching, N-H bending vibration, C-N stretching of residual N-acetyl group, C-O-C stretching vibration, and Fe-O bond, respectively^[101]. The peak at 1660 cm^{-1} also corresponding to the C=N stretching vibration arising from Schiff base reaction between amino groups of CHT and carbonyl groups of GLA^[138]. In FTIR spectrum of CHT-GLA/ZnO/ Fe_3O_4 -25, it was clearly observed the bands of $-NH_2$ and OH groups were shifted and became stronger, signifying the strong interaction between $-NH_2$ and OH groups and ZnO^[106]. In same context, the peak observed at 540 cm^{-1} corresponding to metal oxygen linkage (Zn-O)^[107]. The spectrum of the CHT-GLA/ZnO/ Fe_3O_4 nanocomposite after RBBR adsorption appeared a remarkable shift in the -OH and N-H bands, signifying the contributing of the -OH and $-NH_2$ groups in the RBBR adsorption.

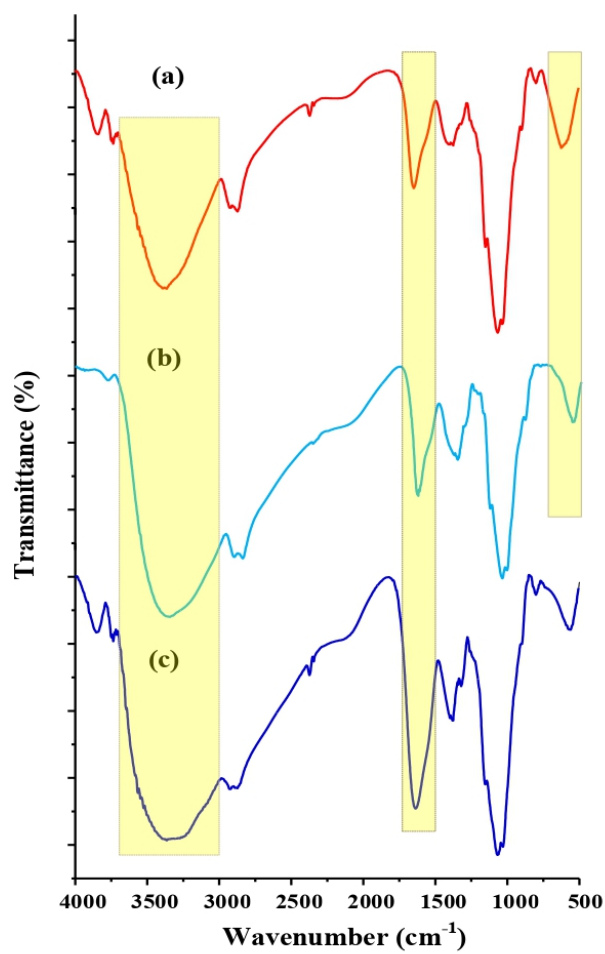


Figure 3.10: FTIR spectra of (a) CHT-GLA/ Fe_3O_4 , (b) CHT-GLA/ZnO/ Fe_3O_4 -25, and (c) CHT-GLA/ZnO/ Fe_3O_4 -25 after adsorption of RBBR dye

3.2.1.3 Physio-chemical properties

The physicochemical characteristics, namely, elemental composition, amine group content, surface areas properties of the CHT-GLA/ Fe_3O_4 , CHT-GLA/ZnO/ Fe_3O_4 -25, CHT-GLA/ZnO/ Fe_3O_4 -50 are presented in (Table: 3.6). CHN-O analysis of the elemental composition demonstrated that the CHT-GLA/ZnO/ Fe_3O_4 -25 and CHT-GLA/ZnO/ Fe_3O_4 -50 had lower carbon content, and higher oxygen content than CHT-GLA/ Fe_3O_4 . This finding can be attributed to the incorporation of metal oxide (ZnO) nanoparticles into the molecular structure of CHT-GLA. The results of the pH-potentiometric titration clarified that the amine group content (%) in CHT-GLA/ZnO/ Fe_3O_4 -25 and CHT-GLA/ZnO/ Fe_3O_4 -50 was gradually decreased with additional loading of ZnO nanoparticles in the molecular structure of CHT-GLA. This observation can be assigned to the physical mixing of CHT with ZnO nanoparticles. In another word, more loading of ZnO nanoparticles will lead to less content of CHT in the whole molecular structure of the composite material as a result less amine group content will be obtained^[138]. Another possible reason is the coordination of zinc ions with the amino and hydroxyl groups, which may lead to reduce the free amino group content^[109].

The results of BET analysis showed that the surface area of CHT-GLA/ Fe_3O_4 , CHT-GLA/ZnO/ Fe_3O_4 -25, and CHT-GLA/ZnO/ Fe_3O_4 -50 are 4.17, 9.92, and 6.67, respectively. These results are probably due to the fact that the ZnO nanoparticles possessing a high surface area were scattered on the CHT-GLA/ Fe_3O_4 matrix and enlarged its surface^[110]. It was clearly observed from (Table: 3.6) that the CHT-GLA/ZnO/ Fe_3O_4 -25 has a higher surface area compared to CHT-GLA/ZnO/ Fe_3O_4 -50, although CHT-GLA/ZnO/ Fe_3O_4 -50 has a higher loading of ZnO nanoparticles. These results can be attributed to the fact that a high loading of ZnO nanoparticles may cause depositing of some of them within the larger pores of the CHT-GLA matrix^[139]. Depending on the classification of IUPAC, all the prepared composites (CHT-GLA/ Fe_3O_4 , CHT-GLA/ZnO/ Fe_3O_4 -25, and CHT-GLA/ZnO/ Fe_3O_4 -50) are a mesoporous^[111].

Table 3.6: The physicochemical properties of the synthesized nanocomposites.

Analysis	CHT-GLA/ Fe_3O_4	CHT-GLA/ZnO/ Fe_3O_4 -25	CHT-GLA/ZnO/ Fe_3O_4 -50
C(wt. %)	33.95	26.34	17.92
H(wt. %)	6.37	4.97	3.15
N(wt. %)	4.19	2.93	1.49
O(wt. %)	55.49	62.76	77.44
pH-potentiometric titration $-NH_2$ (%)	26.5	19.3	16.1
BET surface area (m^2/g)	4.17	9.92	6.67
Total pore volume (cm^3/g)	0.0129	0.0180	0.0170
Vm (cm^3/g)	0.00033	0.00069	0.00037
Mean pore diameter (nm)	12.3	7.2	10.2

3.2.1.4 XRD analysis

The crystallinity of the CHT-GLA/ Fe_3O_4 , CHT-GLA/ZnO/ Fe_3O_4 -25, and CHT-GLA/ZnO/ Fe_3O_4 -50 were investigated by XRD analysis. The XRD patterns of CHT-GLA/ Fe_3O_4 , CHT-GLA/ZnO/ Fe_3O_4 -25, and CHT-GLA/ZnO/ Fe_3O_4 -50 are exhibited respectively in (Figure: 3.11, a-c). The XRD result of CHT-GLA/ Fe_3O_4 (Figure: 3.11,a) exhibits several crystalline peaks at $2\theta = 30.1^\circ$, 35.2° , 43.1° , 53.2° , 57.3° , and 62.1° , which are assigned to (220), (311), (400), (422), (511), and (440) of Fe_3O_4 particles, respectively^[112]. The broad peak observed at 20.3° in (Figure: 3.11, a) is ascribed to the semicrystalline nature of CHT^[106]. The XRD patterns of CHT-GLA/ZnO/ Fe_3O_4 -25 (Figure: 3.11, a) and CHT-GLA/ZnO/ Fe_3O_4 -50 (Figure: 3.11,b) shows a typical crystalline peak at 31.80, 34.45, 36.27, 47.59, 56.66, 62.91, and 68.0 belonging to the crystalline phases (100), (002), (101), (102), (110), (103), and (112), respectively of ZnO nanoparticles^[106]. These results confirm the strong interaction between the $-NH_2$ and $-OH$ groups of CHT with Zn ions and reinforce a good compatibility between the polymer matrix of CHT-GLA and the ZnO^[140]. Furthermore, it was noticed that all the peaks of CHT-GLA/ZnO/ Fe_3O_4 -50 had a higher intensity compared to CHT-GLA/ZnO/ Fe_3O_4 -25 due to the increased loading of ZnO nanoparticles in the polymer matrix of CHT-GLA.

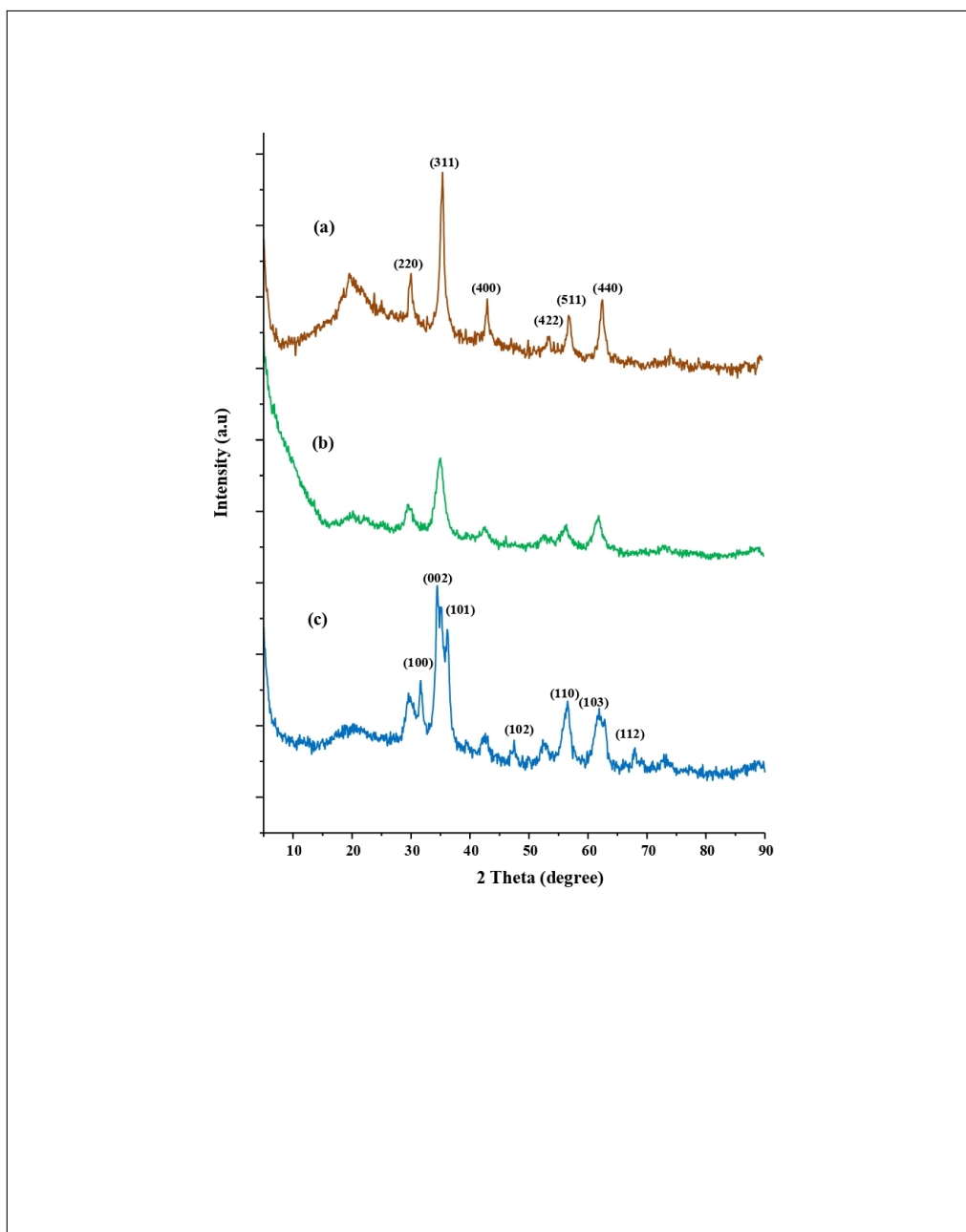


Figure 3.11: XRD patterns of (a) CHT-GLA/ Fe_3O_4 , (b) CHT-GLA/ZnO/ Fe_3O_4 -25, and (c) CHT-GLA/ZnO/ Fe_3O_4 -50

3.2.2 BBD model analysis

The statistical analysis and specification the important impacts of the parameters and their interactions for the RBBR removal data was achieved by the variance analysis (ANOVA).

(Table: 3.7) displays ANOVA results of the RBBR removal. The model F value of 16.37 (p-value < 0.0001) indicates that the model for the RBBR removal is significant^[40]. The value of correlation coefficient (R^2) for this model is 0.93, which indicates that the accuracy of the fitting of the model, and good correlation between predicted and experimental RBBR removal

values^[137]. Statistically, the model terms are significant with P-value less than 0.05. In this case A, B, C, E, AB, BC, BE, A^2 , and B^2 are significant terms in the RBBR removal process. Thus, the experimental relationship between RBBR removal efficiency and the examined variables was correlated by quadratic polynomial model as expressed in (Equation: 3.8).

$$\begin{aligned} \text{RBBR Removal efficiency (\%)} = & +45.87 + 7.63A + 12.94B - 13.46C + 2.83E - 5.93AB - 6.95BC \\ & + 6.88 BE - 6.86 A^2 - 4.07 B^2 \end{aligned} \quad (3.8)$$

Table 3.7: Analysis of variance (ANOVA) for RBBR removal.

Source	Sum of Squares	Df	Mean Square	F-value	p-value
Model	8308.45	20	415.42	16.37	< 0.0001
A-ZnO loading	930.25	1	930.25	36.65	< 0.0001
B-Adsorbent dosage	2680.65	1	2680.65	105.63	< 0.0001
C-pH	2897.13	1	2897.13	114.16	< 0.0001
D-Temp.	48.65	1	48.65	1.92	0.1784
E-Time	128.26	1	128.26	5.05	0.0336
AB	140.42	1	140.42	5.53	0.0268
AC	22.09	1	22.09	0.8704	0.3598
AD	5.76	1	5.76	0.2270	0.6379
AE	51.12	1	51.12	2.01	0.1682
BC	193.21	1	193.21	7.61	0.0107
BD	0.0225	1	0.0225	0.0009	0.9765
BE	189.06	1	189.06	7.45	0.0115
CD	0.0400	1	0.0400	0.0016	0.9686
CE	103.02	1	103.02	4.06	0.0548
DE	0.1600	1	0.1600	0.0063	0.9373
A^2	411.25	1	411.25	16.20	0.0005
B^2	144.77	1	144.77	5.70	0.0248
C^2	88.09	1	88.09	3.47	0.0742
D^2	55.00	1	55.00	2.17	0.1535
E^2	0.0064	1	0.0064	0.0003	0.9875
Residual	634.47	25	25.38		
Cor Total	8942.91	45			

Moreover, the verification of experimental results can be achieved by the analysis of the obtained graphics from BBD model such as actual versus predicted, normal probability of the residuals, and externally studentized residuals versus predicted. ([Figure: 3.12, a](#)). displays the actual versus predicted plot of RBBR removal efficiency values. According to ([Figure: 3.12, a](#)), the points of actual were mostly close to the points of predicted, signifying that the BBD model

can adequately optimize the adsorption process of RBBR dye. ([Figure: 3.12, b](#)) demonstrates the normal probability plot of residuals. As per ([Figure: 3.12, b](#)), all points are normally distributed around the straight-line, elucidating that the independence of the residuals [36]. ([Figure: 3.12, c](#)) shows the plot of externally studentized residuals of the experimental versus predicted values. It can be noticed from ([Figure: 3.12, c](#)) the points are scattered around the horizontal line, indicating that no significant variation between actual and predicted^[141].

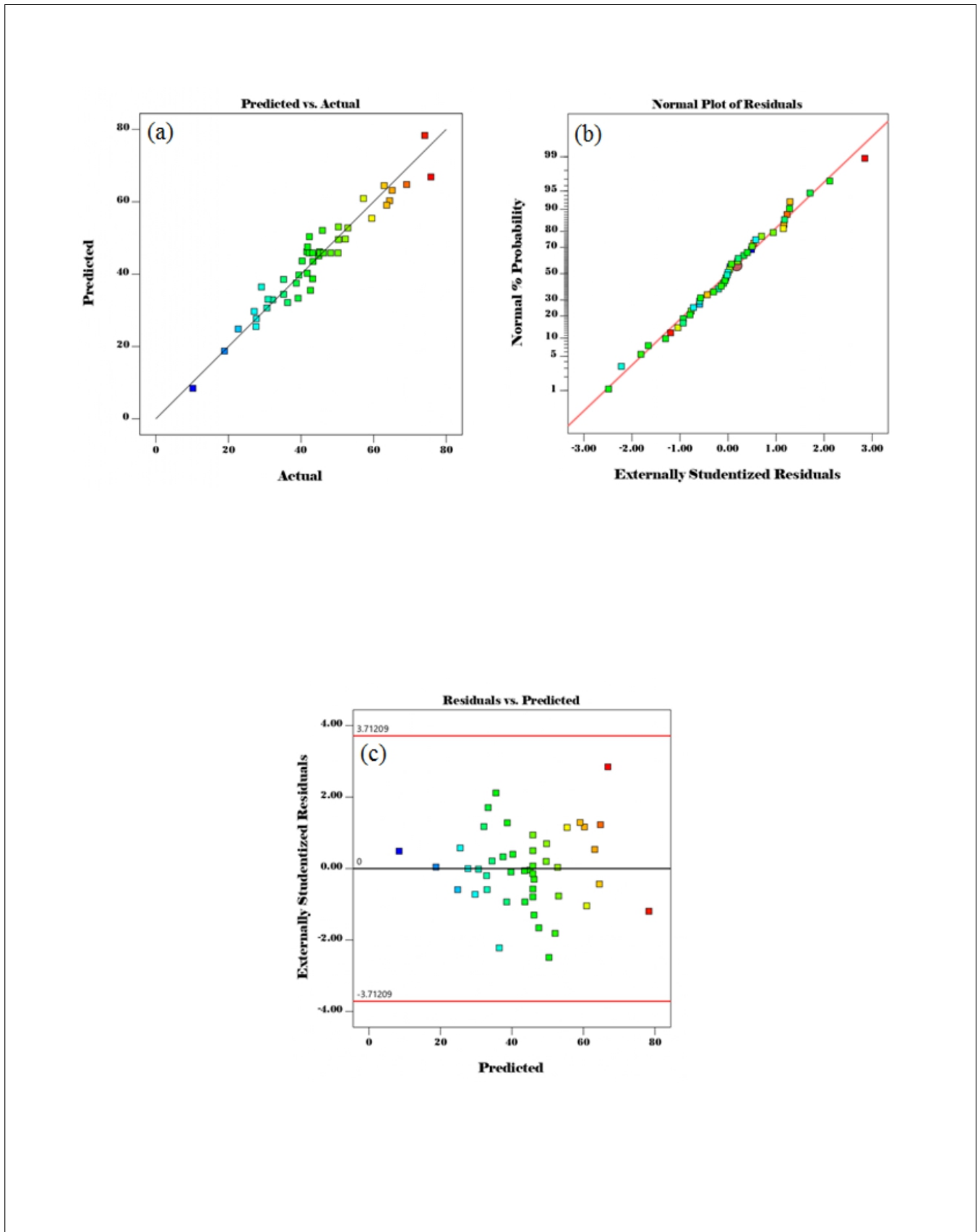


Figure 3.12: Plots of (a) actual versus predicted, (b) normal probability of the residuals, and (c) externally studentized residuals versus predicted.

3.2.2.1 Parametric optimization of BBD

Three-dimensional (3D) response surfaces are important graphical plots to explain the interaction effects of two operational factors on the RBBR removal efficiency. ([Figure: 3.13, a](#)) presents the 3D surface plot of the combined effect of ZnO loading and dose on the RBBR removal efficiency at a constant pH (7), temperature (45 °C) , and time (35 min). The obtained results from ([Figure: 3.13, a](#)) demonstrate that the RBBR removal efficiency was improved by increasing both adsorbent dose and ZnO loading. This finding relates to the high surface area resulted from ZnO nanoparticles and the higher number of active binding sites of the CHT-GLA/ZnO/ Fe_3O_4 , which are readily available to adsorb RBBR dye^[106].

([Figure:3.13, b](#)) presents the 3D surface plot of the combined effect of dose and pH on the RBBR removal efficiency at a constant ZnO loading (25%), temperature (45 °C), and time (35 min). It can be seen from ([Figure:3.13, b](#)), the RBBR removal efficiency (%) increased by decreasing the pH value from basic environment (pH=10) towards acidic environment (pH=4). The value p H_{pzc} of the CHT-GLA/ZnO/ Fe_3O_4 is 7.4 as illustrated in ([Figure:3.13, c](#)). This finding signifies that the CHT-GLA/ZnO/ Fe_3O_4 surface at pH value greater than p H_{pzc} acquires a negative charge. Thus, the CHT-GLA/ZnO/ Fe_3O_4 surface at acidic environment (pH =4) turns to a positive charge due to the increase of H^+ concentration in the solution^[142]. Accordingly, electrostatic attractions will be formed between the surface cationic groups of the CHT-GLA/ZnO/ Fe_3O_4 and the RBBR molecules as outlined in (Equation: 3.9).



The combined effect of dose and time on the RBBR removal efficiency was important. ([Figure:3.13, d](#)) presents the 3D surface plot of the important combined effects of dose and time on the RBBR removal efficiency at a constant ZnO loading (25%), pH (7), and temperature (45 °C). As can be shown from ([Figure:3.13, d](#)) that the RBBR removal efficiency did not improve significantly by increasing the contact time up to 60 min, indicating that the occupancy of the active sites on the adsorbent with RBBR molecules was very fast, and reached the equilibrium absorption of RBBR dye within a short period of time.

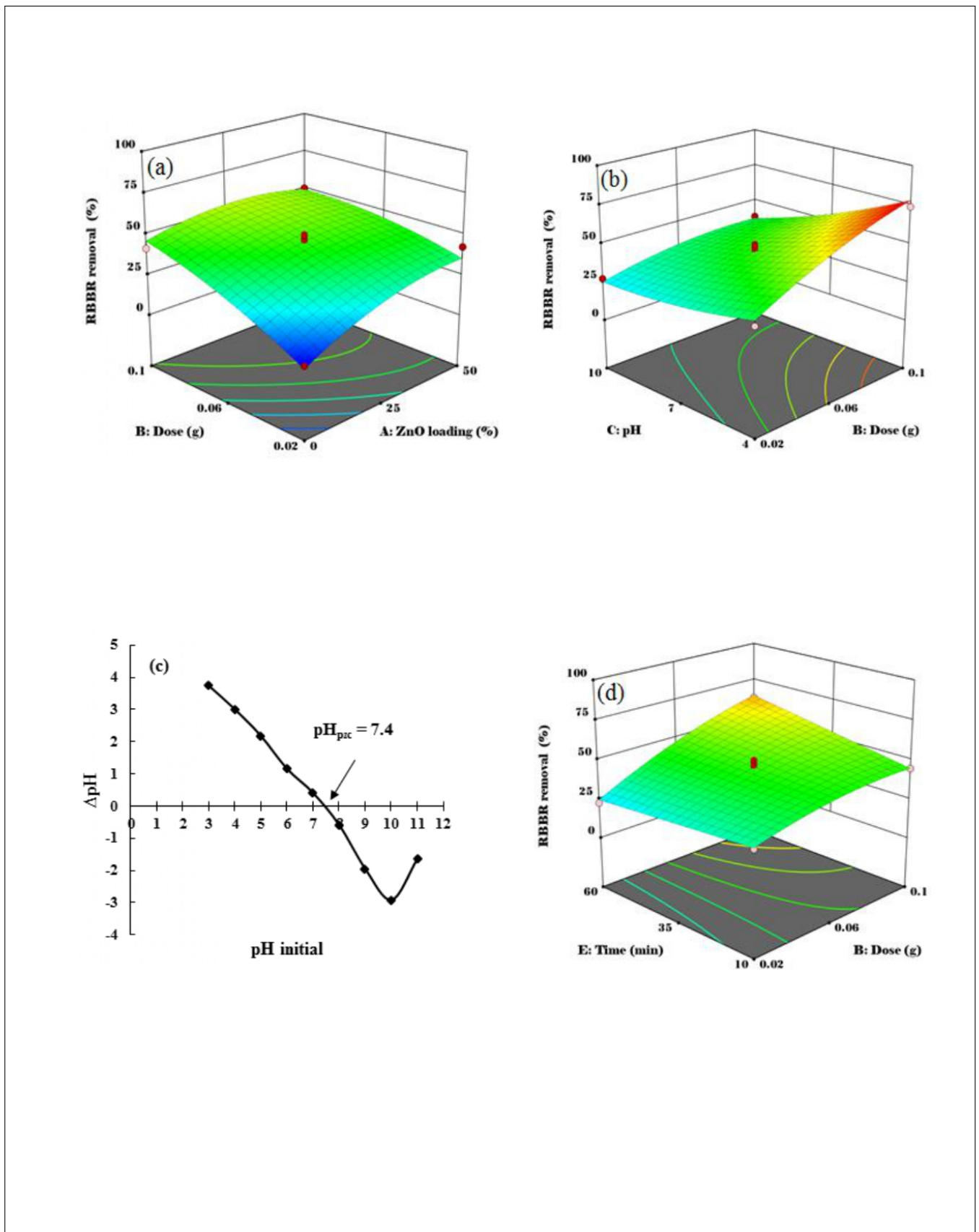


Figure 3.13: 3D plots of (a) AB, (b) BC, and (d) BE significant interactions on RBBR removal; whereas. (c) pH_{pzc} of CHT-GLA/ $\text{ZnO}/\text{Fe}_3\text{O}_4$.

3.2.3 Adsorption study

The time dependence of RBBR uptake by CHT-GLA/ZnO/ Fe_3O_4 -25 nanocomposite was monitored for better understanding to the adsorption process. In this regard, the influence of different initial RBBR concentration (range: 50-250 mg/L) on adsorption behaviour of RBBR by CHT-GLA/ZnO/ Fe_3O_4 -25 nanocomposite was investigated at fixed dose of CHT-GLA/ZnO/ Fe_3O_4 -25 (0.06 g), temperature (60 °C), solution pH (4), and solution volume (100 mL). The adsorption capacity values of CHT-GLA/ZnO/ Fe_3O_4 -25 as a function of contact time were presented in ([Figure: 3.14 ,a](#)). As can be seen, rapid qt increases at the beginning of the adsorption process for all studied concentrations which can be attributed to the existence of the adsorption active groups on the surface of CHT-GLA/ZnO/ Fe_3O_4 -25, indicating CHT-GLA/ZnO/ Fe_3O_4 -25 could be utilized as a promising adsorbent in textile dye removal. Moreover, the adsorption capacity of CHT-GLA/ZnO/ Fe_3O_4 -25 was found to increase from 60.6 to 179.7 mg/g by increasing the initial RBBR concentration from 50 to 250 mg/L. This result may be due to the higher RBBR concentration gradient, which enhances the moving of RBBR molecules to the active sites available onto the CHT-GLA/ZnO/ Fe_3O_4 -25 surface^{[143], [144]}.

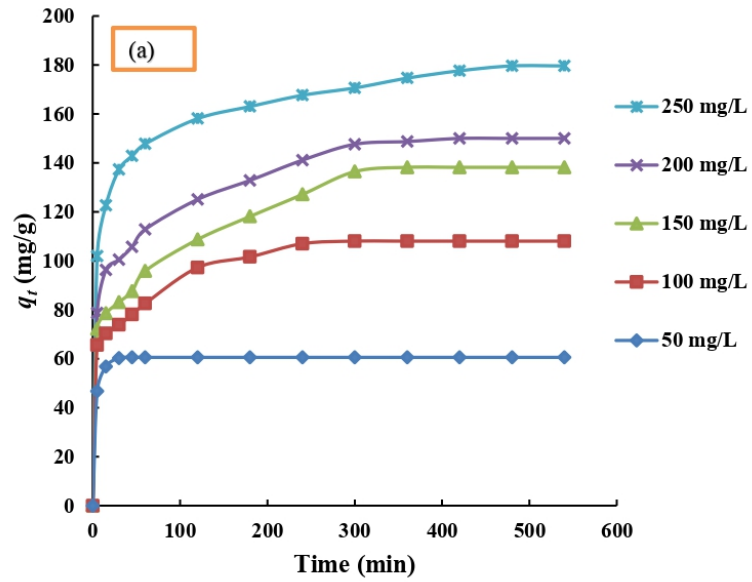


Figure 3.14: (a) Effect of the contact time on RBBR dye adsorption at different initial concentrations

3.2.4 Adsorption kinetics

To determine the controlling mechanism of the adsorption process of the RBBR on the CHT-GLA/ZnO/ Fe_3O_4 surface. The dynamical experimental data were fitted to two kinetic models: pseudo-first order (PFO)^[118] and pseudo-second order (PSO)^[119]. The parameters of the kinetic models were obtained by the non-linear equations of PFO and PSO given in (Equations: 3.10, 3.11) respectively.

$$q_t = q_e(1 - \exp^{-K_1 t}) \quad (3.10)$$

$$q_t = \frac{q_e^2 K_2 t}{1 + q_e K_2 t} \quad (3.11)$$

where q_e and q_t are the adsorption capacities (mg/g) at adsorption equilibrium and time (t), respectively. k_1 (1/min) is the PFO adsorption rate constant and k_2 (g/mg min) is the PSO adsorption rate constant. The calculated parameters of the kinetic models are listed in (Table: 3.8). It can be seen from (Table: 3.8) that the R^2 values of the PSO was higher than the PFO. Moreover, the calculated q_e of the PSO was closer to the experimental q_e compared to the values of calculated q_e for the PFO. The obtained results clarified that the adsorption of RBBR dye onto CHT-GLA/ZnO/ Fe_3O_4 surface is a chemisorption process including electrostatic interactions, which are happened between the positive charges and cationic groups available on the CHT-GLA/ZnO/ Fe_3O_4 nanocomposite surface with the negative charges ($-SO_3^-$) of the RBBR dye^[145].

Table 3.8: PFO and PSO kinetic parameters for RBBR dye adsorption on CHT-GLA/ZnO/ Fe_3O_4 -25.

Concentration(mg/L)	$q_{eexp}(mg/g)$	PFO			PSO		
		$q_{ecal}(mg/g)$	$k_1(1/min)$	R^2	$q_{ecal}(mg/g)$	$k_2 * 10^{-2}(g/mgmin)$	R^2
50	60.6	60.3	0.292	0.99	61.3	1.152	0.99
100	108.1	97.9	0.139	0.80	104.6	0.154	0.91
150	138.3	126.8	0.044	0.77	133.1	0.063	0.98
200	150.0	135.1	0.091	0.82	143.8	0.089	0.93
250	179.7	163.2	0.139	0.90	176.5	0.116	0.97

3.2.5 Adsorption isotherm

The adsorption isotherms are applied to understand the relationship between equilibrium adsorption capacity of the CHT-GLA/ZnO/ Fe_3O_4 nanocomposite and initial concentration of RBBR^[143]. The equilibrium adsorption is crucial parameter in the describing and explaining the correlation between CHT-GLA/ZnO/ Fe_3O_4 nanocomposite and RBBR molecules. The affinity and adsorption capacity of CHT-GLA/ZnO/ Fe_3O_4 -25 nanocomposite to adsorb RBBR dye from aqueous solution were elucidated by fitting the experimental data to Langmuir^[122], Freundlich^[123], and Temkin^[124] isotherm models. The Langmuir model indicates that all adsorption sites are equivalent and a monolayer adsorption towards pollutants is occurred on a homogeneous surface of adsorbent^[143]. The Freundlich model is generally used to describe a multilayer adsorption towards pollutants is occurred on a heterogeneous surface of adsorbent [18]. Moreover, the Temkin model assumes there is a linear relationship between adsorption heat and coverage by taking into consideration the temperature effect^[146]. The parameters of the isotherms were obtained by the non-linear equations of Langmuir, Freundlich, and Temkin as presented in (Equations: 3.12, 3.13, 3.14), respectively.

$$q_t = \frac{q_{max}K_aC_e}{1 + K_aC_e} \quad (3.12)$$

$$q_e = K_fC_e^{1/n} \quad (3.13)$$

$$q_t = \frac{RT}{b_T} \ln K_aC_e \quad (3.14)$$

where q_{max} (mg/g) is the calculated adsorption capacity of the CHT-GLA/ZnO/ Fe_3O_4 , and K_a (L/mg) is the Langmuir equilibrium constant. K_f (mg/g)(L/mg)^{1/n} and n are constants related to the Freundlich model. K_T (L/mg) and b_T (J/mol) are Temken constants related to the equilibrium binding, and adsorption heat. T(K) and R(8.314J/molK) represents the temperature and gas constant, respectively. (**Figure:** 3.15, **b**) and (**Table:** 3.9) show the fitting parameters and curves of isotherms, respectively. As per the correlation coefficient (R^2) of models, the Freundlich model ($R^2 = 0.97$) and Temkin model ($R^2 = 0.97$) are higher than that of the Langmuir model ($R^2 = 0.94$), Thus, the adsorption process of RBBR by CHT-GLA/ZnO/ Fe_3O_4 is more in line with the Freundlich and Temkin models, indicating the heterogeneous character of the RBBR physical and chemical adsorption onto CHT-GLA/ZnO/ Fe_3O_4 surface^[147]. The

q_{max} of RBBR on CHT-GLA/ZnO/ Fe_3O_4 -25 was found as 176.6 mg/g at 60 °C.

(Table: 3.10) summarizes the comparison the q_{max} of the CHT-GLA/ZnO/ Fe_3O_4 -25 with other adsorbents reported in previous works toward RBBR. These results of (Table: 3.10) demonstrate that the CHT-GLA/ZnO/ Fe_3O_4 -25 had favorable adsorption ability for the removal of organic dyes from wastewater.

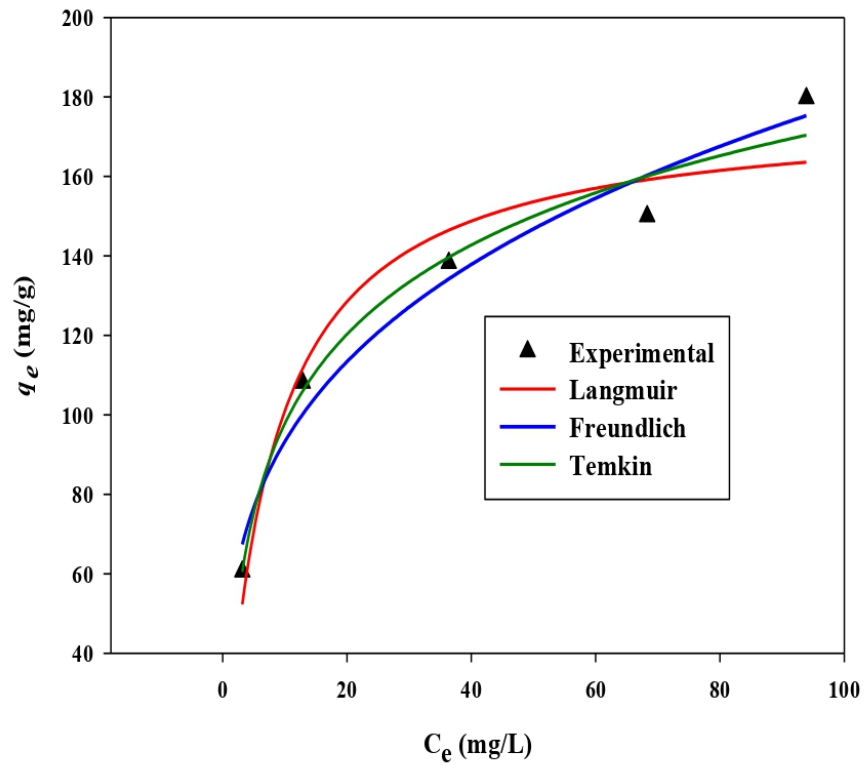


Figure 3.15: adsorption isotherms of RBBR by CHT-GLA/ZnO/Fe₃O₄-25 (dosage 0.06g, pH of solution 4, temperature 45 °C, agitation speed = 100 strokes and volume of solution = 100 mL).

Table 3.9: Parameters of the Langmuir, Freundlich and Temkin isotherm models for RBBR dye adsorption on CHT-GLA/ZnO/ Fe_3O_4 -25 at 60 °C

Adsorption isotherm	Parameter	Value
Langmuir	qm (mg/g)	176.6
	Ka (L/mg)	0.133
	R^2	0.94
Freundlich	Kf (mg/g) (L/mg) ^{1/n}	48.76
	N	3.54
	R^2	0.97
Temkin	KT (L/mg)	0.71
	bT (J/mol)	85.4
	R2	0.97

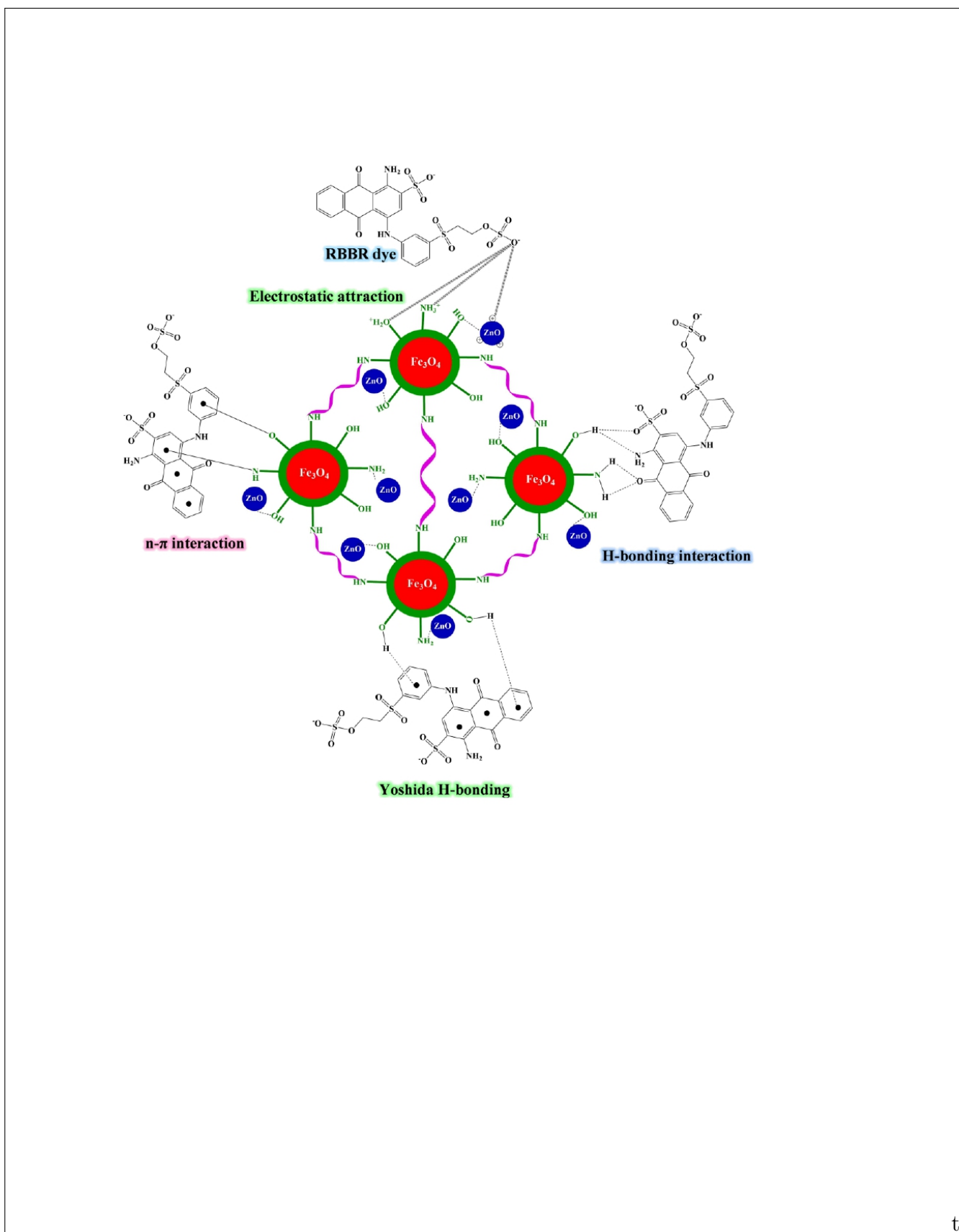
Table 3.10: Comparison of the adsorption capacity of RBBR dye by various adsorbents

Adsorbents	qm (mg/g)	References
Magnetic chitosan-glutaraldehyde/zinc oxide/ Fe_3O_4 nanocomposite	179.7	This study
Chitosan-tripolyphosphate/kaolin composite	687.2	[148]
Graphene oxide-ionic liquid	416.7	[149]
Sawdust-based activated carbon	368.5	[150]
Polyaniline/chitosan composite	303.03	[128]
ZnO-polyacrylonitrile-hinokitiol	267.37	[130]
Chitosan-alkali lignin composite	111.11	[133]
Chitosan/SiO ₂ /carbon nanotubes magnetic nanocomposite	97.08	[134]
Magnesium hydroxide coated bentonite	66.90	[151]
Borax cross-linked Jhingan gum hydrogel	9.884	[136]

3.2.6 Adsorption mechanism

The adsorption mechanism of RBBR on the CHT-GLA/ZnO/ Fe_3O_4 nanocomposite surface was sketched depending on of the presence of active adsorption sites such as hydroxyl (-OH), amino ($-NH_2$) and $Zn(OH)^+$, as shown in ([Figure: 3.16](#)). At first, CHT-GLA/ZnO/ Fe_3O_4

nanocomposite surface can obtain positive charges in an acidic solution due to $\text{pH} < \text{pH}_{\text{pzc}}$. The positive charges of the CHT-GLA/ZnO/ Fe_3O_4 nanocomposite surface can be obtained from different sources such as hydroxyl (-OH), and amine ($-\text{NH}_2$) protonated groups, as well as positive charges formed from ZnO nanoparticles. Electrostatic interactions are prime character for the RBBR adsorption because of the plenty of positive charges and cationic groups on the CHT-GLA/ZnO/ Fe_3O_4 nanocomposite surface, which are attracted with the negative charges ($-\text{SO}_3^-$) of the RBBR dye. Various studies have been reported using positive charges of ZnO nanoparticles formed in the acidic medium to adsorb organic dyes through electrostatic interactions^{[116], [152]}. Hydrogen interactions designated by H-bonding and Yoshida H-bonding from significant interactions that could be played an important role in adsorption of RBBR dye. These interactions (H-bonding) and (Yoshida H-bonding) are formed between the free H and H-OH (hydrogen of hydroxyl) available on the CHT-GLA/ZnO/ Fe_3O_4 nanocomposite surface with N and O groups and the aromatic system of the RBBR dye, respectively^[153]. Lastly, π - interactions occur between the electron-donating system represented by groups containing N and O in the CHT-GLA/ZnO/ Fe_3O_4 nanocomposite and the electron-accepting system represented by the aromatic rings of the RBBR dye^[101].



t

Figure 3.16: Illustration of the possible interaction between CHT-GLA/ZnO/Fe₃O₄ nanocomposite surface and RBBR dye including electrostatic attraction, hydrogen bonding interactions, Yoshida H-bonding, and n- interactions.

3.3 Results And Discussion Of chitosan-Benzil/ $\text{ZnO}/\text{Fe}_3\text{O}_4$

($\text{Cs} - \text{Bz}/\text{ZnO}/\text{Fe}_3\text{O}_4$)

3.3.1 Characterization of $\text{Cs-Bz}/\text{ZnO}/\text{Fe}_3\text{O}_4$

3.3.1.1 Morphological Characterization for the $\text{Cs} - \text{Bz}/\text{ZnO}/\text{Fe}_3\text{O}_4$

SEM-EDX analysis was carried out in order to identify the surface morphology and chemical composition. (**Figure: 3.17**) exhibits the SEM images and EDX spectra of (a) $\text{Cs-Bz}/\text{Fe}_3\text{O}_4$, (b) $\text{Cs-Bz}/\text{ZnO-25}/\text{Fe}_3\text{O}_4$, and (c) $\text{Cs-Bz}/\text{ZnO-25}/\text{Fe}_3\text{O}_4$ after adsorption of RBBR. As per (**Figure: 3.17, a**), the surface morphology of $\text{Cs-Bz}/\text{Fe}_3\text{O}_4$ is displayed which appears as an irregular and heterogenous surface with presence of crevices. The EDX spectra of $\text{Cs-Bz}/\text{Fe}_3\text{O}_4$ detects the elements C, O, and N which can be ascribed to backbone Cs as well as Fe corresponding to the magnetic Fe_3O_4 . (**Figure: 3.17, b**) shows the SEM of $\text{Cs-Bz}/\text{ZnO-25}/\text{Fe}_3\text{O}_4$ which appears as a surface containing different sizes of protrusions. This observation signifies the uniform distribution of the ZnO nanoparticles in the polymeric matrix of the $\text{Cs-Bz}/\text{Fe}_3\text{O}_4$, while the existence of the Zn in the corresponding EDX spectrum reconfirmed the successful loading of the ZnO nanoparticles in the polymeric matrix of $\text{Cs-Bz}/\text{Fe}_3\text{O}_4$. On the other hand, the surface morphology of $\text{Cs-Bz}/\text{ZnO-25}/\text{Fe}_3\text{O}_4$ after RBBR adsorption (**Figure: 3.17, c**) transformed to be more compact, with less visible pores and cavities due to loading of RBBR dye molecules onto its surface. Moreover, the detected sulfur (S) atom in the corresponding EDX spectrum reconfirmed the availability of RBBR dye molecules on the $\text{Cs-Bz}/\text{ZnO-25}/\text{Fe}_3\text{O}_4$ due to the adsorption process.

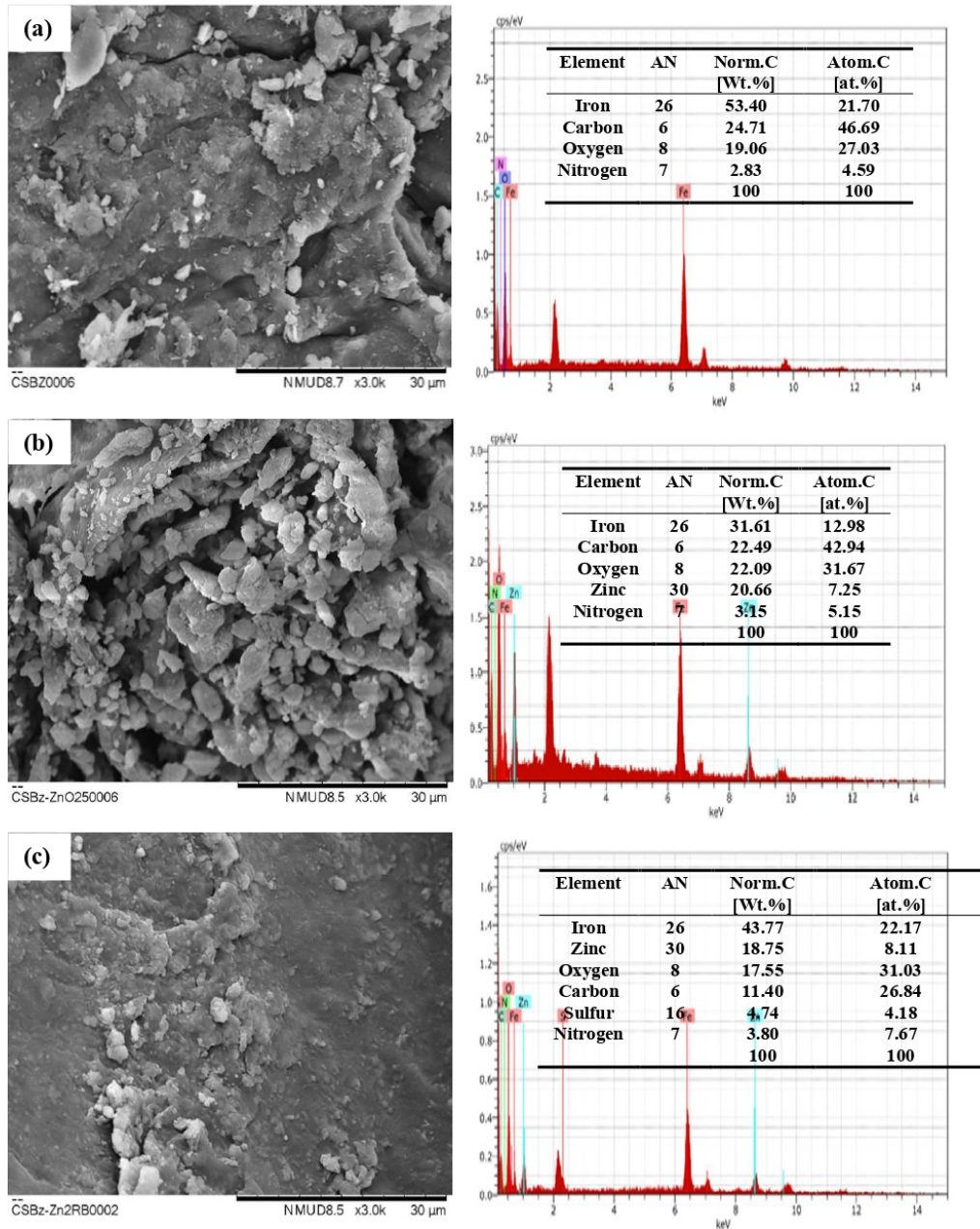


Figure 3.17: SEM images and EDX spectra of (a) Cs-Bz/ Fe_3O_4 , (b) Cs-Bz/ZnO-25/ Fe_3O_4 nanocomposite, and (c) Cs-Bz/ZnO-25/ Fe_3O_4 nanocomposite after adsorption of RBBR dye at magnification power 3000x.

3.3.1.2 FT-IR spectral analysis

Moreover, FTIR analysis was carried out in order to determine the fundamental functional groups of Cs-Bz/ZnO-25/ Fe_3O_4 before and after RBBR adsorption which were displayed in ([Figure: 3.18, a](#)).and ([Figure: 3.18, b](#)), respectively. The bands illustrated in ([Figure: 3.18, a](#)) at 3600 cm^{-1} , 3342 cm^{-1} , 2872 cm^{-1} , 1320 cm^{-1} , 1061 cm^{-1} , 565 cm^{-1} and 465 cm^{-1} are ascribed to the following groups/bonds: -OH stretching, $-NH_2$ asymmetric stretching, C-H asymmetric stretching, C-N stretching, C-O stretching, FeO bending, and O-Zn-O bending, respectively^{[154], [155], [156], [157], [158]}. In addition, the peak at 1639 cm^{-1} indicates that the imine function C=N was formed by condensation reaction between the carbonyl groups of Benzil and amino groups of Cs^[159]. In same context, the spectrum observed at 1557 cm^{-1} can be attributed to the bending vibration of N-H. The FTIR spectrum of the Cs-Bz/ZnO-25/ Fe_3O_4 nanocomposite after RBBR adsorption is shown ([Figure: 3.18, b](#)), which shows a reduction in the intensity of some bonds especially -OH and $-NH_2$. This observation clearly indicates the involvement of these certain functional groups in capturing the RBBR dye molecules. Furthermore, the appearance of the new band at 1500 cm^{-1} (refers to C=C stretching of aromatic rings of RBBR) is another evidence of loading RBBR on the surface of Cs-Bz/ZnO-25/ Fe_3O_4 .

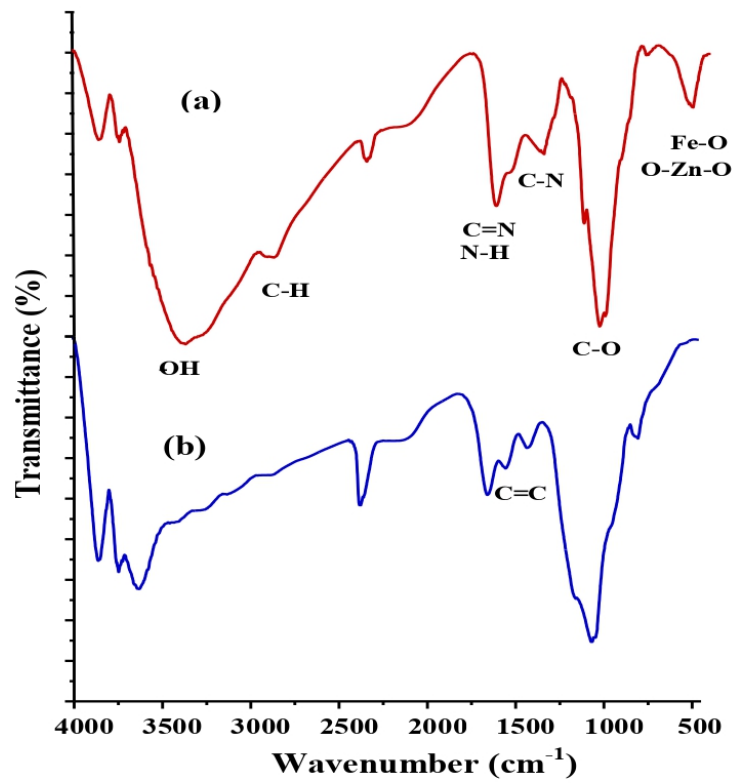


Figure 3.18: FTIR spectra of (a) Cs-Bz/ZnO-25/ Fe_3O_4 , and (b) Cs-Bz/ZnO-25/ Fe_3O_4 after adsorption of RBBR dye

3.3.1.3 Physio-chemical properties

The results of surface area analysis and amino group contents (%) of Cs-Bz/ Fe_3O_4 , Cs-Bz/ZnO-25/ Fe_3O_4 , and Cs-Bz/ZnO-50/ Fe_3O_4 are presented in (Table: 3.11). The pH potentiometric titration analysis shows a gradual descend in the amino group content with more loading of ZnO nanoparticles as shown in the following materials: Cs-Bz/ Fe_3O_4 (45.03%) Cs-Bz/ZnO-25/ Fe_3O_4 (38.64%) Cs-Bz/ZnO-50/ Fe_3O_4 (32.01%). This observation can be assigned to the replacement of certain amount of Cs with ZnO nanoparticles which leads to this reduction in amino group content. Another possible reason can be ascribed to the coordination bonds between free electron pair for nitrogen atoms with the empty orbital of the zinc^{[160], [109]}. On the other hand, opposite trend was observed with surface area property, which shows remarkable improvement in the surface area with loading more ZnO nanoparticles in the polymeric matrix of the following materials: Cs-Bz/ZnO-50/ Fe_3O_4 (18.8 m^2/g) Cs-Bz/ZnO-25/ Fe_3O_4 (9.42 m^2/g) Cs-Bz/ Fe_3O_4 (1.01 m^2/g). From these results, it can be concluded that loading 50% of ZnO nanoparticles in the polymeric matrix of Cs-Bz/ Fe_3O_4 is reasonable for improving its surface area by 18.6-fold. This result signifies a uniform distribution of high surface area ZnO nanoparticles with obvious ability to improve the surface area property. From adsorption standpoint, even though Cs-Bz/ZnO-50/ Fe_3O_4 has the highest surface area over both Cs-Bz/ZnO-25/ Fe_3O_4 , and Cs-Bz/ Fe_3O_4 , however, the best adsorptive property was achieved with Cs-Bz/ZnO-25/ Fe_3O_4 over Cs-Bz/ZnO-50/ Fe_3O_4 and Cs-Bz/ Fe_3O_4 . This observation can be explained according to the following facts: (i) Cs-Bz/ZnO-50/ Fe_3O_4 has the highest surface area (18.8 m^2/g) and lowest amino group content (32.01(%)), (ii) Cs-Bz/ Fe_3O_4 has the lowest surface area (1.01 m^2/g) and highest amino group content (45.03 (%)), (iii) Cs-Bz/ZnO-25/ Fe_3O_4 has an average surface area ((9.42 m^2/g) and amino group content (38.64 (%)) over both Cs-Bz/ Fe_3O_4 and Cs-Bz/ZnO-50/ Fe_3O_4 materials. In fact, adsorption process is a surface phenomenon and depends mainly on the available adsorption active sites on the adsorbents surface, in addition to the surface area of the adsorbent. Therefore, Cs-Bz/ZnO-25/ Fe_3O_4 has the perfect balancing and tuning between available adsorption active sites (amino group content) and available surface area of the adsorbent. As a result, the best adsorptive removal of RBBR was achieved by best composite formulation of Cs-Bz/ZnO-25/ Fe_3O_4 .

Table 3.11: Material characteristics of the CS-Bz/ Fe_3O_4 , CS-Bz/ZnO-25/ Fe_3O_4 , and CS-Bz/ZnO-50/ Fe_3O_4

Analysis	CS-Bz/ Fe_3O_4	CS-Bz/ZnO-25/ Fe_3O_4	CS-Bz/ZnO-50/ Fe_3O_4
pH-potentiometric titration $-NH_2$ (%)	45.03	38.64	32.01
BET surface area (m^2/g)	1.01	9.42	18.8
Mean pore diameter (nm)	15.57	5.88	6.94

3.3.1.4 XRD analysis

The amorphous and crystalline nature of the preparer composite materials were investigated by X-ray diffraction analysis, which is considered one of the best techniques that provides this information. ([Figure: 3.19](#)) shows the XRD patterns of (a) Cs-Bz/ Fe_3O_4 , (b) Cs-Bz/ZnO-25/ Fe_3O_4 , and (c) Cs-Bz/ZnO-50/ Fe_3O_4 nanocomposites. The XRD pattern of (a) Cs-Bz/ Fe_3O_4 displayed the peaks at $2\theta = 30^\circ, 35^\circ, 43^\circ, 53^\circ, 57^\circ,$ and 62° in ([Figure: 3.19, a](#)), which are the characteristic peaks of Fe_3O_4 ^[161], and indicates the successful synthesis of magnetic Cs. The XRD patterns of Cs-Bz/ZnO-25/ Fe_3O_4 and Cs-Bz/ZnO-50/ Fe_3O_4 nanocomposites were shown in ([Figure: 3.19, b](#)) and ([Figure: 3.19, c](#)), respectively. These spectra show an observable increase in the band intensities after loading ZnO nanoparticles into polymeric matrix of Cs-Bz/ Fe_3O_4 at different ratios. This observation reinforces the intercalation and uniform distribution of ZnO nanoparticles in the polymeric structure of Cs-Bz/ Fe_3O_4 .

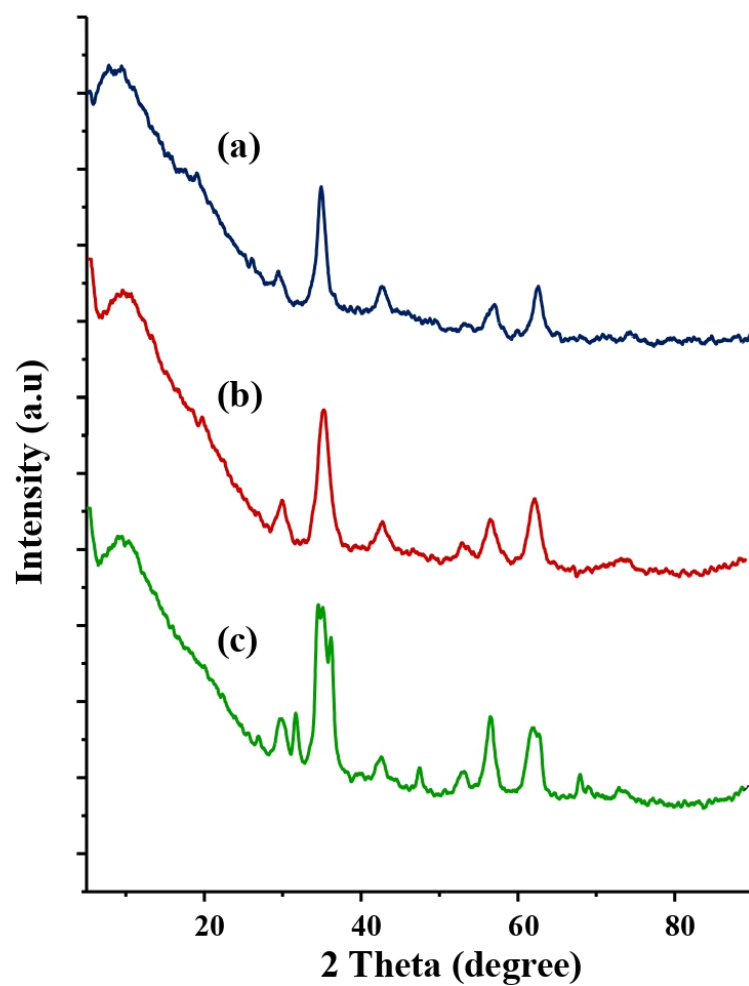


Figure 3.19: XRD spectra of (a) Cs-Bz/ Fe_3O_4 , (b) Cs-Bz/ZnO-25/ Fe_3O_4 , and (c) Cs-Bz/ZnO-50/ Fe_3O_4 .

3.3.2 BBD model analysis

The experimental data obtained from *BBD* was validated by analysis of variance (ANOVA) as recorded in ([Table: 3.12](#)). The ANOVA test shows the following terms: F-value (42.98), and p-value (< 0.0001). The value of p less than 0.05 is considered significant as per the conditions of model^[162]. Moreover, the predicted and experimental statistical values were found in line with each other and showed a high value (0.97) of the correlation coefficient (R^2). According to ([Table: 3.12](#)), B, C, E, AB, AC, CD, A^2 , B^2 , C^2 , and E^2 are significant terms for removing RBBR dye. Thus, the expression of the quadratic regression model illustrates the empirical relationship between the RBBR removal (response) and significant variables is presented in the (equation: 4.15).

$$\begin{aligned} \text{RBBR Removal (\%)} = & +73.60 + 12.39B - 32.83C - 6.75AB + 6.88AC - 13.53CD - 13.12A^2 \\ & -7.26 B^2 - 21.01 C^2 \end{aligned} \quad (3.15)$$

Table 3.12: ANOVA analysis of RBBR removal.

Source	Sum of Squares	Df	Mean Square	F-value	p-value
Model	27348.18	20	1367.41	42.98	< 0.0001
A-ZnO loading	25.00	1	25.00	0.7859	0.3838
B-Adsorbent dosage	2455.20	1	2455.20	77.18	< 0.0001
C-pH	17246.26	1	17246.26	542.14	< 0.0001
D-Temp.	131.68	1	131.68	4.14	0.0526
E-Time	879.12	1	879.12	27.64	< 0.0001
AB	182.25	1	182.25	5.73	0.0245
AC	189.06	1	189.06	5.94	0.0222
AD	98.01	1	98.01	3.08	0.0915
AE	54.02	1	54.02	1.70	0.2044
BC	18.06	1	18.06	0.5678	0.4582
BD	8.41	1	8.41	0.2644	0.6117
BE	12.60	1	12.60	0.3962	0.5348
CD	731.70	1	731.70	23.00	< 0.0001
CE	24.01	1	24.01	0.7548	0.3932
DE	2.25	1	2.25	0.0707	0.7925
A^2	1502.93	1	1502.93	47.24	< 0.0001
B^2	459.52	1	459.52	14.44	0.0008
C^2	3854.07	1	3854.07	121.15	< 0.0001
D^2	32.13	1	32.13	1.01	0.3245
E^2	116.67	1	116.67	3.67	0.0670
Residual	795.29	25	31.81		
Cor Total	28143.47	45			

(Figure: 3.20, a) shows the normal probability versus externally studentized residuals. This plot determines whether residuals follow a normal distribution. In a normal distribution, the points should lay on an approximately straight line. As per (Figure: 3.20, a), the points lie along a straight line and, consequently, it can be assumed that they are normally distributed^[163]. The normal distributions of the residuals signify the accuracy of the assumptions, and the

independence of the residuals^[164]. The relationship between the actual and predicted values for RBBR dye removal is shown in (Figure: 3.20, b). From (Figure: 3.20, b) it can be deduced that the predicted and actual points were mostly close to each other. This observation signifies that the experimental results for this research are highly acceptable.

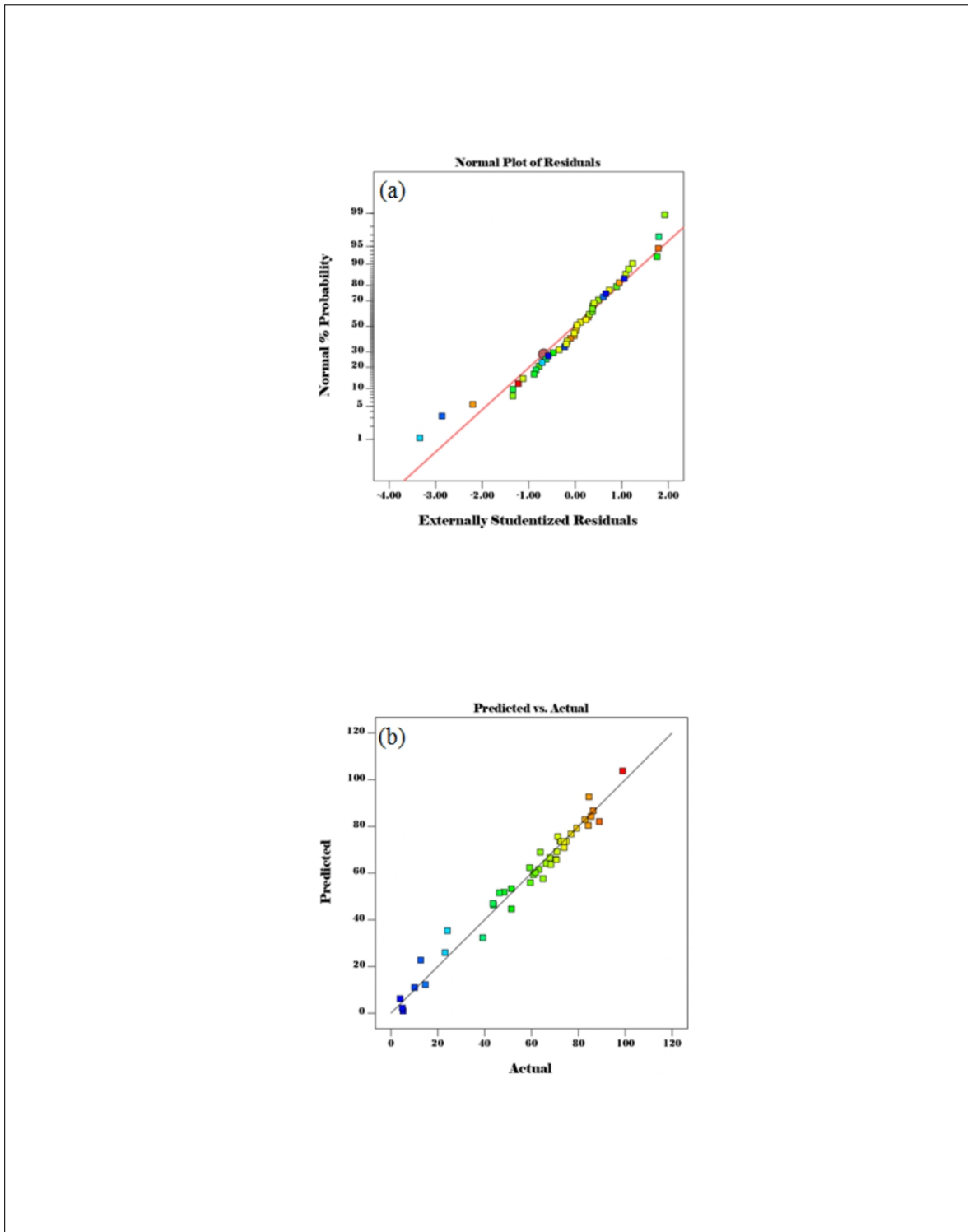
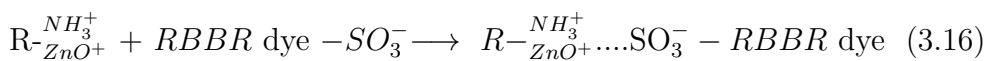


Figure 3.20: Plots of (a) residuals normal probability, and (b) predicted vs. actual relationship of RBBR dye removal (%).

3.3.2.1 Parametric optimization of BBD

Parametric optimization of BBD The surface and contour plots were plotted graphically to conclude the significance of binary interactions between different selected variables, and optimization of the behavior of RBBR dye adsorption^[165]. (**Figure: 3.21, a**), and (**Figure: 3.21, b**), represent response surface plots (3D and 2D contour, respectively) for the parametric interaction between loading of ZnO nanoparticles (A) and working solution pH (C) as a statistically significant function (p value=0.0222). The other operation parameters (adsorbent dose of 0.04, temperature 60 °C, and time of 10 min) were kept constant. It can be observed from (**Figure: 3.21, a**), and (**Figure: 3.21, b**) that adjusting the solution pH from solution pH 10 towards solution pH 4 is responsible for improving the efficiency of RBBR removal (%) from 3.9 % to 98.9 %. In order to understand this improvement in the adsorptive behavior of Cs-Bz/ZnO-25/ Fe_3O_4 in acidic solution environment. The pHPzc of the Cs-Bz/ZnO-25/ Fe_3O_4 was determined to be 7.5 (**Figure: 3.21, c**). It can be concluded from (**Figure: 3.21, c**), at solution pH higher than pHPzc (basic environment) poor removal of RBBR will be observed. This observation can be attributed to the high competition between the RBBR ions and OH^- existing in the bulk solution, which leads to repulsion. In the same context, when the solution pH goes below pHPzc (acidic environment) the surface of the Cs-Bz/ZnO-25/ Fe_3O_4 will acquire a positive charge due to protonation (conversion) of amino ($-NH_2$) group into protonated (cationic) amino ($-NH_3^+$) group. As a result, an intense electrostatic attraction can be occurred between free amino ($-NH_3^+$) groups and ZnO positive charges of Bz/ZnO-25/ Fe_3O_4 with sulfonate ($-SO_3^-$) groups of the RBBR dye as depicted in (equation: 4.16), where R is Bz/ZnO-25/ Fe_3O_4 .



The second statistically significant interaction (p-value = 0.0245) was observed between ZnO loading (A) and adsorbent dose (B), while other operation parameters (solution pH of 4, temperature of 60 °C, and time of 10 min) were kept constant. (**Figure: 3.22, a**) and (**Figure: 3.22, b**), show the 3D response surface plots and 2D contour, respectively. It can be confirmed from (Figure 3.22, a) and (**Figure: 3.22, b**), that the RBBR removal efficiency increased by increasing both ZnO loading and adsorbent dose. This finding can be attributed to the role

of uniform distribution of ZnO nanoparticles into polymeric matrix of Cs-Bz/ Fe_3O_4 , which eventually leads to an improvement in the surface area as previously discussed. Moreover, higher adsorbent dose of Cs-Bz/ZnO-25/ Fe_3O_4 will offer greater number of active adsorption sites to capture more RBBR dye molecules from the bulk solution.

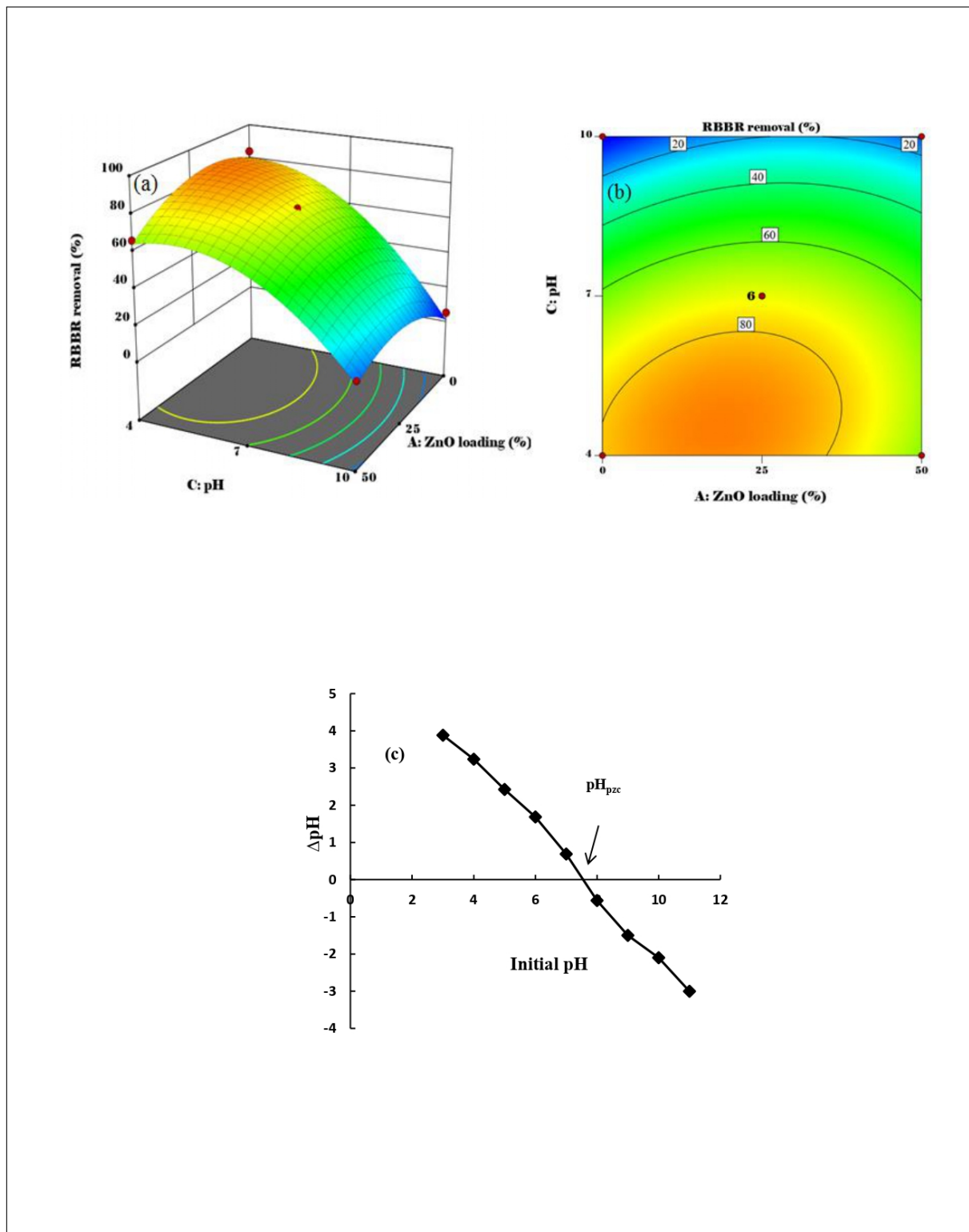


Figure 3.21: (a) 3D plot, and (b) 2D contour plot of the parametric interaction between AC, and (c) pH_{pzc} of Cs-Bz/ZnO-25/ Fe_3O_4 .

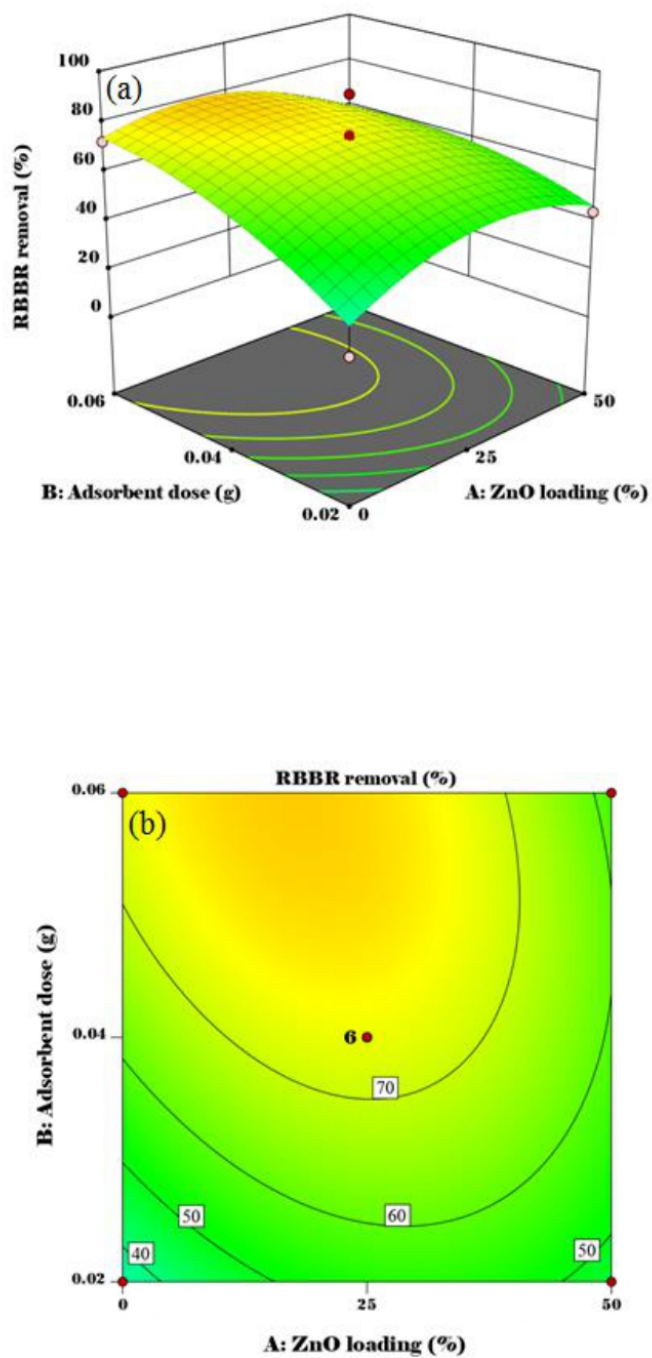


Figure 3.22: (a) 3D, (b) 2D contour plot of the parametric interaction between AB on RBBR removal.

The parametric interaction of solution pH (C) with temperature (D) was the last statistically significant interaction for removal of RBBR with p-value < 0.0001 , by keeping other operation parameters (ZnO loading 25%, adsorbent dose of 0.04 , and time of 10 min) constant. ([Figure: 3.23, a](#)) and ([Figure: 3.23, b](#)) exhibit 3D response surface plots and 2D contour for the parametric interaction of solution pH (C) and temperature (D), respectively. It can be revealed from ([Figure: 3.23, a](#)) and ([Figure: 3.23, b](#)), that RBBR removal efficiency increased by raising the solution temperature from 30 C to 60 C. This output indicates that the adsorption process of RBBR by Cs-Bz/ZnO/ Fe_3O_4 surface is an endothermic in nature, and will be further discussed in the following section (Adsorption thermodynamics).

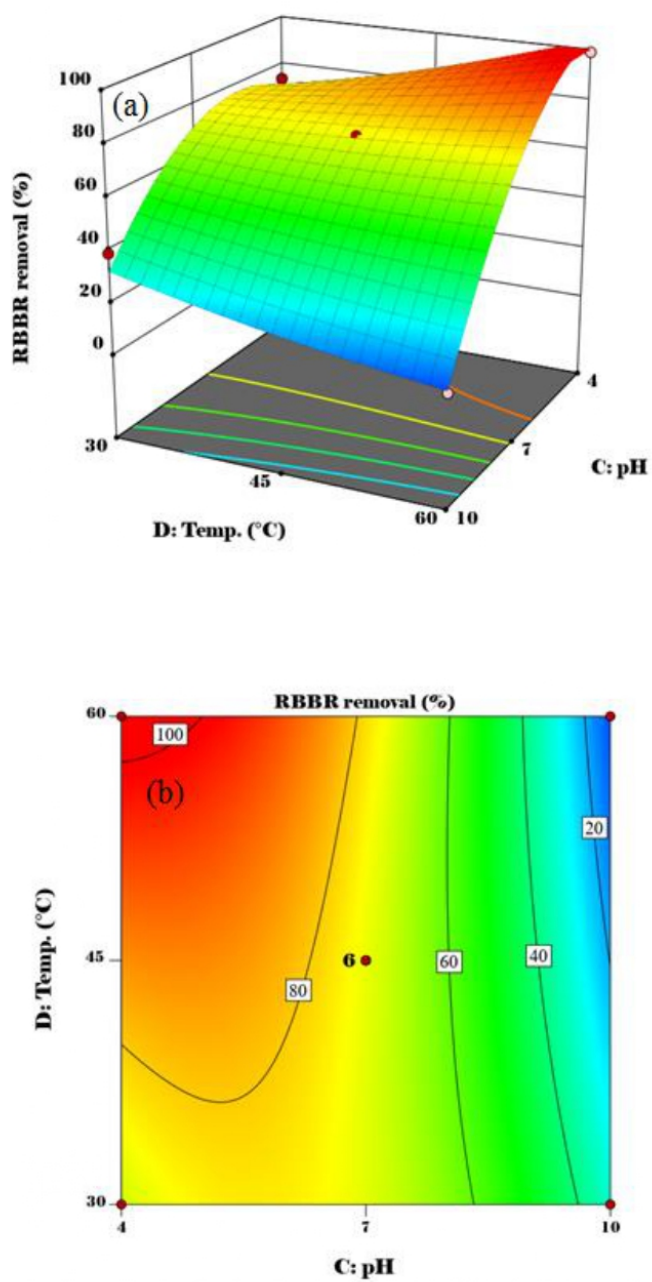


Figure 3.23: (a) 3D response surface plot, (b) 2D contour plot of RBBR dye removal demonstrating the parametric interaction between CD.

3.3.3 Adsorption study

The ability of Cs-Bz/ZnO-25/ Fe_3O_4 for capturing RBBR was investigated in batch adsorption mode at different initial RBBR concentrations (50-300 mg/L), while the other working parameters (Cs-Bz/ZnO-25/ Fe_3O_4 dose=0.04 g, solution pH = 4, temperature = 60 °C, and shaking speed = 100 rpm) were kept constant. (Figure: 3.24) illustrates the adsorption capacity (mg/g) of Cs-Bz/ZnO-25/ Fe_3O_4 versus contact time (min). From (Figure: 3.24), the adsorption capacity of Cs-Bz/ZnO-25/ Fe_3O_4 towards RBBR dye increases from 95.6 to 570.8 mg/g with increasing initial concentrations of RBBR from 50 to 300 mg/L. This phenomenon can possibly assign to the higher collision rate between RBBR and Cs-Bz/ZnO-25/ Fe_3O_4 surface at higher initial RBBR concentration^[40]. Extra time was required to attain the equilibrium for higher RBBR concentration due to a tendency of RBBR to pass deeper into inner surface of the Cs-Bz/ZnO-25/ Fe_3O_4 and be captured by active adsorption sites. This observation reveals that the initial RBBR concentration has a fundamental role in the adsorption capacity of RBBR by Cs-Bz/ZnO-25/ Fe_3O_4 adsorbent. Similar approaches were found for the adsorption of anionic dyes by various crosslinked Cs nanocomposite derivatives^{[142], [88], [145]}.

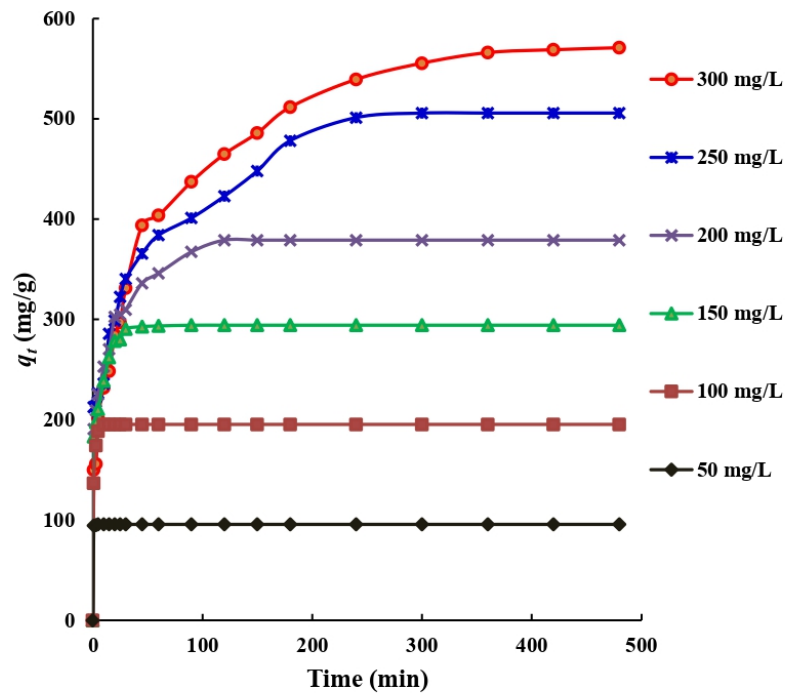


Figure 3.24: Influence of initial RBBR concentrations vs. contact time on adsorption capacity of Cs-Bz/ZnO-25/ Fe_3O_4 . Experimental conditions (dose = 0.04 g, pH = 4, temperature = 60 °C, agitation speed = 100 rpm, and vol. = 100 mL).

3.3.4 Adsorption kinetics

The kinetics always has a great importance to understand the behavior of the adsorption process. The dynamical empirical data was tested by two types of kinetic models namely the pseudo-first-order^[118], and the pseudo-second-order^[119] as presented in the following nonlinear (equations: 3.17 , 3.18) respectively.

$$q_t = q_e(1 - \exp^{-K_1 t}) \quad (3.17)$$

$$q_t = \frac{q_e^2 K_2 t}{1 + q_e K_2 t} \quad (3.18)$$

where q_t is the quantity of RBBR dye adsorbed per unit mass on adsorbent at any time t (mg/g), q_e is the quantity of RBBR dye adsorbed per unit mass on adsorbent at equilibrium (mg/g), $k_1(1/min)$, and $k_2(g/mgmin)$ are the rates constant for the pseudo-first-order and the pseudo-second-order models, respectively. (Table: 3.13) illustrates the obtained data from both kinetic models.

Table 3.13: Kinetic parameters for RBBR adsorption by Cs-Bz/ZnO-25/ Fe_3O_4

Concentration(mg/L)	$q_{eexp}(mg/g)$	PFO			PSO		
		$q_{ecal}(mg/g)$	$k_1(1/min)$	R^2	$q_{ecal}(mg/g)$	$k_2 * 10^{-2}(g/mgmin)$	R^2
50	95.6	95.6	4.48	0.99	95.7	83.5	1.00
100	195.3	194.3	1.14	0.99	197.3	1.25	0.99
150	294.2	283.7	0.54	0.88	292.3	0.32	0.96
200	379.1	349.5	0.25	0.79	367.7	0.10	0.95
250	505.7	455.4	0.07	0.75	480.4	0.03	0.94
300	570.8	517.7	0.04	0.88	563.6	0.01	0.93

The higher coefficient of correlation (R^2) values is observed for the pseudo-second-order over pseudo-first-order. Furthermore, the calculated q_e values ($q_{e,cal}$) from the pseudo-second-order kinetic model were closer to the experimental q_e values ($q_{e,exp}$) compared to the first-order model. These kinetic data clearly reveal that the adsorption of RBBR by Cs-Bz/ZnO-25/ Fe_3O_4 was well described by pseudo-second-order kinetic model, which indicates the tendency towards chemisorption process^[166].

3.3.5 Adsorption isotherm

The determination of the adsorption isotherm is an essential fact to understand the mode of the adsorption process between adsorbent and adsorbate. Therefore, three isotherm models namely Langmuir^[122], Freundlich^[123], and Temkin^[124] were applied for fitting the empirical data of uptaking RBBR by Cs-Bz/ZnO-25/ Fe_3O_4 . The nonlinear (expressions: 3.19, 3.20, 3.21) for these isotherm models can be expressed as follow:

$$q_t = \frac{q_{max}K_aC_e}{1 + K_aC_e} \quad (3.19)$$

$$q_e = K_fC_e^{1/n} \quad (3.20)$$

$$q_t = \frac{RT}{b_T} \ln K_aC_e \quad (3.21)$$

In the above expressions, $q_e(mg/g)$ is the adsorption capacity, $q_{max}(mg/g)$ the maximum adsorption capacity, K_a , K_f , and K_T are constants (L/mg) of Langmuir, Freundlich, and Temkin, respectively, n is a parameter that describes the type of adsorptions, $b_T(J/mol)$ is the heat of adsorption. The calculate isotherm parameters for all the studied isotherm models are represented in ([Table: 3.14](#)) and ([Table: 3.25](#)).

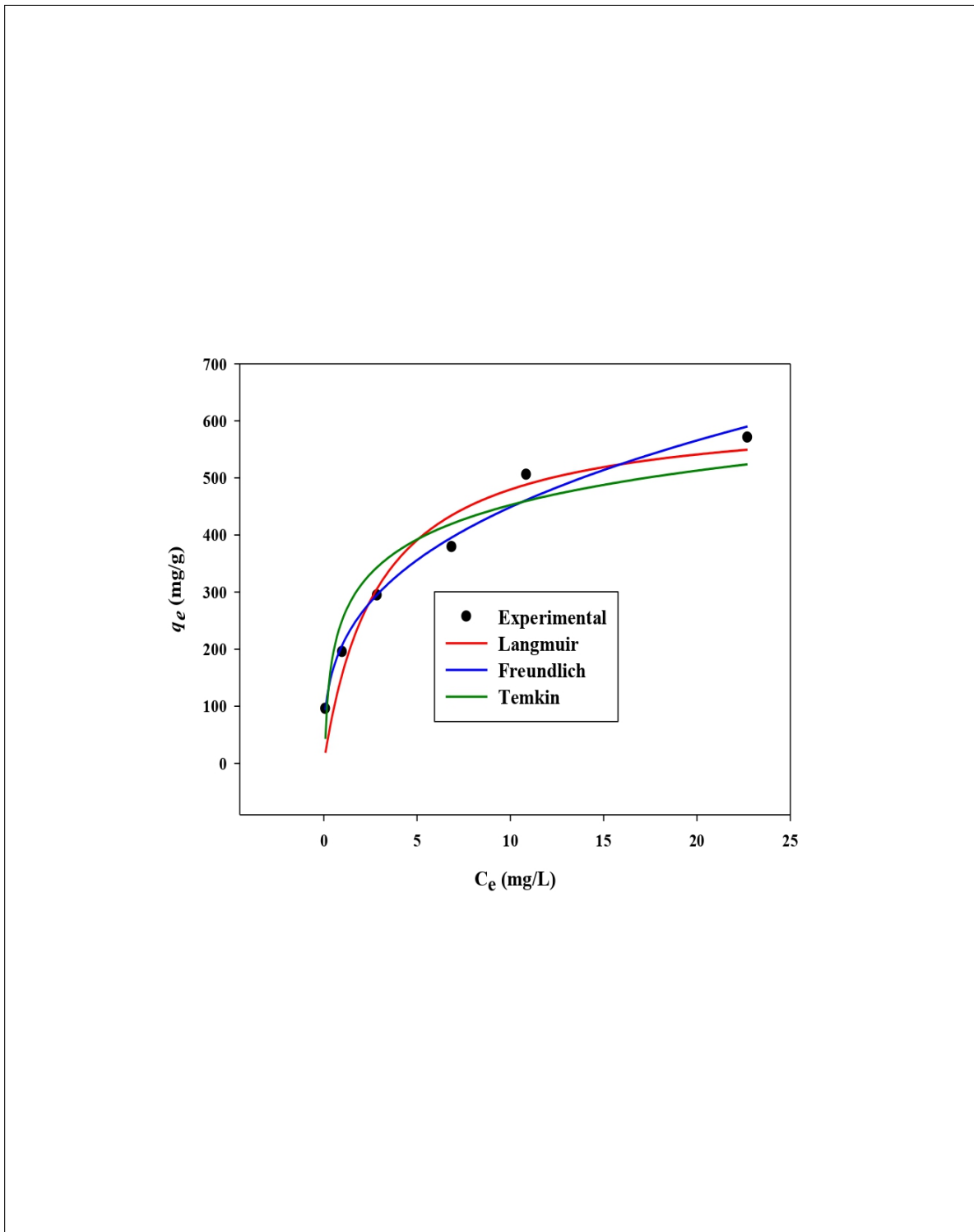


Figure 3.25: Adsorption isotherms of RBBR dye by Cs-Bz/ZnO-25/ Fe_3O_4 . Experimental conditions (dose = 0.04 g, pH = 4, temperature = 60 °C, agitation speed = 100 strokes, and volume of solution = 100 mL).

According to (Table: 3.14), the uptake of RBBR dye by Cs-Bz/ZnO-25/ Fe_3O_4 obeys Freundlich isotherm model, and is better than the Langmuir and Temkin adsorption isotherm models due to its higher coefficient of determination ($R^2 = 0.98$) value compared to the other

Table 3.14: Parameters of isotherm models for RBBR adsorption by Cs-Bz/ZnO-25/ Fe_3O_4 at 60 °C

Adsorption isotherm	Parameter	Value
Langmuir	qm (mg/g)	620.5
	Ka (L/mg)	0.340
	R^2	0.93
Freundlich	Kf (mg/g) (L/mg) ^{1/n}	208.1
	N	2.99
	R^2	0.98
Temkin	KT (L/mg)	2.89
	bT (J/mol)	31.8
	R^2	0.91

models. This finding suggests that the adsorption was occurred on heterogeneous surfaces by multilayer coverage^[167]. Moreover, the maximum adsorption capacity q_{max} was estimated by the Langmuir isotherm model to be 620.5 mg/g. Thus, the q_{max} of RBBR dye onto Cs-Bz/ZnO-25/ Fe_3O_4 was compared with other adsorbents reported in the literature for removing RBBR as listed in (Table: 3.15). This (Table: 3.15), reveals that Cs-Bz/ZnO-25/ Fe_3O_4 is a promising magnetic composite material for removal of an anionic dye (RBBR) from aqueous environment with very preferable adsorption capacity.

Table 3.15: Comparison of the q_{max} of RBBR dye by different adsorbents.

Adsorbents	q_m (mg/g)	References
Cs-Bz/ZnO-25/ Fe_3O_4	620.5	This study
Chitosan-tripolyphosphate/kaolin composite	687.2	[148]
Graphene oxide-ionic liquid	416.7	[149]
Sawdust-based activated carbon	368.5	[150]
Polyaniline/chitosan composite	303.03	[128]
ZnO-polyacrylonitrile-hinokitiol	267.37	[130]
Chitosan-alkali lignin composite	111.11	[133]
Chitosan/SiO ₂ /carbon nanotubes magnetic nanocomposite	97.08	[134]
Magnesium hydroxide coated bentonite	66.90	[151]
Borax cross-linked Jhingan gum hydrogel	9.884	[136]

3.3.6 Adsorption thermodynamics

The spontaneity of the adsorption process was determined by determining the thermodynamic functions at different working temperatures. The standard change for Gibb's free energy ΔG° (kJ/mol), and enthalpy ΔH° (kJ/mol), and entropy ΔS° (kJ/mol K) were calculated using the following (equations 3.22, 3.23, 3.24) respectively^[145]:

$$\Delta G = -RT \ln K_d \quad (3.22)$$

$$K_d = \frac{q_e}{C_e} \quad (3.23)$$

$$\ln K_d = \frac{\Delta S}{R} - \frac{\Delta H}{RT} \quad (3.24)$$

The obtained values of ΔG , ΔS , and ΔH are listed in ([Table: 3.16](#)), and the corresponding Van't Hoff plot deduced by plotting $\ln K_d$ as a function of $1/T$ is presented in ([Figure: 3.26](#)).

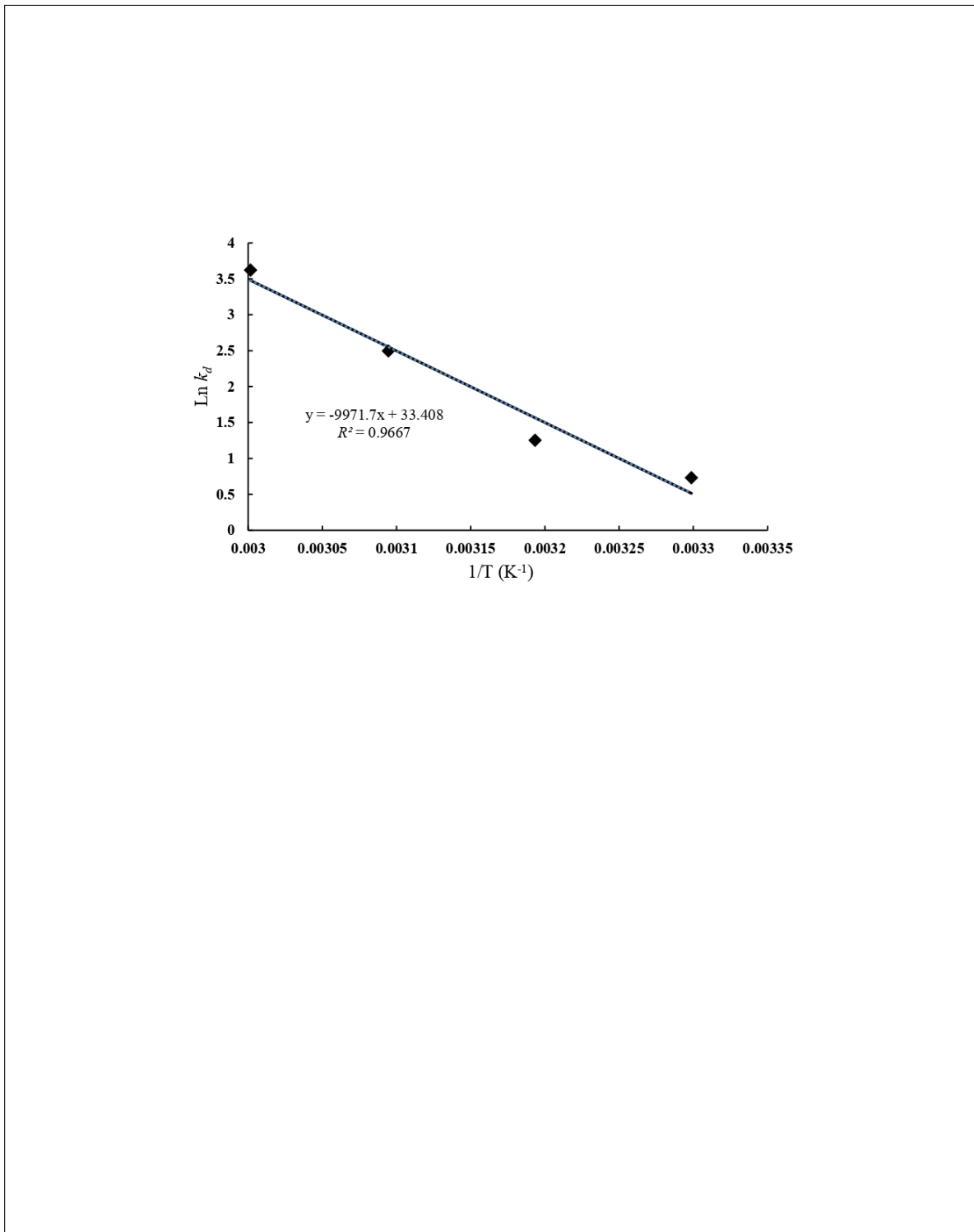


Figure 3.26: Van't Hoff plot RBBR dye adsorption by Cs-Bz/ZnO-25/ Fe_3O_4 (dose=0.04 g, pH= 4, agitation speed = 100 strokes, and vol.= 100 mL).

Table 3.16: Thermodynamic parameters for the adsorption of RBBR dye on Cs-Bz/ZnO-25/ Fe_3O_4

T (K)	K_d	ΔG° (kJ/mol)	ΔH° (kJ/mol)	ΔS° (kJ/molK)
303.15	2.08	-1.84	82.9	0.28
313.15	3.50	-3.26		
323.15	12.2	-6.71		
333.15	37.4	-10.03		

In general, the negative values of ΔG° at all working temperatures confirm the spontaneity of the RBBR adsorption by Cs-Bz/ZnO-25/ Fe_3O_4 ^[168]. The positive value of the ΔH° indicates that the adsorption process of RBBR by Cs-Bz/ZnO-25/ Fe_3O_4 is an endothermic in nature. This observation is in line with the results of BBD parametric optimization presented in ([Figure: 3.23](#)). Furthermore, the positive value of ΔS° indicate possible increment in the degree of freedom of the adsorbed species due to RBBR disorder and/or loss of water molecules upon binding of RBBR to the Cs-Bz/ZnO-25/ Fe_3O_4 surface.

3.3.7 Adsorption mechanism

The prepared Cs-Bz/ZnO/ Fe_3O_4 nanocomposite with various active adsorption sites on its molecular structure as proven previously by various analytical techniques can offer several interaction forces (e.g., electrostatic attractions, hydrogen bonding, Yoshida H-bonding, n-interactions, and - interactions) with the RBBR molecules as shown in ([Figure: 3.27](#)). One of the decisive interactions in the adsorption of the RBBR dye is an electrostatic attraction because of the abundance of positive functional groups (e.g., $-NH_3^+$, $-OH_2^+$, and $C = HN^+$ and charges $Zn(OH)^+$ on the surface of Cs-Bz/ZnO/ Fe_3O_4 , which can strongly attract the negative charges ($-SO_3^-$) of the RBBR molecules^[153]. The possible hydrogen interactions can be occurred between the free hydrogen atom in the Cs-Bz/ZnO/ Fe_3O_4 surface with N and O atoms in the molecular structure of RBBR. Yoshida hydrogen bonding occurs between the OH (-H of hydroxyl group) groups of adsorbent (Cs-Bz/ZnO/ Fe_3O_4) and the aromatic rings of adsorbate (RBBR dye) and this correlates well with the observations^[169], ^[170], ^[101]. Another possible interaction is n which can be created between lone pair electrons of the O and N atoms in the molecular structure of RBBR with the aromatic rings of cross-linker agent (Bz). Moreover, interaction also can be occurred between the aromatic rings of Bz with

the orbital of the aromatic rings in the molecular structure of RBBR^[171]. These types of various possible interactions lead to a very distinct improvement in the adsorption capacity of Cs-Bz/ZnO/ Fe_3O_4 towards RBBR, with preferable adsorption capacity of 620.5 mg/g.

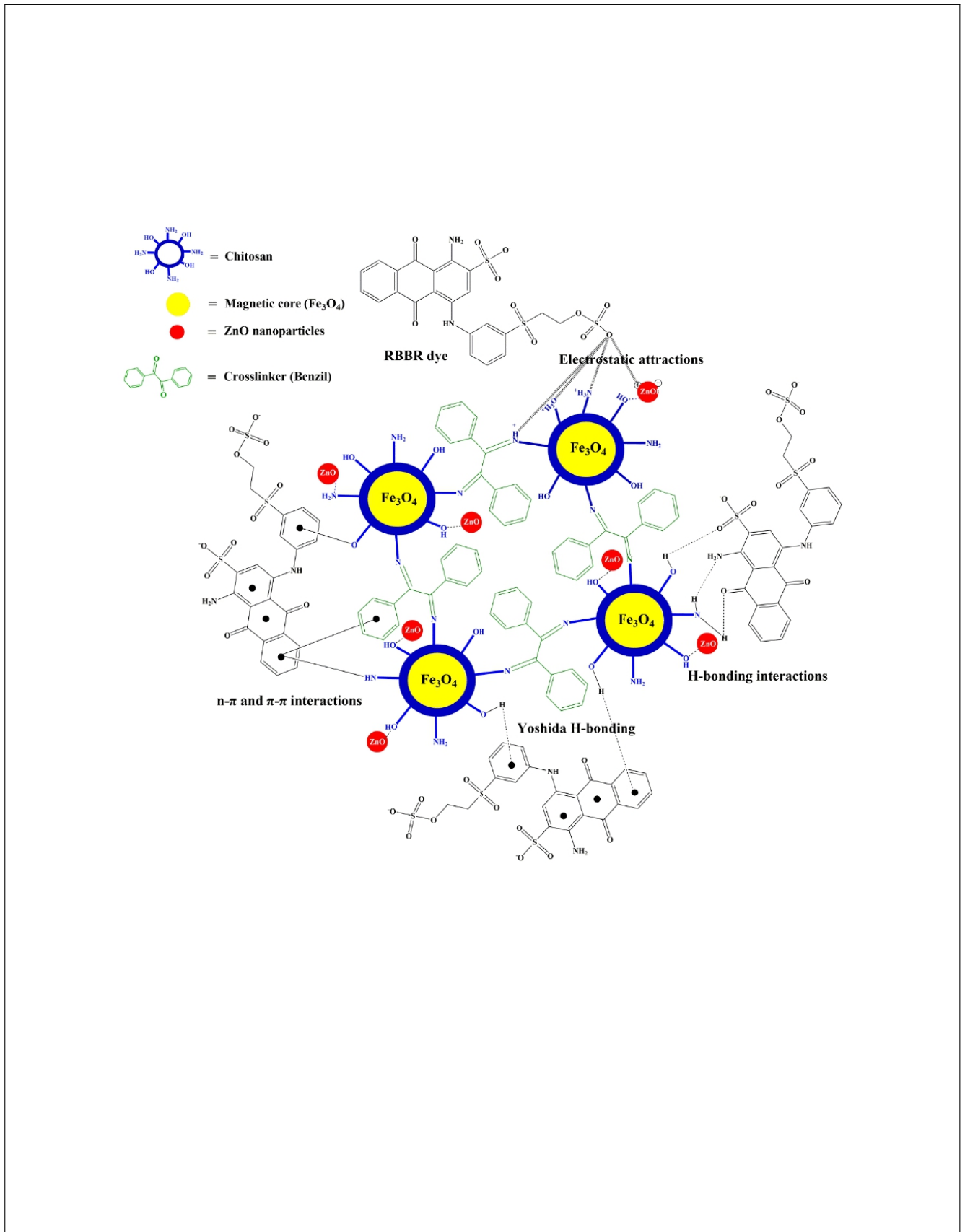


Figure 3.27: Adsorption mechanism of RBBR dye on the Cs-Bz/ZnO/Fe₃O₄ surface.

GENERAL CONCLUSION

In general, this study was conducted to assess the effectiveness of bio-composites that have the Schiff's base functions and the potential of using them for uptaking the dyes pollutants from Waterbodies In order to contribute to the preservation of ecosystems. Three bio-composites have been successfully synthesized as promising adsorbents for the removal of the RBBR dye from wastewater, and characterized by several analysis techniques to confirm their chemical structure. Regarding the comparative studies and optimizing the influence of conditions and parameters on the adsorption process were estimated through modeling Stat-Ease Design-Expert (Version 12) software. This research also achieved the desired goals, which are as follows:

Objective 1: Chitosan-magnetic were synthesized followed by cross-linking reaction with three different kind of cross-linking agents namely: glyoxal, glutaraldehyde, and benzil in order to obtain at composites carry bi-imines function. Beside, Nano ZnO powder was dispersed into chitosan matrix at two different mixing ratios 25% and 50% to improve the surface area of the adsorbents. Thus, the bio-composites obtained as such: CS-G/ZnO/ Fe_3O_4 , CHT-GLA/ZnO/ Fe_3O_4 , and Cs-Bz/ZnO/ Fe_3O_4 .

Objective 2: The bio-composites have been above mentioned were characterized by several analyse techniques for instance SEM/EDX, FTIR, XRD, BET, and pH potentiometric titration analyses to confirm physical properties and the chemical structure. In this regard, the obtained results showed that the highest RBBR removal efficiency by CS-G/ZnO/ Fe_3O_4 , CHT-GLA/ZnO/ Fe_3O_4 , and Cs-Bz/ZnO/ Fe_3O_4 was 93.8%, 75.8%, and 98.9% respectively.

Objective 3: The adsorption isotherm and kinetic models studies were applied to monitor the behavior of adsorption process. It can be deduced from the found values that all adsorbents obey the Freundlich isotherm model given that it more fit this study and the closeness of the R2 value to 1. The maximum adsorption capacity of CS-G/ZnO/ Fe_3O_4 , CHT-GLA/ZnO/ Fe_3O_4 , and Cs-Bz/ZnO/ Fe_3O_4 was 363.3, 176.6, and 620.5 respectively. In his regard, as followed adsorption kinetic study for this research pseudo second order rate constant Owing to the q_e experimental close to q_e calculated.

Future Recommendations

Based on the results from this study the following recommendations be carried out for any future work as continuation:

- response surface methodology is considered very important to optimize adsorption process factors.
- The crosslinkers used in the current study can be replaced with crosslinkers from kind conjugated system.
- Use these obtained biocomposites for uptaking heavy metal in wastewater treatment.



Contents lists available at ScienceDirect

Journal of Environmental Chemical Engineering

journal homepage: www.elsevier.com/locate/jece

Parametric optimization by Box–Behnken design for synthesis of magnetic chitosan-benzil/ZnO/Fe₃O₄ nanocomposite and textile dye removal

Abdallah Reghioua^{a,b,c}, Djamel Barkat^a, Ali H. Jawad^{b,*}, Ahmed Saud Abdulhameed^d, Abdullah A. Al-Kahtani^e, Zeid A. AlOthman^e

^a Laboratory of Molecular Chemistry and Environment, University of Biskra, PO Box 1-65, Biskra, 07000, Algeria

^b Faculty of Applied Sciences, Universiti Teknologi MARA, 40450 Shah Alam, Selangor, Malaysia

^c University of El Oued, Psc. Technology, 39000 El Oued, Algeria

^d Department of Medical Instrumentation Engineering, Al-Mustansiriyah University College, Baghdad, Iraq

^e Advanced Materials Research Chair, Chemistry Department, College of Science, King Saud University, Riyadh 11451, Saudi Arabia

ARTICLE INFO

Editor: Dr. G.L. Dotto

Keywords:

Schiff's base

Chitosan

ZnO nanoparticles

Box-Behnken

Response surface methodology

Adsorption

ABSTRACT

In this research work, a new magnetic Schiff's base-chitosan-benzil/zinc oxide/Fe₃O₄ nanocomposite (Ca-Sb/ZnO/Fe₃O₄) was developed to be a promising and recoverable adsorbent for Remazol Brilliant Blue R dye (RBBR) removal from the aquatic environment. Parametric optimization by Box–Behnken design was made to optimize the synthesis condition (loading ZnO nanoparticles into polymeric matrix of Ca) in addition to adsorption operation parameters (adsorbent dose, solution pH, temperature, and contact time). The obtained results show that the best RBBR removal (96.8%) can be achieved by loading 25% ZnO nanoparticles into polymeric matrix of Ca (Ca-Sb/ZnO-25/Fe₃O₄), and at optimum adsorption operation parameters (adsorbent dosage of 0.04 g, solution of pH 4, temperature of 60 °C, and contact time of 10 min). At these optimum conditions, the maximum adsorption capacity was found to be 620.5 mg/g. The best isotherm and kinetic models were Freundlich model and pseudo-second-order kinetic model, respectively. The probable RBBR dye adsorption mechanism can be assigned to various types of physicochemical interactions (i.e. electrostatic, π-π, π-π interactions) in addition to hydrogen bonding and Yoshida H-bonding. The output of this research confirms that Ca-Sb/ZnO-25/Fe₃O₄ is a superior, recoverable, and environment friendly bi-hybrid nanocomposite adsorbent. The remarkable output of this research can open a window for other possible significant applications such as treatment of real waste water, removal of heavy metal ions, and reduction of chemical oxygen demand.

1. Introduction

Maintaining the freshwater in human life is a crucial issue in our time, particularly with the increasing level of pollutants such as sewage and industrial wastewater, in addition to the exceptional pollution resulting from transportation accidents, which leads to the degradation of many ecosystems [1]. The discharge of industrial pollutants such as dyes can cause many harmful effects on aquatic environments and human beings [2,3]. Thus, it is recommended that these organic dyes to be correctly disposed before being released into aquatic environment to maintain ecosystems [4]. Till now, several techniques have been applied for removing these hazardous pollutants from the water/wastewater e.g., precipitation by chemical agents [5], separation by ion exchange method [6], adsorption process [7], chemical oxidation/reduction [8],

biological treatment [9], and nitrifying-enriched activated sludge (NAS) [10]. Among these methods, adsorption is a very effective technique due to its high selectivity, regeneration, low-cost, and designability [11,12]. These ideal features of adsorption make it one of the most important techniques to confront dangerous environmental threats.

Chitosan (Cs) is composed of D-glucosamine units which is a cationic polysaccharide [13]. Cs is ranked in the second position after cellulose according to its abundance in nature, and it can be produced from deacetylation of chitin [14]. Cs has several significant characteristics e.g non-toxicity, biodegradability, antimicrobial activity, and biocompatibility [15]. It is unique due to the existence of two groups namely hydroxyl (-OH) and amino (-NH₂) in its backbone [16]. These unique functional groups in Cs backbone can be effectively utilized for capturing various types water pollutants such as dyes [17], and metal

* Corresponding author.

E-mail address: al200@uitm.edu.my (A.H. Jawad).

<https://doi.org/10.1016/j.jece.2021.105166>

Received 21 December 2020; Received in revised form 26 January 2021; Accepted 1 February 2021

Available online 5 February 2021

2213-2407/© 2021 Elsevier Ltd. All rights reserved.



Synthesis of Schiff's base magnetic crosslinked chitosan-glyoxal/ZnO/Fe₃O₄ nanoparticles for enhanced adsorption of organic dye: Modeling and mechanism study

Abdallah Reghioia^{a,b,c}, Djamel Barkat^a, Ali H. Jawad^{b,*}, Ahmed Saud Abdulhameed^d,
Mohammad Rizwan Khan^e

^a Laboratory of Molecular Chemistry and Environment, University of Biskra, PO Box 345, Biskra, 07000, Algeria

^b Faculty of Applied Sciences, Universiti Teknologi MARA, 40450 Shah Alam, Selangor, Malaysia

^c University of El Oued, P.O. Technology, 39000 El Oued, Algeria

^d Department of Medical Instrumentation Engineering, Al-Mustansiriyah University College, Baghdad, Iraq

^e Chemistry Department, College of Science, King Saud University, Riyadh 11451, Saudi Arabia

ARTICLE INFO

Keywords

Magnetic chitosan
ZnO nanoparticles
Glyoxal
Adsorption
Optimization
Reactive blue 19 dye

ABSTRACT

In this work, Schiff's base magnetic crosslinked chitosan-glyoxal/Fe₃O₄ composite (CS-G/Fe₃O₄) was synthesized and further developed by loading zinc oxide (ZnO) nanoparticles into its polymeric matrix. The final composite material of magnetic crosslinked chitosan-glyoxal/ZnO/Fe₃O₄ nanoparticles (CS-G/ZnO/Fe₃O₄ NPs) was tested for the removal of organic dye pollutant (reactive blue 19, RB19). The synthesized magnetic nanomaterials were characterized by several techniques such as CHN elemental analysis, Brunauer-Emmett-Teller analysis, vibrating-sample magnetometer, X-ray powder diffraction, Fourier Transform infrared, scanning electron microscope, energy dispersive X-ray analysis, pH_{zpc}, and pH-potentiometric titration. A statistical approach namely Box-Behnken design (BBD) was applied to optimize the synthesis conditions as well as adsorption key parameters (A: ZnO nanoparticles loading (0–50%), B: adsorbent dosage (0.02–0.1 g), C: pH (4–10), D: temperature (30–60 °C), and time E: (10–60 min)). The adsorption kinetic and equilibrium results were well described with pseudo-second order model and Freundlich isotherm model, respectively. The maximum adsorption capacity of CS-G/ZnO/Fe₃O₄ NPs for RB19 was 363.3 mg/g at 60 °C. The adsorption mechanism of RB19 onto CS-G/ZnO/Fe₃O₄ NPs can be ascribed to several types of interactions (e.g. electrostatic attractions, hydrogen bonding, and π-π interactions). This study provides a new and effective adsorbent for water remediation due to its recoverability and high efficiency in removing the organic dye pollutants.

1. Introduction

Liquid wastes discharged from various industries such as textile, food, pharmaceutical, paper, and cosmetic is one of the most important contributors to water pollution around the world (Souza and Velasco, 2020). Treatment of the wastewater containing pollutants is a challenging task that researchers are facing. These wastewaters may contain organic dyes, heavy metals, and pharmaceuticals, which may affect human health, and the quality of aquatic life (Costa et al., 2020). Among the various organic dye pollutants, reactive blue 19 (RB19) dye (also known as remazol brilliant blue R dye) is a toxic anionic dye commonly used as a starting material for synthesis of polymeric dyes (Jawad and

Abdulhameed, 2020a). RB19 is classified as a recalcitrant organo-pollutant, which can cause a series of harms to humans and living organisms (Danda and Eckert, 2020). Thus, it is essential to efficiently remove organic dye pollutants from wastewater before being discharged into aquatic systems. Various biological, chemical, and physical technologies aiming at removing organic dye pollutants from effluents have been applied such as adsorption (Senthil and Alzain, 2020), electrochemical oxidation (Madruga-Rodríguez et al., 2020), photocatalytic degradation (Albus et al., 2020; Ayodele et al., 2021), and ion exchange (Joseph et al., 2020). Among these technologies, adsorption has been extensively researched and applied due to its high efficiency, low operation cost, insensitivity towards toxicity of substances, and

* Corresponding author.

E-mail address: ahj200@uvm.edu.my, ahj200@gmail.com (A.H. Jawad).

<https://doi.org/10.1016/j.scp.2021.100379>

Received 23 October 2020; Received in revised form 15 January 2021; Accepted 16 January 2021

Available online 27 January 2021

2352-5541/© 2021 Elsevier B.V. All rights reserved.



Magnetic Chitosan-Glutaraldehyde/Zinc Oxide/Fe₃O₄ Nanocomposite: Optimization and Adsorptive Mechanism of Remazol Brilliant Blue R Dye Removal

Abdallah Reghioua^{1,2,3} · Djamel Barkat¹ · Ali H. Jawad² · Ahmed Saud Abdulhameed⁴ · S. Rangabhashtyam⁵ · Mohammad Rizwan Khan⁶ · Zaid A. AlOthman⁶

Accepted: 27 April 2021

© The Author(s), under exclusive licence to Springer Science+Business Media, LLC | part of Springer Nature 2021

Abstract

A magnetic Schiff's base chitosan-glutaraldehyde/Fe₃O₄ composite (CHT-GLA/ZnO/Fe₃O₄) was developed by incorporating zinc oxide (ZnO) nanoparticles into its structure to prepare an efficient adsorbent for the removal of remazol brilliant blue R (RBBR) dye. The CHT-GLA/ZnO/Fe₃O₄ was characterized by the following methods: CHN, BET, FTIR, XRD, SEM-EDX, pH_{pzc}, and potentiometric titrations. Box-Behnken design based on response surface methodology was used to optimize the effects of the A: ZnO nanoparticles loading (0–50%), B: dose (0.02–0.1 g), C: pH (4–10), D: temperature (30–60 °C), and time E: (10–60 min) on the synthesis of the magnetic adsorbent and the RBBR dye adsorption. The experimental data of kinetics followed the pseudo-second order model, while isotherms showed better fit to Freundlich and Temkin models. The maximum adsorption capacity of the target nanocomposite (CHT-GLA/Fe₃O₄ containing 25% ZnO or CHT-GLA/ZnO/Fe₃O₄-25) was reached of 176.6 mg/g at 60 °C. The adsorption mechanism of RBBR onto CHT-GLA/ZnO/Fe₃O₄ nanocomposite can be attributed to multi-interactions including electrostatic attractions, hydrogen bonding, Yoshida H-bonding, and π - π interactions. This study offers a promising hybrid nanobiomaterial adsorbent in environmental nanotechnology to separate and remove the contaminants such as organic dyes from wastewater.

Keywords Magnetic chitosan · Zinc oxide nanoparticles · Remazol brilliant blue R dye · Glutaraldehyde · Response surface methodology

Introduction

Synthetic dyes are widely used in many industrial activities including paper, plastics, textile, cosmetic, leather, and pharmaceutical, which generate massive volumes of wastewaters [1]. Discharging of the organic dyes directly into surface water can cause serious water pollution, i.e. reducing photosynthesis activity, disordering the ecological balance of aquatic systems, and toxic effects on biota [2]. Moreover, several dyes can cause a series of adverse effects on human health [3]. Remazol brilliant blue R (RBBR) dye is a typical reactive dye, which is extensively used in the industrial for synthesis of polymeric dyes [4]. RBBR is considered as recalcitrant organic pollutants, which can cause several health problems [5]. Therefore, the treatment of the effluents containing dyestuffs before being fluxed into water streams is environmentally important. Several methods have been documented for the treatment of the effluents containing dyestuffs such as adsorption [6], membrane separation [7],

✉ A.H. Jawad
ah288@uimn.edu.my; ahjn72@gmail.com

¹ Laboratory of Molecular Chemistry and Environment, University of Biskra, PO Box 145, Biskra 07000, Algeria

² Faculty of Applied Sciences, Universiti Teknologi MARA, 40450 Shah Alam, Selangor, Malaysia

³ University of El Oued, Fac. Technology, 30000 El Oued, Algeria

⁴ Department of Medical Instrumentation Engineering, Al-Mansour University College, Baghdad, Iraq

⁵ Department of Biotechnology, School of Chemical and Biotechnology, SASTRA Deemed University, Thanjavur, Tamil Nadu 613401, India

⁶ Advanced Materials Research Chair, Chemistry Department, College of Science, King Saud University, Riyadh 11451, Saudi Arabia

BIBLIOGRAPHY

- [1] M. Pervaiz, S. Sadiq, A. Sadiq, U. Younas, A. Ashraf, Z. Saeed, M. Zuber, and A. Adnan, "Azo-schiff base derivatives of transition metal complexes as antimicrobial agents."
- [2] S. Sadjadi, N. Abedian-Dehaghani, F. Koohestani, and M. M. Heravi, "Halloysite functionalized with cu (ii) schiff base complex containing polymer as an efficient catalyst for chemical transformation," *Inorganic Chemistry Communications*, vol. 133, p. 108955, 2021.
- [3] B. Naureen, G. Miana, K. Shahid, M. Asghar, S. Tanveer, and A. Sarwar, "Iron (iii) and zinc (ii) monodentate schiff base metal complexes: Synthesis, characterisation and biological activities," *Journal of Molecular Structure*, vol. 1231, p. 129946, 2021.
- [4] T. Bazhenova, L. Zorina, S. Simonov, Y. V. Manakin, A. Kornev, K. Lyssenko, V. Mironov, I. Gilmutdinov, and E. Yagubskii, "A novel family of hepta-coordinated cr (iii) complexes with a planar pentadentate n3o2 schiff base ligand: Synthesis, structure and magnetism," *Inorganica Chimica Acta*, vol. 522, p. 120358, 2021.
- [5] H. Kargar, M. Fallah-Mehrjardi, R. Behjatmanesh-Ardakani, K. Munawar, M. Ashfaq, and M. Tahir, "Titanium (iv) complex containing ono-tridentate schiff base ligand: Synthesis, crystal structure determination, hirshfeld surface analysis, spectral characterization, theoretical and computational studies," *Journal of Molecular Structure*, vol. 1241, p. 130653, 2021.
- [6] Y. Song, C. Li, G. Liu, R. Liu, Y. Chen, W. Li, Z. Cao, B. Zhao, C. Lu, and Y. Liu, "Drug-metabolizing cytochrome p450 enzymes have multifarious influences on treatment outcomes," *Clinical pharmacokinetics*, pp. 1–17, 2021.

-
- [7] T. A. Saleh, "Protocols for synthesis of nanomaterials, polymers, and green materials as adsorbents for water treatment technologies," *Environmental Technology & Innovation*, p. 101821, 2021.
- [8] G. Xiao, H. Su, and T. Tan, "Synthesis of core-shell bioaffinity chitosan-tio₂ composite and its environmental applications," *Journal of Hazardous Materials*, vol. 283, pp. 888–896, 2015.
- [9] M. Nasrollahzadeh, M. Sajjadi, S. Iravani, and R. S. Varma, "Carbon-based sustainable nanomaterials for water treatment: state-of-art and future perspectives," *Chemosphere*, vol. 263, p. 128005, 2021.
- [10] N. N. Abd Malek, A. H. Jawad, K. Ismail, R. Razuan, and Z. A. ALothman, "Fly ash modified magnetic chitosan-polyvinyl alcohol blend for reactive orange 16 dye removal: Adsorption parametric optimization," *International journal of biological macromolecules*, vol. 189, pp. 464–476, 2021.
- [11] H. Chandarana, S. Subburaj, P. S. Kumar, and M. A. Kumar, "Evaluation of phase transfer kinetics and thermodynamic equilibria of reactive orange 16 sorption onto chemically improved arachis hypogaea pod powder," *Chemosphere*, vol. 276, p. 130136, 2021.
- [12] I. A. Mohammed, A. H. Jawad, A. S. Abdulhameed, and M. S. Mastuli, "Physicochemical modification of chitosan with fly ash and tripolyphosphate for removal of reactive red 120 dye: statistical optimization and mechanism study," *International journal of biological macromolecules*, vol. 161, pp. 503–513, 2020.
- [13] R. Abd Rashid, M. A. M. Ishak, and K. Mohammed, "Adsorptive removal of methylene blue by commercial coconut shell activated carbon," *Science Letters*, vol. 12, no. 1, 2018.
- [14] A. Reghioua, D. Barkat, A. H. Jawad, A. S. Abdulhameed, A. A. Al-Kahtani, and Z. A. ALothman, "Parametric optimization by box-behnken design for synthesis of magnetic chitosan-benzil/zno/fe₃o₄ nanocomposite and textile dye removal," *Journal of Environmental Chemical Engineering*, vol. 9, no. 3, p. 105166, 2021.
- [15] X. Zou, H. Zhang, T. Chen, H. Li, C. Meng, Y. Xia, and J. Guo, "Preparation and characterization of polyacrylamide/sodium alginate microspheres and its adsorption of mb dye," *Colloids and Surfaces A: Physicochemical and Engineering Aspects*, vol. 567, pp. 184–192, 2019.

-
- [16] H. Demissie, G. An, R. Jiao, T. Ritigala, S. Lu, and D. Wang, "Modification of high content nanocluster-based coagulation for rapid removal of dye from water and the mechanism," *Separation and Purification Technology*, vol. 259, p. 117845, 2021.
- [17] S. M. Saleh, "Zno nanospheres based simple hydrothermal route for photocatalytic degradation of azo dye," *Spectrochimica Acta Part A: Molecular and Biomolecular Spectroscopy*, vol. 211, pp. 141–147, 2019.
- [18] C. Anushree and J. Philip, "Efficient removal of methylene blue dye using cellulose capped fe₃o₄ nanofluids prepared using oxidation-precipitation method," *Colloids and Surfaces A: Physicochemical and Engineering Aspects*, vol. 567, pp. 193–204, 2019.
- [19] P. Liang, M. Rivallin, S. Cerneaux, S. Lacour, E. Petit, and M. Cretin, "Coupling cathodic electro-fenton reaction to membrane filtration for ao7 dye degradation: A successful feasibility study," *Journal of Membrane Science*, vol. 510, pp. 182–190, 2016.
- [20] P. Chanikya, P. Nidheesh, D. S. Babu, A. Gopinath, and M. S. Kumar, "Treatment of dyeing wastewater by combined sulfate radical based electrochemical advanced oxidation and electrocoagulation processes," *Separation and Purification Technology*, vol. 254, p. 117570, 2021.
- [21] H. Pakalapati, P. L. Show, J.-H. Chang, B.-L. Liu, and Y.-K. Chang, "Removal of dye waste by weak cation-exchange nanofiber membrane immobilized with waste egg white proteins," *International journal of biological macromolecules*, vol. 165, pp. 2494–2507, 2020.
- [22] M. E. Mahmoud, G. M. Nabil, N. M. El-Mallah, H. I. Bassiouny, S. Kumar, and T. M. Abdel-Fattah, "Kinetics, isotherm, and thermodynamic studies of the adsorption of reactive red 195 a dye from water by modified switchgrass biochar adsorbent," *Journal of Industrial and Engineering Chemistry*, vol. 37, pp. 156–167, 2016.
- [23] Z. Graba, S. Hamoudi, D. Bekka, N. Bezzi, and R. Boukherroub, "Influence of adsorption parameters of basic red dye 46 by the rough and treated algerian natural phosphates," *Journal of Industrial and Engineering Chemistry*, vol. 25, pp. 229–238, 2015.
- [24] W. Du, X. Wang, G. Chen, J. Zhang, and M. Slaný, "Synthesis, property and mechanism analysis of a novel polyhydroxy organic amine shale hydration inhibitor," *Minerals*, vol. 10, no. 2, p. 128, 2020.

-
- [25] A. M. Awad, R. Jalab, A. Benamor, M. S. Nasser, M. M. Ba-Abbad, M. El-Naas, and A. W. Mohammad, "Adsorption of organic pollutants by nanomaterial-based adsorbents: An overview," *Journal of Molecular Liquids*, vol. 301, p. 112335, 2020.
- [26] K. B. Tan, M. Vakili, B. A. Horri, P. E. Poh, A. Z. Abdullah, and B. Salamatinia, "Adsorption of dyes by nanomaterials: recent developments and adsorption mechanisms," *Separation and Purification Technology*, vol. 150, pp. 229–242, 2015.
- [27] F. Pozzi, "Development of innovative analytical procedures for the identification of organic colorants of interest in art and archaeology," 2012.
- [28] J. Sokolowska-Gajda, H. S. Freeman, and A. Reife, "Synthetic dyes based on environmental considerations. part 2: Iron complexes formazan dyes," *Dyes and pigments*, vol. 30, no. 1, pp. 1–20, 1996.
- [29] A. Mudhoo and D. Beekaroo, "Adsorption of reactive red 158 dye by chemically treated cocos nucifera l. shell powder," in *Adsorption of Reactive Red 158 Dye by Chemically Treated Cocos Nucifera L. Shell Powder*. Springer, 2011, pp. 1–65.
- [30] I. Kabdađli, O. Tünay, and D. Orhon, "Wastewater control and management in a leather tanning district," *Water science and technology*, vol. 40, no. 1, pp. 261–267, 1999.
- [31] K. Ivanov, E. Gruber, W. Schempp, and D. Kirov, "Possibilities of using zeolite as filler and carrier for dyestuffs in paper," *Papier*, vol. 50, no. 7-8, p. 456, 1996.
- [32] N. Bensalah, M. Q. Alfaro, and C. Martínez-Huitle, "Electrochemical treatment of synthetic wastewaters containing alphazurine a dye," *Chemical Engineering Journal*, vol. 149, no. 1-3, pp. 348–352, 2009.
- [33] A. Oussalah, A. Boukerroui, A. Aichour, and B. Djellouli, "Cationic and anionic dyes removal by low-cost hybrid alginate/natural bentonite composite beads: adsorption and reusability studies," *International journal of biological macromolecules*, vol. 124, pp. 854–862, 2019.
- [34] Y. Zhou, J. Lu, Y. Zhou, and Y. Liu, "Recent advances for dyes removal using novel adsorbents: a review," *Environmental pollution*, vol. 252, pp. 352–365, 2019.
- [35] S. S. Affat, "Classifications, advantages, disadvantages, toxicity effects of natural and synthetic dyes: A review," *University of Thi-Qar Journal of Science*, vol. 8, no. 1, pp. 130–135, 2021.

-
- [36] E. Clarke and R. Anliker, "Organic dyes and pigments," in *Anthropogenic compounds*. Springer, 1980, pp. 181–215.
- [37] G. Mishra and M. Tripathy, "A critical review of the treatments for decolourization of textile effluent," *Colourage*, vol. 40, pp. 35–35, 1993.
- [38] M. Purkait, S. DasGupta, and S. De, "Adsorption of eosin dye on activated carbon and its surfactant based desorption," *Journal of environmental management*, vol. 76, no. 2, pp. 135–142, 2005.
- [39] Z. Isik, M. Saleh, Z. Bilici, and N. Dizge, "Remazol brilliant blue r (rbbr) dye and phosphate adsorption by calcium alginate beads modified with polyethyleneimine," *Water Environment Research*, 2021.
- [40] A. H. Jawad and A. S. Abdulhameed, "Statistical modeling of methylene blue dye adsorption by high surface area mesoporous activated carbon from bamboo chip using koh-assisted thermal activation," *Energy, Ecology and Environment*, vol. 5, no. 6, pp. 456–469, 2020.
- [41] K. T. Rainert, H. C. A. Nunes, M. J. Gonçalves, C. V. Helm, and L. B. B. Tavares, "Decolorization of the synthetic dye remazol brilliant blue reactive (rbbr) by ganoderma lucidum on bio-adsorbent of the solid bleached sulfate paperboard coated with polyethylene terephthalate," *Journal of Environmental Chemical Engineering*, vol. 9, no. 2, p. 104990, 2021.
- [42] I. M. Banat, P. Nigam, D. Singh, and R. Marchant, "Microbial decolorization of textile-dyecontaining effluents: a review," *Bioresource technology*, vol. 58, no. 3, pp. 217–227, 1996.
- [43] A. K. Mittal and S. Gupta, "Biosorption of cationic dyes by dead macro fungus fomitopsis carnea: batch studies," *Water science and technology*, vol. 34, no. 10, pp. 81–87, 1996.
- [44] Y. Fu and T. Viraraghavan, "Fungal decolorization of dye wastewaters: a review," *Bioresource technology*, vol. 79, no. 3, pp. 251–262, 2001.
- [45] H. Chu and K. Chen, "Reuse of activated sludge biomass: I. removal of basic dyes from wastewater by biomass," *Process Biochemistry*, vol. 37, no. 6, pp. 595–600, 2002.
- [46] Y. Fu and T. Viraraghavan, "Removal of congo red from an aqueous solution by fungus aspergillus niger," *Advances in Environmental Research*, vol. 7, no. 1, pp. 239–247, 2002.

-
- [47] G. Gupta, G. Prasad, and V. Singh, "Removal of chrome dye from aqueous solutions by mixed adsorbents: fly ash and coal," *Water Research*, vol. 24, no. 1, pp. 45–50, 1990.
- [48] K. Kadirvelu, M. Kavipriya, C. Karthika, M. Radhika, N. Vennilamani, and S. Patabhi, "Utilization of various agricultural wastes for activated carbon preparation and application for the removal of dyes and metal ions from aqueous solutions," *Bioresource technology*, vol. 87, no. 1, pp. 129–132, 2003.
- [49] T. Robinson, G. McMullan, R. Marchant, and P. Nigam, "Remediation of dyes in textile effluent: a critical review on current treatment technologies with a proposed alternative," *Bioresource technology*, vol. 77, no. 3, pp. 247–255, 2001.
- [50] M. Asgher and H. N. Bhatti, "Evaluation of thermodynamics and effect of chemical treatments on sorption potential of citrus waste biomass for removal of anionic dyes from aqueous solutions."
- [51] O. G. Oluwole, "Removal of textile dyes from aqueous solutions using clay minerals and agricultural waste (carica papaya seeds)," 2020.
- [52] V. Gupta *et al.*, "Application of low-cost adsorbents for dye removal—a review," *Journal of environmental management*, vol. 90, no. 8, pp. 2313–2342, 2009.
- [53] R. S. Dassanayake, S. Acharya, and N. Abidi, "Recent advances in biopolymer-based dye removal technologies," *Molecules*, vol. 26, no. 15, p. 4697, 2021.
- [54] A. Dąbrowski, "Adsorption from theory to practice," *Advances in colloid and interface science*, vol. 93, no. 1-3, pp. 135–224, 2001.
- [55] M. T. Yagub, T. K. Sen, S. Afroze, and H. M. Ang, "Dye and its removal from aqueous solution by adsorption: a review," *Advances in colloid and interface science*, vol. 209, pp. 172–184, 2014.
- [56] A. Leonard and R. Lauwerys, "Carcinogenicity and mutagenicity of chromium," *Mutation Research/Reviews in Genetic Toxicology*, vol. 76, no. 3, pp. 227–239, 1980.
- [57] T. Mancuso, "Consideration of chromium as an industrial carcinogen," in *International conference on heavy metals in the environment*. University of Toronto, Institute of Environmental Studies Toronto, Canada, 1975, pp. 343–356.

-
- [58] J. C. Pashin, "Coal as a petroleum source rock and reservoir rock," in *Applied coal petrology*. Elsevier, 2008, pp. 227–262.
- [59] A. Ahmad, S. H. Mohd-Setapar, C. S. Chuong, A. Khatoon, W. A. Wani, R. Kumar, and M. Rafatullah, "Recent advances in new generation dye removal technologies: novel search for approaches to reprocess wastewater," *RSC advances*, vol. 5, no. 39, pp. 30 801–30 818, 2015.
- [60] Y. Bulut and H. Aydın, "A kinetics and thermodynamics study of methylene blue adsorption on wheat shells," *Desalination*, vol. 194, no. 1-3, pp. 259–267, 2006.
- [61] M. E. Argun, S. Dursun, M. Karatas, and M. Gürü, "Activation of pine cone using fenton oxidation for cd (ii) and pb (ii) removal," *Bioresource technology*, vol. 99, no. 18, pp. 8691–8698, 2008.
- [62] M. A. M. Salleh, D. K. Mahmoud, W. A. W. A. Karim, and A. Idris, "Cationic and anionic dye adsorption by agricultural solid wastes: a comprehensive review," *Desalination*, vol. 280, no. 1-3, pp. 1–13, 2011.
- [63] B. Nandi, A. Goswami, and M. Purkait, "Removal of cationic dyes from aqueous solutions by kaolin: kinetic and equilibrium studies," *Applied Clay Science*, vol. 42, no. 3-4, pp. 583–590, 2009.
- [64] A. Aadil, M. Shahzad, S. Kashif, M. Muhammad, A. Rabia, A. Saba *et al.*, "Comparative study of adsorptive removal of congo red and brilliant green dyes from water using peanut shell." *Middle East Journal of Scientific Research*, vol. 11, no. 6, pp. 828–832, 2012.
- [65] W. W. Ngah, L. Teong, and M. M. Hanafiah, "Adsorption of dyes and heavy metal ions by chitosan composites: A review," *Carbohydrate polymers*, vol. 83, no. 4, pp. 1446–1456, 2011.
- [66] I. M. Lipatova, L. I. Makarova, and A. A. Yusova, "Adsorption removal of anionic dyes from aqueous solutions by chitosan nanoparticles deposited on the fibrous carrier," *Chemosphere*, vol. 212, pp. 1155–1162, 2018.
- [67] X. Wei, T. Huang, J. Nie, J.-h. Yang, X.-d. Qi, Z.-w. Zhou, and Y. Wang, "Bio-inspired functionalization of microcrystalline cellulose aerogel with high adsorption performance toward dyes," *Carbohydrate polymers*, vol. 198, pp. 546–555, 2018.

-
- [68] I. Bouzaida and M. Rammah, “Adsorption of acid dyes on treated cotton in a continuous system,” *Materials Science and Engineering: C*, vol. 21, no. 1-2, pp. 151–155, 2002.
- [69] D. Sun, X. Zhang, Y. Wu, and X. Liu, “Adsorption of anionic dyes from aqueous solution on fly ash,” *Journal of hazardous materials*, vol. 181, no. 1-3, pp. 335–342, 2010.
- [70] A. Kausar, M. Iqbal, A. Javed, K. Aftab, H. N. Bhatti, S. Nouren *et al.*, “Dyes adsorption using clay and modified clay: a review,” *Journal of Molecular Liquids*, vol. 256, pp. 395–407, 2018.
- [71] M. A. Aly-Eldeen, A. A. El-Sayed, D. M. Salem, and G. M. El Zokm, “The uptake of eriochrome black t dye from aqueous solutions utilizing waste activated sludge: Adsorption process optimization using factorial design,” *The Egyptian Journal of Aquatic Research*, vol. 44, no. 3, pp. 179–186, 2018.
- [72] K. Samal, N. Raj, and K. Mohanty, “Saponin extracted waste biomass of sapindus mukorossi for adsorption of methyl violet dye in aqueous system,” *Surfaces and Interfaces*, vol. 14, pp. 166–174, 2019.
- [73] S. Subramani and N. Thinakaran, “Isotherm, kinetic and thermodynamic studies on the adsorption behaviour of textile dyes onto chitosan,” *Process Safety and Environmental Protection*, vol. 106, pp. 1–10, 2017.
- [74] B. Xu, H. Zheng, Y. Wang, Y. An, K. Luo, C. Zhao, and W. Xiang, “Poly (2-acrylamido-2-methylpropane sulfonic acid) grafted magnetic chitosan microspheres: Preparation, characterization and dye adsorption,” *International journal of biological macromolecules*, vol. 112, pp. 648–655, 2018.
- [75] H. Schiff, “The syntheses and characterization of schiff base,” *Ann. Chem. Suppl*, vol. 3, pp. 343–349, 1864.
- [76] —, “Mittheilungen aus dem universitätslaboratorium in pisa: eine neue reihe organischer basen,” *Justus Liebigs Annalen der Chemie*, vol. 131, no. 1, pp. 118–119, 1864.
- [77] I. Bravo, M. Revenga-Parra, F. Pariente, and E. Lorenzo, “Reagent-less and robust biosensor for direct determination of lactate in food samples,” *Sensors*, vol. 17, no. 1, p. 144, 2017.

-
- [78] C. Demitri, V. M. De Benedictis, M. Madaghiele, C. E. Corcione, and A. Maffezzoli, "Nanostructured active chitosan-based films for food packaging applications: Effect of graphene stacks on mechanical properties," *Measurement*, vol. 90, pp. 418–423, 2016.
- [79] M. O'Donnell, "Aldrichim. acta 2001, 34, 3–15.(e) odonnell, mj," *Acc. Chem. Res.*, vol. 37, pp. 506–517, 2004.
- [80] X. Ye, Y. Chen, C. Ling, R. Ding, X. Wang, X. Zhang, and S. Chen, "One-pot synthesis of schiff base compounds via photocatalytic reaction in the coupled system of aromatic alcohols and nitrobenzene using cdin 2 s 4 photocatalyst," *Dalton Transactions*, vol. 47, no. 32, pp. 10915–10924, 2018.
- [81] S.-Y. Ding, J. Gao, Q. Wang, Y. Zhang, W.-G. Song, C.-Y. Su, and W. Wang, "Construction of covalent organic framework for catalysis: Pd/cof-lzu1 in suzuki–miyaura coupling reaction," *Journal of the American Chemical Society*, vol. 133, no. 49, pp. 19816–19822, 2011.
- [82] A. Zeus, R. Ding, and C. Wolf, "Quantitative chirality sensing of amines and amino alcohols via schiff base formation with a stereodynamic uv/cd probe," *Organic & biomolecular chemistry*, vol. 14, no. 6, pp. 1934–1939, 2016.
- [83] O. Wahba, A. M. Hassan, A. Naser, and A. Hanafi, "Preparation and spectroscopic studies of some copper and nickel schiff base complexes and their applications as colouring pigments in protective paints industry," *Egyptian Journal of Chemistry*, vol. 60, no. 1, pp. 25–40, 2017.
- [84] Y. Liu, L. Mao, S. Yang, M. Liu, H. Huang, Y. Wen, F. Deng, Y. Li, X. Zhang, and Y. Wei, "Synthesis and biological imaging of fluorescent polymeric nanoparticles with aie feature via the combination of raft polymerization and post-polymerization modification," *Dyes and Pigments*, vol. 158, pp. 79–87, 2018.
- [85] D. ŞENOL, "Elektron salıcı ve electron çekici grup içeren schiff bazı polimer boyaların sentez ve karakterizasyonu," *Hacettepe Journal of Biology and Chemistry*, vol. 45, no. 1, pp. 67–80.
- [86] H.-W. Ou, K.-H. Lo, W.-T. Du, W.-Y. Lu, W.-J. Chuang, B.-H. Huang, H.-Y. Chen, and C.-C. Lin, "Synthesis of sodium complexes supported with nno-tridentate schiff base ligands and their applications in the ring-opening polymerization of l-lactide," *Inorganic chemistry*, vol. 55, no. 4, pp. 1423–1432, 2016.

-
- [87] W. Al Zoubi and Y. G. Ko, "Organometallic complexes of schiff bases: recent progress in oxidation catalysis," *Journal of Organometallic Chemistry*, vol. 822, pp. 173–188, 2016.
- [88] A.-T. Mohammad, A. S. Abdulhameed, and A. H. Jawad, "Box-behnken design to optimize the synthesis of new crosslinked chitosan-glyoxal/tio₂ nanocomposite: methyl orange adsorption and mechanism studies," *International journal of biological macromolecules*, vol. 129, pp. 98–109, 2019.
- [89] E. Avcu, F. E. Bařtan, H. Z. Abdullah, M. A. U. Rehman, Y. Y. Avcu, and A. R. Boccacini, "Electrophoretic deposition of chitosan-based composite coatings for biomedical applications: A review," *Progress in Materials Science*, vol. 103, pp. 69–108, 2019.
- [90] H. Hassan, A. Salama, A. K. El-Ziaty, and M. El-Sakhawy, "New chitosan/silica/zinc oxide nanocomposite as adsorbent for dye removal," *International journal of biological macromolecules*, vol. 131, pp. 520–526, 2019.
- [91] B. Butola *et al.*, "Recent advances in chitosan polysaccharide and its derivatives in antimicrobial modification of textile materials," *International journal of biological macromolecules*, vol. 121, pp. 905–912, 2019.
- [92] V. Ghormade, E. Pathan, and M. Deshpande, "Can fungi compete with marine sources for chitosan production?" *International journal of biological macromolecules*, vol. 104, pp. 1415–1421, 2017.
- [93] M. Hamdi, R. Nasri, S. Li, and M. Nasri, "Bioactive composite films with chitosan and carotenoproteins extract from blue crab shells: Biological potential and structural, thermal, and mechanical characterization," *Food Hydrocolloids*, vol. 89, pp. 802–812, 2019.
- [94] Z. Shariatinia and A. Mazloom-Jalali, "Chitosan nanocomposite drug delivery systems designed for the ifosfamide anticancer drug using molecular dynamics simulations," *Journal of Molecular Liquids*, vol. 273, pp. 346–367, 2019.
- [95] A. S. Abdulhameed, A. H. Jawad, and A.-T. Mohammad, "Synthesis of chitosan-ethylene glycol diglycidyl ether/tio₂ nanoparticles for adsorption of reactive orange 16 dye using a response surface methodology approach," *Bioresource technology*, vol. 293, p. 122071, 2019.
- [96] N. N. Abd Malek, E. Yousif, and A. H. Jawad, "Optimization of adsorption parameters for

- reactive red 4 (rr4) removal by cross-linked chitosan-epichlorohydrin using boxbehnken design,” *Science Lettes (ScL)*, vol. 14, no. 1, pp. 83–95, 2020.
- [97] A. Okudan, B. E. Ataoglu, O. Sengoz, and G. Arslan, “Cu (ii) sorption performance of novel chitosan/ter-(vinyl pivalate-maleic anhydride-n-tert-butylacrylamide) microcapsules,” *Journal of Polymers and the Environment*, vol. 27, no. 11, pp. 2454–2463, 2019.
- [98] A. H. Jawad, A. S. Abdulhameed, and M. S. Mastuli, “Mesoporous crosslinked chitosan-activated charcoal composite for the removal of thionine cationic dye: comprehensive adsorption and mechanism study,” *Journal of Polymers and the Environment*, vol. 28, no. 3, pp. 1095–1105, 2020.
- [99] I. Alakhras, F. Ouachtak, H. Alhajri, E. Rehman, R. Al-Mazaideh, G. Anastopoulos, and E. C. Lima, “Adsorptive removal of cationic rhodamine b dye from aqueous solutions using chitosan-derived schiff base,” *Separation Science and Technology*, pp. 1–13, 2021.
- [100] A. H. Jawad, A. S. Abdulhameed, L. D. Wilson, M. Hanafiah, W. Nawawi, Z. A. ALOthman, and M. R. Khan, “Fabrication of schiffs base chitosan-glutaraldehyde/activated charcoal composite for cationic dye removal: Optimization using response surface methodology,” *Journal of Polymers and the Environment*, pp. 1–14, 2021.
- [101] N. N. Abd Malek, A. H. Jawad, A. S. Abdulhameed, K. Ismail, and B. Hameed, “New magnetic schiff’s base-chitosan-glyoxal/fly ash/fe₃o₄ biocomposite for the removal of anionic azo dye: An optimized process,” *International journal of biological macromolecules*, vol. 146, pp. 530–539, 2020.
- [102] L. Y. Maroufi, M. Tabibiazar, M. Ghorbani, and A. Jahanban-Esfahlan, “Fabrication and characterization of novel antibacterial chitosan/dialdehyde guar gum hydrogels containing pomegranate peel extract for active food packaging application,” *International Journal of Biological Macromolecules*, vol. 187, pp. 179–188, 2021.
- [103] R. E. Malekshah, F. Shakeri, A. Khaleghian, and M. Salehi, “Developing a biopolymeric chitosan supported schiff-base and cu (ii), ni (ii) and zn (ii) complexes and biological evaluation as pro-drug,” *International journal of biological macromolecules*, vol. 152, pp. 846–861, 2020.
- [104] N. Sarjono, N. B. A. Prasetya, and D. N. Bima, “Synthesis of mn (ii) complexes-carboxymethyl chitosan schiff base salicylaldehyde and antibacterial activity.”

-
- [105] R. S. Vieira and M. M. Beppu, "Interaction of natural and crosslinked chitosan membranes with hg (ii) ions," *Colloids and Surfaces A: Physicochemical and Engineering Aspects*, vol. 279, no. 1-3, pp. 196–207, 2006.
- [106] M. H. Mostafa, M. A. Elsayy, M. S. Darwish, L. I. Hussein, and A. H. Abdaleem, "Microwave-assisted preparation of chitosan/zno nanocomposite and its application in dye removal," *Materials Chemistry and Physics*, vol. 248, p. 122914, 2020.
- [107] K. M. Rao, M. Suneetha, G. T. Park, A. G. Babu, and S. S. Han, "Hemostatic, biocompatible, and antibacterial non-animal fungal mushroom-based carboxymethyl chitosan-zno nanocomposite for wound-healing applications," *International journal of biological macromolecules*, vol. 155, pp. 71–80, 2020.
- [108] A. H. Jawad, I. A. Mohammed, and A. S. Abdulhameed, "Tuning of fly ash loading into chitosan-ethylene glycol diglycidyl ether composite for enhanced removal of reactive red 120 dye: optimization using the box-behnken design," *Journal of Polymers and the Environment*, vol. 28, no. 10, pp. 2720–2733, 2020.
- [109] S.-B. Ghaffari, M.-H. Sarrafzadeh, M. Salami, and M. R. Khorramizadeh, "A ph-sensitive delivery system based on n-succinyl chitosan-zno nanoparticles for improving antibacterial and anticancer activities of curcumin," *International journal of biological macromolecules*, vol. 151, pp. 428–440, 2020.
- [110] A. Soubhagya, A. Moorthi, and M. Prabakaran, "Preparation and characterization of chitosan/pectin/zno porous films for wound healing," *International journal of biological macromolecules*, vol. 157, pp. 135–145, 2020.
- [111] K. S. Sing, "Reporting physisorption data for gas/solid systems with special reference to the determination of surface area and porosity (recommendations 1984)," *Pure and applied chemistry*, vol. 57, no. 4, pp. 603–619, 1985.
- [112] A. H. Jawad, N. N. Abd Malek, A. S. Abdulhameed, and R. Razuan, "Synthesis of magnetic chitosan-fly ash/fe 3 o 4 composite for adsorption of reactive orange 16 dye: optimization by box-behnken design," *Journal of Polymers and the Environment*, vol. 28, no. 3, pp. 1068–1082, 2020.
- [113] A. Alipour, S. Zarinabadi, A. Azimi, and M. Mirzaei, "Adsorptive removal of pb (ii) ions from aqueous solutions by thiourea-functionalized magnetic zno/nanocellulose composite:

- optimization by response surface methodology (rsm),” *International journal of biological macromolecules*, vol. 151, pp. 124–135, 2020.
- [114] E. Sharifpour, M. Ghaedi, A. Asfaram, M. Farsadrooh, E. A. Dil, and H. Javadian, “Modeling and optimization of ultrasound-assisted high performance adsorption of basic fuchsin by starch-capped zinc selenide nanoparticles/ac as a novel composite using response surface methodology,” *International journal of biological macromolecules*, vol. 152, pp. 913–921, 2020.
- [115] S. M. Ghoreishian, G. S. R. Raju, E. Pavitra, C. H. Kwak, Y.-K. Han, and Y. S. Huh, “Ultrasound-assisted heterogeneous degradation of tetracycline over flower-like rgo/cdwo₄ hierarchical structures as robust solar-light-responsive photocatalysts: Optimization, kinetics, and mechanism,” *Applied Surface Science*, vol. 489, pp. 110–122, 2019.
- [116] M. N. Zafar, Q. Dar, F. Nawaz, M. N. Zafar, M. Iqbal, and M. F. Nazar, “Effective adsorptive removal of azo dyes over spherical zno nanoparticles,” *Journal of Materials Research and Technology*, vol. 8, no. 1, pp. 713–725, 2019.
- [117] N. D. Shooto, “Removal of toxic hexavalent chromium (cr (vi)) and divalent lead (pb (ii)) ions from aqueous solution by modified rhizomes of acorus calamus,” *Surfaces and Interfaces*, vol. 20, p. 100624, 2020.
- [118] S. Lagergren, “Zur theorie der sogenannten adsorption geloster stoffe,” 1898.
- [119] Y.-S. Ho and G. McKay, “Sorption of dye from aqueous solution by peat,” *Chemical engineering journal*, vol. 70, no. 2, pp. 115–124, 1998.
- [120] A. G. El-Shamy, “An efficient removal of methylene blue dye by adsorption onto carbon dot@ zinc peroxide embedded poly vinyl alcohol (pva/czno₂) nano-composite: a novel reusable adsorbent,” *Polymer*, vol. 202, p. 122565, 2020.
- [121] C. Muthukumar, V. M. Sivakumar, and M. Thirumarimurugan, “Adsorption isotherms and kinetic studies of crystal violet dye removal from aqueous solution using surfactant modified magnetic nanoadsorbent,” *Journal of the Taiwan Institute of Chemical Engineers*, vol. 63, pp. 354–362, 2016.
- [122] I. Langmuir, “The adsorption of gases on plane surfaces of glass, mica and platinum.” *Journal of the American Chemical society*, vol. 40, no. 9, pp. 1361–1403, 1918.

-
- [123] H. Freundlich *et al.*, “Over the adsorption in solution,” *J. Phys. chem*, vol. 57, no. 385471, pp. 1100–1107, 1906.
- [124] M. Temkin, “Kinetics of ammonia synthesis on promoted iron catalysts,” *Acta physicochim. URSS*, vol. 12, pp. 327–356, 1940.
- [125] Y. Lei, Q. Huang, D. Gan, H. Huang, J. Chen, F. Deng, M. Liu, X. Li, X. Zhang, and Y. Wei, “A novel one-step method for preparation of sulfonate functionalized nanodiamonds and their utilization for ultrafast removal of organic dyes with high efficiency: Kinetic and isotherm studies,” *Journal of Environmental Chemical Engineering*, vol. 8, no. 3, p. 103780, 2020.
- [126] S. M. El-Kousy, H. G. El-Shorbagy, and M. Abd El-Ghaffar, “Chitosan/montmorillonite composites for fast removal of methylene blue from aqueous solutions,” *Materials Chemistry and Physics*, vol. 254, p. 123236, 2020.
- [127] N. K. Nga, N. T. T. Chau, and P. H. Viet, “Preparation and characterization of a chitosan/mgo composite for the effective removal of reactive blue 19 dye from aqueous solution,” *Journal of Science: Advanced Materials and Devices*, vol. 5, no. 1, pp. 65–72, 2020.
- [128] V. Janaki, B.-T. Oh, K. Shanthi, K.-J. Lee, A. Ramasamy, and S. Kamala-Kannan, “Polyaniline/chitosan composite: an eco-friendly polymer for enhanced removal of dyes from aqueous solution,” *Synthetic Metals*, vol. 162, no. 11-12, pp. 974–980, 2012.
- [129] X. Li, C. Sun, W. Cao, C. Hu, and Y. Zhao, “Comparative adsorption of remazol brilliant blue r and copper in aqueous solutions by carbon nanotubes with different levels of carboxyl group and specific surface area,” *Materials Research Express*, vol. 6, no. 10, p. 1050e2, 2019.
- [130] D.-N. Phan, R. A. Rebia, Y. Saito, D. Kharaghani, M. Khatri, T. Tanaka, H. Lee, and I.-S. Kim, “Zinc oxide nanoparticles attached to polyacrylonitrile nanofibers with hinokitiol as gluing agent for synergistic antibacterial activities and effective dye removal,” *Journal of Industrial and Engineering Chemistry*, vol. 85, pp. 258–268, 2020.
- [131] A. Özcan, Ç. Ömeroğlu, Y. Erdoğan, and A. S. Özcan, “Modification of bentonite with a cationic surfactant: an adsorption study of textile dye reactive blue 19,” *Journal of hazardous materials*, vol. 140, no. 1-2, pp. 173–179, 2007.

-
- [132] A. Dalvand, R. Nabizadeh, M. R. Ganjali, M. Khoobi, S. Nazmara, and A. H. Mahvi, "Modeling of reactive blue 19 azo dye removal from colored textile wastewater using l-arginine-functionalized Fe_3O_4 nanoparticles: Optimization, reusability, kinetic and equilibrium studies," *Journal of Magnetism and Magnetic Materials*, vol. 404, pp. 179–189, 2016.
- [133] V. Nair, A. Panigrahy, and R. Vinu, "Development of novel chitosan–lignin composites for adsorption of dyes and metal ions from wastewater," *Chemical Engineering Journal*, vol. 254, pp. 491–502, 2014.
- [134] M. Abbasi, "Synthesis and characterization of magnetic nanocomposite of chitosan/ SiO_2 /carbon nanotubes and its application for dyes removal," *Journal of Cleaner Production*, vol. 145, pp. 105–113, 2017.
- [135] O. A. Saputra, A. H. Rachma, and D. S. Handayani, "Adsorption of remazol brilliant blue r using amino-functionalized organosilane in aqueous solution," *Indonesian Journal of Chemistry*, vol. 17, no. 3, pp. 343–350, 2017.
- [136] C. J. Mate and S. Mishra, "Synthesis of borax cross-linked jhingan gum hydrogel for remediation of remazol brilliant blue r (rbbr) dye from water: adsorption isotherm, kinetic, thermodynamic and biodegradation studies," *International journal of biological macromolecules*, vol. 151, pp. 677–690, 2020.
- [137] A. S. Abdulhameed, A.-T. Mohammad, and A. H. Jawad, "Application of response surface methodology for enhanced synthesis of chitosan tripolyphosphate/ TiO_2 nanocomposite and adsorption of reactive orange 16 dye," *Journal of Cleaner Production*, vol. 232, pp. 43–56, 2019.
- [138] Y. Jiang, W. Cai, W. Tu, and M. Zhu, "Facile cross-link method to synthesize magnetic $\text{Fe}_3\text{O}_4@ \text{SiO}_2$ –chitosan with high adsorption capacity toward hexavalent chromium," *Journal of Chemical & Engineering Data*, vol. 64, no. 1, pp. 226–233, 2018.
- [139] S. C. Motshekga, S. S. Ray, M. S. Onyango, and M. N. Momba, "Preparation and antibacterial activity of chitosan-based nanocomposites containing bentonite-supported silver and zinc oxide nanoparticles for water disinfection," *Applied Clay Science*, vol. 114, pp. 330–339, 2015.

- [140] H. Wang, X. Gong, Y. Miao, X. Guo, C. Liu, Y.-Y. Fan, J. Zhang, B. Niu, and W. Li, "Preparation and characterization of multilayer films composed of chitosan, sodium alginate and carboxymethyl chitosan-zno nanoparticles," *Food chemistry*, vol. 283, pp. 397–403, 2019.
- [141] L. P. Lingamdinne, J. R. Koduru, Y.-Y. Chang, and R. R. Karri, "Process optimization and adsorption modeling of pb (ii) on nickel ferrite-reduced graphene oxide nanocomposite," *Journal of Molecular Liquids*, vol. 250, pp. 202–211, 2018.
- [142] A. H. Jawad, A. S. Abdulhameed, A. Reghioua, and Z. M. Yaseen, "Zwitterion composite chitosan-epichlorohydrin/zeolite for adsorption of methylene blue and reactive red 120 dyes," *International Journal of Biological Macromolecules*, vol. 163, pp. 756–765, 2020.
- [143] X. Zheng, H. Zheng, Z. Xiong, R. Zhao, Y. Liu, C. Zhao, and C. Zheng, "Novel anionic polyacrylamide-modify-chitosan magnetic composite nanoparticles with excellent adsorption capacity for cationic dyes and ph-independent adsorption capability for metal ions," *Chemical Engineering Journal*, vol. 392, p. 123706, 2020.
- [144] R. Abd Rashid, A. H. Jawad, M. Azlan, M. Ishak, and N. Kasim, "Fecl₃-activated carbon developed from coconut leaves: characterization and application for methylene blue removal," *Sains Malaysiana*, vol. 47, no. 3, pp. 603–610, 2018.
- [145] A. H. Jawad, N. S. A. Mubarak, and A. S. Abdulhameed, "Hybrid crosslinked chitosan-epichlorohydrin/tio₂ nanocomposite for reactive red 120 dye adsorption: kinetic, isotherm, thermodynamic, and mechanism study," *Journal of Polymers and the Environment*, vol. 28, no. 2, pp. 624–637, 2020.
- [146] Y. Chen, W. Cai, C. Dang, J. Fan, J. Zhou, and Z. Liu, "A facile sol-gel synthesis of chitosan-boehmite film with excellent acid resistance and adsorption performance for pb (ii)," *Chemical Engineering Research and Design*, vol. 161, pp. 332–339, 2020.
- [147] V. Rizzi, J. Gubitosa, P. Fini, R. Romita, A. Agostiano, S. Nuzzo, and P. Cosma, "Commercial bentonite clay as low-cost and recyclable natural adsorbent for the carbendazim removal/recover from water: Overview on the adsorption process and preliminary photodegradation considerations," *Colloids and Surfaces A: Physicochemical and Engineering Aspects*, vol. 602, p. 125060, 2020.
- [148] A. H. Jawad and A. S. Abdulhameed, "Facile synthesis of crosslinked chitosan-tripolyphosphate/kaolin clay composite for decolourization and cod reduction of remazol

- brilliant blue r dye: optimization by using response surface methodology,” *Colloids and Surfaces A: Physicochemical and Engineering Aspects*, vol. 605, p. 125329, 2020.
- [149] D. T. Ogunleye, S. O. Akpotu, and B. Moodley, “Adsorption of sulfamethoxazole and reactive blue 19 using graphene oxide modified with imidazolium based ionic liquid,” *Environmental Technology & Innovation*, vol. 17, p. 100616, 2020.
- [150] K. Vijayaraghavan, S. W. Won, and Y.-S. Yun, “Treatment of complex remazol dye effluent using sawdust-and coal-based activated carbons,” *Journal of Hazardous Materials*, vol. 167, no. 1-3, pp. 790–796, 2009.
- [151] K. Chinoune, K. Bentaleb, Z. Bouberka, A. Nadim, and U. Maschke, “Adsorption of reactive dyes from aqueous solution by dirty bentonite,” *Applied Clay Science*, vol. 123, pp. 64–75, 2016.
- [152] F. Zhang, X. Chen, F. Wu, and Y. Ji, “High adsorption capability and selectivity of zno nanoparticles for dye removal,” *Colloids and Surfaces A: Physicochemical and Engineering Aspects*, vol. 509, pp. 474–483, 2016.
- [153] A. H. Jawad, A. S. Abdulhameed, N. N. Abd Malek, and Z. A. ALothman, “Statistical optimization and modeling for color removal and cod reduction of reactive blue 19 dye by mesoporous chitosan-epichlorohydrin/kaolin clay composite,” *International journal of biological macromolecules*, vol. 164, pp. 4218–4230, 2020.
- [154] S. Pandey and S. Tiwari, “Facile approach to synthesize chitosan based composite characterization and cadmium (ii) ion adsorption studies,” *Carbohydrate Polymers*, vol. 134, pp. 646–656, 2015.
- [155] H. Karaer and İ. Kaya, “Synthesis, characterization and using at the copper adsorption of chitosan/polyvinyl alcohol magnetic composite,” *Journal of Molecular Liquids*, vol. 230, pp. 152–162, 2017.
- [156] E. Zabihi, A. Babaei, D. Shahrampour, Z. Arab-Bafrani, K. S. Mirshahidi, and H. J. Majidi, “Facile and rapid in-situ synthesis of chitosan-zno nano-hybrids applicable in medical purposes; a novel combination of biomineralization, ultrasound, and bio-safe morphology-conducting agent,” *International journal of biological macromolecules*, vol. 131, pp. 107–116, 2019.

-
- [157] M. Slaný, L. Jankovič, and J. Madejová, “Structural characterization of organo-montmorillonites prepared from a series of primary alkylamines salts: Mid-ir and near-ir study,” *Applied Clay Science*, vol. 176, pp. 11–20, 2019.
- [158] W. Du, M. Slaný, X. Wang, G. Chen, and J. Zhang, “The inhibition property and mechanism of a novel low molecular weight zwitterionic copolymer for improving wellbore stability,” *Polymers*, vol. 12, no. 3, p. 708, 2020.
- [159] D.-M. Guo, Q.-D. An, Z.-Y. Xiao, S.-R. Zhai, and D.-J. Yang, “Efficient removal of pb (ii), cr (vi) and organic dyes by polydopamine modified chitosan aerogels,” *Carbohydrate polymers*, vol. 202, pp. 306–314, 2018.
- [160] L. Qi, Z. Xu, X. Jiang, C. Hu, and X. Zou, “Preparation and antibacterial activity of chitosan nanoparticles,” *Carbohydrate research*, vol. 339, no. 16, pp. 2693–2700, 2004.
- [161] S. Wang, Y. Lu, X.-k. Ouyang, X. X. Liang, D. Yu, L.-Y. Yang, and F. Huang, “Fabrication of chitosan-based mcs/zno@ alg gel microspheres for efficient adsorption of as (v),” *International journal of biological macromolecules*, vol. 139, pp. 886–895, 2019.
- [162] J. Qu, X. Meng, H. You, X. Ye, and Z. Du, “Utilization of rice husks functionalized with xanthates as cost-effective biosorbents for optimal cd (ii) removal from aqueous solution via response surface methodology,” *Bioresource technology*, vol. 241, pp. 1036–1042, 2017.
- [163] S. Saha, B.-H. Jeon, M. B. Kurade, S. B. Jadhav, P. K. Chatterjee, S. W. Chang, S. P. Govindwar, and S. J. Kim, “Optimization of dilute acetic acid pretreatment of mixed fruit waste for increased methane production,” *Journal of Cleaner Production*, vol. 190, pp. 411–421, 2018.
- [164] E. Natarajan and G. P. Ponnaiah, “Optimization of process parameters for the decolorization of reactive blue 235 dye by barium alginate immobilized iron nanoparticles synthesized from aluminum industry waste,” *Environmental Nanotechnology, Monitoring & Management*, vol. 7, pp. 73–88, 2017.
- [165] B. Zhang, J. Zhang, Q. Yang, C. Feng, Y. Zhu, Z. Ye, and J. Ni, “Investigation and optimization of the novel uasb–mfc integrated system for sulfate removal and bioelectricity generation using the response surface methodology (rsm),” *Bioresource technology*, vol. 124, pp. 1–7, 2012.

- [166] S. Surip, A. S. Abdulhameed, Z. N. Garba, S. S. A. Syed-Hassan, K. Ismail, and A. H. Jawad, "H₂so₄-treated malaysian low rank coal for methylene blue dye decolourization and cod reduction: optimization of adsorption and mechanism study," *Surfaces and Interfaces*, vol. 21, p. 100641, 2020.
- [167] H. Bensalah, S. A. Younssi, M. Ouammou, A. Gurlo, and M. F. Bekheet, "Azo dye adsorption on an industrial waste-transformed hydroxyapatite adsorbent: kinetics, isotherms, mechanism and regeneration studies," *Journal of Environmental Chemical Engineering*, vol. 8, no. 3, p. 103807, 2020.
- [168] Z. A. AlOthman, M. A. Habila, R. Ali, A. A. Ghafar, and M. S. E.-d. Hassouna, "Valorization of two waste streams into activated carbon and studying its adsorption kinetics, equilibrium isotherms and thermodynamics for methylene blue removal," *Arabian Journal of Chemistry*, vol. 7, no. 6, pp. 1148–1158, 2014.
- [169] H. L. Parker, A. J. Hunt, V. L. Budarin, P. S. Shuttleworth, K. L. Miller, and J. H. Clark, "The importance of being porous: polysaccharide-derived mesoporous materials for use in dye adsorption," *RSC advances*, vol. 2, no. 24, pp. 8992–8997, 2012.
- [170] R. S. Blackburn, "Natural polysaccharides and their interactions with dye molecules: applications in effluent treatment," *Environmental science & technology*, vol. 38, no. 18, pp. 4905–4909, 2004.
- [171] S. K. Singh and A. Das, "The n π^* interaction: a rapidly emerging non-covalent interaction," *Physical Chemistry Chemical Physics*, vol. 17, no. 15, pp. 9596–9612, 2015.